UNIVERSITÀ DEGLI STUDI DI PAVIA

FACOLTÀ DI INGEGNERIA

DOTTORATO DI RICERCA IN MICROELETTRONICA
XXII CICLO

INTEGRATED MAGNETIC SENSOR INTERFACE CIRCUITS AND PHOTOVOLTAIC ENERGY HARVESTER SYSTEMS

Tutor:
Chiar.mo Prof. Piero Malcovati

Coordinatore del Corso di Dottorato:
Chiar.mo Prof. Rinaldo Castello

Tesi di Dottorato
di Ferri Massimo

Alle ambizioni

Contents

List of Figures

Introduction

The first part of the thesis focuses on the design of integrated magnetic sensor interface circuits. Magnetic phenomena can represent an optimal information carrier in many applications. The first application considered is an electronic compass based on a Fluxgate magnetic sensor. In particular we designed a reliable measurement setup that allowed us to improve the previously obtained results of 50%. Indeed with a manual approach the maximum detectable angular accuracy was 4 degrees, while with an automated approach it has been reduced to 1.5 degrees.

A new fluxgate magnetic sensor interface circuit has then been designed, to realize a low-power current measurement system for portable applications. The total power consumption has been drastically reduced with an improvement of the linearity of the entire system. The circuit can provide a widely programmable excitation current to the Fluxgate sensor and read-out the sensor signal with variable gain. Moreover, the circuit provides digital output. All the design and implementation details are presented together with experimental results.

The second part of this thesis is focused on photovoltaic energy harvesting solutions. In particular we realized two integrated microsystems. The first one is photovoltaic power supply system for discrete-time applications. In particular we realized a totally autonomous circuit that charges an external capacitor and monitors the accumulated energy. When the energy is enough to supply an external or on-chip system, the load is connected. When the capacitor is discharged the load

is disconnected. This approach allows us to supply any kind of electronic device that consumes more power than the power that the integrated micro solar cell can provide. This solution has been realized in 0.35-µm standard CMOS technology.
The second energy harvester solution is a photovoltaic voltage regulator with an autonomous temperature sensor. In particular the system provides a regulated 3.3-V voltage supply and provides information about the temperature of the chip. The system has been designed also for low level of illumination.
Both solutions are presented with experimental results.

Chapter 1

Magnetic Sensor Interface Circuits

In this chapter a short background information about magnetic sensors is provided, with a detailed description of the considered devices: the Fluxgate magnetic sensors. Moreover we will describe the measurement setup that has been developed to characterize an integrated interface circuit previously realized. On the basis of the obtained experimental results, a new version of the is presented with the relative experimental results.

1.1 Introduction

Magnetic materials and their behavior are known since hundreds of years [1], and their applications range have been drastically improved. At the beginning they were available only as mechanical devices for navigation and orientation in open spaces. The 1-1 compass is one of the oldest example. Recently to detect a magnetic field it is possible to use both mechanical and electronic sensors. The main advantage of the electronic sensors, which have been recently developed, is that they can be integrated together with electronic interface circuits in the data processing flow. This improves the embedding development trend, but introduces more complexity in the measurement setup design. There are several types of magnetic sensors, but, basically, all of them, when detecting a magnetic field, show a small variation of a physical property or of a parameter of the device. The entity of this variation, which is related to the sensitivity of the sensor to the applied magnetic field, makes the sensor itself suitable for a specific application [2, 3, 4]. It is thus possible to classify the magnetic sensors by using their magnetic field sensing range. As shown in Fig. 1.1, three categories of sensors can be identified:

- low field
- medium field
- high field

Magnetic fields lower than 1 μT are very small and well below the Earth magnetic field. Sensors with field sensing range from 10 μT to 300 μT are considered Earth magnetic field sensors, while sensors with field sensing range above 1 mT are classified as bias magnet field sensors. For measuring the Earth magnetic field with devices that are suitable for portable applications, the magneto-resistance and magneto-inductance (to be used as discrete sensors) are available, as well as the Fluxgate magnetic sensors. Fluxgate sensors and magneto-resistances require the use of a ferromagnetic material. They, as well as magneto-transistors and Hall sensors, can be integrated by using CMOS technologies [5, 6, 4]. The use of a ferromagnetic material as concentrator can help in increasing their sensitivity. Fluxgate sensors, Hall sensors with magnetic concentrator and magneto-transistors allow the implementation of 2D measurements on-chip. By contrast, conventional Hall devices can be used only for 1D measurements. Each sensor has specific features that make it suitable for a given range of applications. In addition to the sensitivity, it is necessary to consider the range of temperature, the

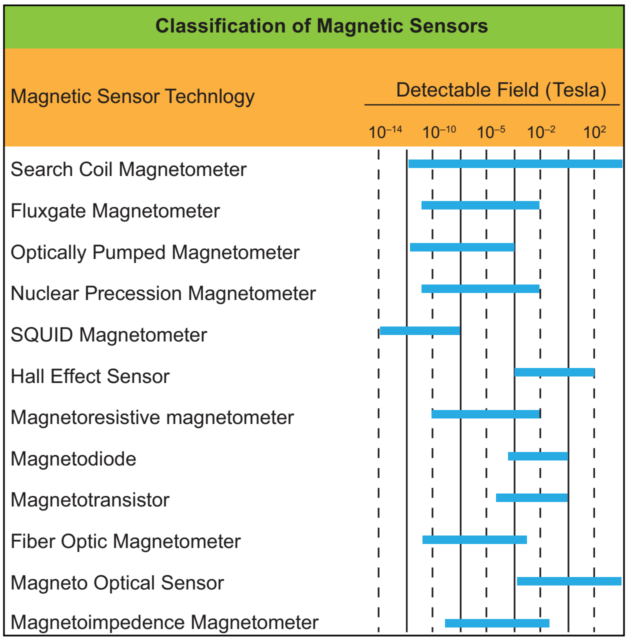

Figure 1.1: Classification of magnetic sensors

sensor volume, and its on-chip manufacturability. Nowadays, there are several different applications where magnetic sensors can be used. Among them electronic compasses [7], sensors for traffic control, magnet activated switches for cellular phones, notebooks or handheld devices can be mentioned. Other applications are in the automotive field or home appliances: devices based on magnetic sensors are used, for example, to control the car engine or in domestic environment.

1.2 Magnetic Sensors

As shown in Fig. 1.1 there are several magnetic sensors that use different technologies to detect magnetic field. The principles of operation of the most used types of magnetic sensors are listed below.

1.2.1 SQUID

The magnetic sensor with the highest sensitivity is the Superconducting Quantum Interface Device (SQUID). Developed around 1962, it is able to detect magnetic fields from few femto-Tesla to tens of Tesla. It is used in medical applications since it can detect the human brain neuro-magnetic field (about few femtoTesla). The main drawback of such a sensor is the low temperature of operation (about 4 K) needed to cool down the junction required to measure the current induced by the magnetic field.

1.2.2 Search-coil

Search coils are based on the induction Faraday law, which establishes that the induced voltage in a coil is proportional to the variation of the magnetic field concatenated to the same coil. This voltage creates a current that is proportional to the speed of the variation of the field itself. The sensitivity of the search-coil depends on the properties of the magnetic material used, the area of the coils and the number of coils used. The direct application of the Faraday law makes this sensor not suitable for static or low-frequency fields.

1.2.3 Magneto-inductive sensor

fempto-Tesla The magneto-inductive sensor is a new type of magnetic sensor developed about twenty years ago. Nowadays it is one of the cheapest and most used sensor thanks to its reliability. The magneto-inductive sensor is basically a solenoid with magnetic material inside. If a current flows inside the solenoid, it generates a magnetic field and an induced voltage. By linking this voltage to the initial current it is possible to obtain the value of the inductance of the sensor. An external magnetic field H_{ext} changes the value of the magneto-inductance, since it changes the value of the induced voltage by the sensed magnetic field. By employing a circuit able to detect the value of the inductance, it is possible to derive the value of an external magnetic field.

1.2.4 Magneto-resistance

Magneto-resistive sensors are based on the anisotropic magneto-resistance effect (AMR) and have been developed in the last 30 years. Magneto-resistive sensors exploit the fact that external fields H influences the electrical resistance ρ of certain ferromagnetic alloys. This solid-state magneto-resistive effect can be easily realized by using a thin film technology. The specific resistance ρ of anisotropic ferromagnetic metals depends on the angle θ between the internal magnetization M and the current I, according to

$$\rho(\theta) = \rho_p + (\rho_p - \rho_{||})cos^2(\theta) \tag{1.1}$$

where ρ_p and $\rho_{||}$ are the resistivities perpendicular and parallel to M. The quotient

$$\frac{(\rho_p - \rho_{||})}{\rho} = \frac{\Delta\rho}{\rho} \tag{1.2}$$

is called the magneto-resistive effect and may amount to several percent. Sensors are always made of ferromagnetic thin films as this has two major advantages over bulk material: the resistance is high and the anisotropy can be made uniaxial. The ferromagnetic layer behaves like a single domain and has one distinguished direction of magnetization in its plane called the easy axis (e.a.), which is the direction of magnetization without external field influence.

1.2.5 Hall sensor

The Hall effect was discovered by Dr. Edwin Hall in 1879. Dr. Hall found that when a magnet was placed so that its field was perpendicular to one face of a thin rectangle of gold through which current was flowing, a difference in potential appeared at the opposite edges. He found that this voltage was proportional to the current flowing through the conductor, and the flux density or magnetic induction perpendicular to the conductor. When a current-carrying conductor is placed into a magnetic field, a voltage will be generated perpendicular to both the current and the field. This principle is known as the Hall effect. Figure 5.2-5 illustrates the basic principle of the Hall effect. It shows a thin sheet of semiconducting material (Hall element) through which a current flows. The output connections are perpendicular to the direction of the current. When no magnetic field is present, the current distribution is uniform and no potential difference is seen across the output. When a perpendicular magnetic field is present a Lorentz force is exerted on the current. This force disturbs the current distribution, resulting in a potential difference (voltage) across the output. This voltage is the Hall voltage (V_H). For

[ht]

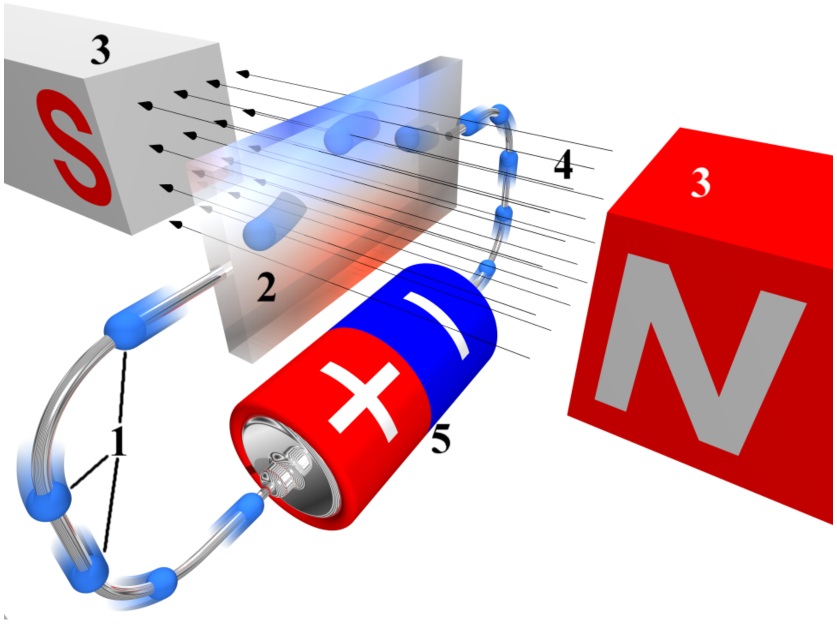

Figure 1.2: Hall effect

the Lorentz's law, a charged particle q moving inside the conductor in magnetic field B with a speed equal to v_d, is subject to a force equal to:

$$F = q \cdot v_d \times B \tag{1.3}$$

where × is the vectorial product operator between v_d and B.

In stationary condition this force is balanced by the induced electrical field generated from a charge redistribution, named Hall field H_E. The integral of this field along the conductor gives the Hall voltage V_H. This voltage is equal to $V_H = E_H W$ in the case that B is uniform along the conductor, where W is the width. An electron placed inside the conductor is subject to a force equal to $F = q \cdot E_H$. Using equation 1.3, and considering $v_d = -J_x/q$, where J_x is he current density, it results

$$q \cdot E_H = q \cdot v_d \cdot B \tag{1.4}$$

that means

$$E_H = R_H \cdot J_x \cdot B \tag{1.5}$$

where R_H is defined as the Hall coefficient. By considering parameter r that takes into account the variation of speed of the carrier (+ for electrons or − for holes)

$$R_H = \pm \frac{r}{q} \tag{1.6}$$

Hall voltage can be expressed as

$$V_H = R_H \frac{I \cdot B}{10^8 t} \tag{1.7}$$

By using equation 1.7 it is possible to determine the type of carriers and the concentration. From this values and knowing the current, it is possible to obtain the conductivity and the Hall mobility ($\mu = \sigma |R_H|$).

1.2.6 Fluxgate sensor

Fluxgate sensors are among the most used magnetometers thanks to their possibility to be integrated together with microelectronic circuits. Fluxgate magnetometers were first introduced in the 1930's. Some development was for airborne magnetic surveys and for submarine detection, like Hall devices. They were further developed for geomagnetic studies, for mineral prospecting and for magnetic measurements in outer space. They have also been adapted and developed for various detections and surveillance devices, both for civil and military use. Despite the advent of newer technologies for magnetic field measurements, Fluxgate magnetometers continue to be used successfully in all of these areas, thanks to their reliability, relative simplicity, and low cost. In the late 1950's, the Fluxgate was adapted to space magnetometer applications. Even as early as 1948, a three-axis Fluxgate was used in an Aerobee sounding rocket to a peak altitude of 112 km. The first satellite to carry a magnetometer of any type was Sputnik 3 which was launched in 1958 and carried a servo-oriented Fluxgate. Luniks 1 and 2 (Russian lunar probes), both launched in 1958, carried triaxial Fluxgates. The USSR Venus probe launched in 1961 carried two single-axis Fluxgates. The first American satellite to carry a Fluxgate was Earth orbiting Explorer 6 launched in 1959. Some satellites or space probes carrying Fluxgate have included USSR Mars probe, Nasa Explorer 12, 14 and 18, Mariner 2 (Venus) the USSR Earth-orbit Electron 2 and Apollo 12, 14, 15 and 16. Nowadays, developments for this sensor are expected in the solution based on CMOS technology for the coils and CMOS compatible post-processing technology (i.e. sputtering) for the core deposition. In this way, it is possible to realize micro-Fluxgates featuring very low power consumption (in the order of few mW) and minimum silicon area. They show some common point with magneto-inductances due essentially to their similar structure. The basic structure of a Fluxgate sensor is shown in Fig. 1.3. The sensor consists of a couple of coils: the first one provides the excitation [8] to saturate the ferromagnetic material of the core (excitation coils). The second one is used to read out the signal (sensing coils). These coils are wrapped around a ferromagnetic core with an high magnetic permeability, in order to collect all the

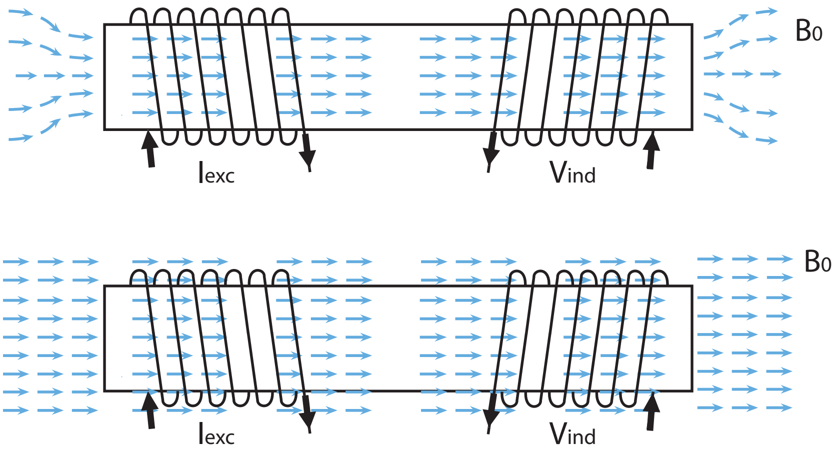

Figure 1.3: Structure of a Fluxgate magnetic sensor

magnetic field to measure. When a current I_{exc} flows into the excitation coils a magnetic field H(t) is generated (typically a triangular or a sinusoidal or, more generally, an excitation current with odd symmetry is used). This magnetic field generates a magnetic induction field B(t), according to the magnetic permeability μ_{eff}(t) of the magnetic material B-H function. Varying the current I_{exc}, the magnetic field B(t) changes causing the material to switch from a non-saturation condition (Fig. 1.4.a) in which all the magnetic field is collected inside the ferromagnetic material, to the saturation condition (Fig. 1.4.b), where the permeability drops and the DC flux associated with the DC magnetic field B_0 to be measured decreases and the sensor acts as in vacuum. The name of the device derives from this *gating* of the flux that occurs when the core is saturated. When the field to be measured is present, the second harmonic and also higher order even harmonics of the excitation current appear in the voltage V_{out}, induced in the sensing coil. This behavior is strictly related to the transfer function of the system that is the hysteresis loop of the magnetic field. Without an external magnetic field, when in the excitation coil flows a current at frequency f, the induced voltage is due to the sum of different harmonics at frequency f, 3f, 5f, 7f, and so on, because of

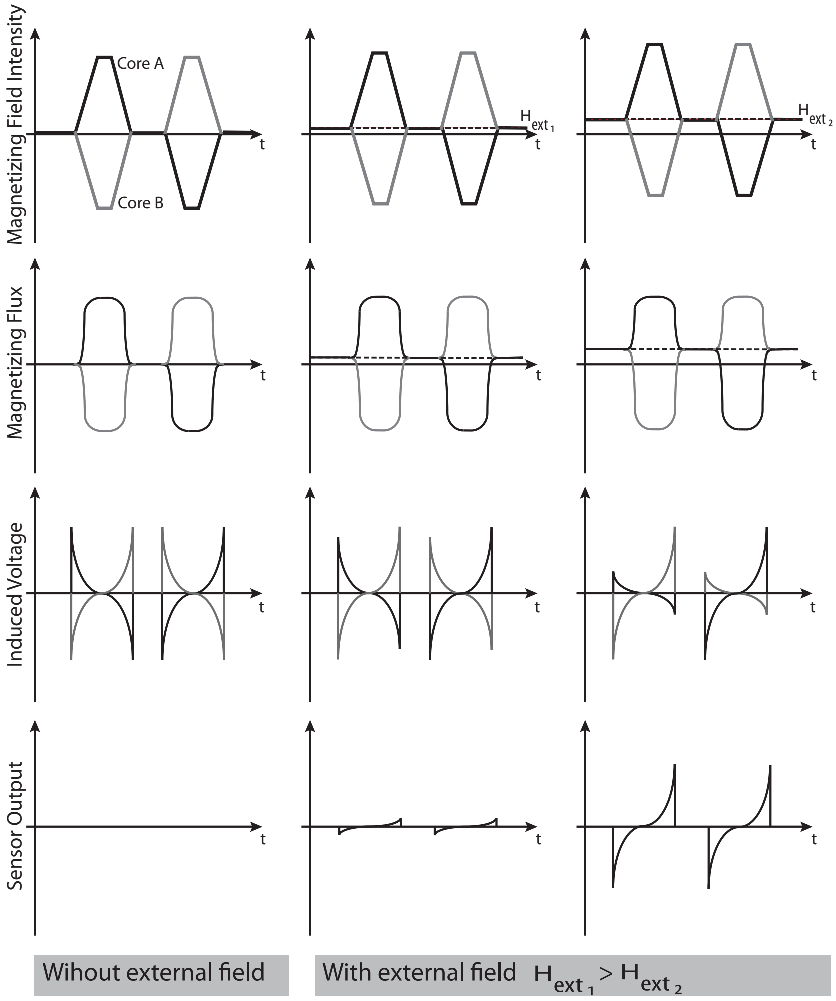

Figure 1.4: Effect of the magnetic field on the Fluxgate sensor output

the transfer function with odd symmetry. When an external magnetic field is applied, the different operating point degrades the symmetry in the transfer function and therefore, together with the odd harmonics, the even harmonics will appear. The amplitude of these even harmonics, that represent the sensor output, will be proportional to the intensity of the external magnetic field.

Let us evaluate the effect of a magnetic field over the sensor itself. First of all we have to distinguish between two different cases: with or without an external magnetic field H$_{ext}$. If we assume the ferromagnetic material B-H characteristic to be linear outside the saturation region with a constant value of μ_{eff} , we obtain

$$B = \mu_{eff}\mu_0 H \tag{1.8}$$

where μ_0 is the magnetic permeability of vacuum. If H$_{ext}$ = 0 (1st column in Fig. 1.4), and a triangular excitation current with frequency f is used, a magnetic field is generated, given by

$$H(t) = 4 \cdot f \cdot H_m \cdot t \quad for\ \ t \in \left[-\frac{1}{4f}\frac{H_s}{H_m} + \frac{n}{f}, \frac{1}{4f}\frac{H_s}{H_m} + \frac{n}{f} \right] \tag{1.9}$$

$$H(t) = -4 \cdot f \cdot H_m \cdot t \quad for\ \ t \in \left[\frac{1}{2f} - \frac{1}{4f}\frac{H_s}{H_m} + \frac{n}{f}, \frac{1}{2f} + \frac{1}{4f}\frac{H_s}{H_m} + \frac{n}{f} \right] \tag{1.10}$$

where n is a integer. For the Faraday-Neumann law, the output voltage of the sensor V$_{out}$ is proportional to the time derivative of the magnetic flux through the N sensing coils with area S.

$$V_{out} = -N \cdot \frac{d\Phi}{dt} = -N_{sens} \cdot A \cdot \frac{dB}{dt} \tag{1.11}$$

The time derivative of the induced magnetic field is equal to

$$\frac{dB}{dt} = 4 \cdot \mu \cdot f \cdot H_m \quad for\ \ t \in \left[-\frac{1}{4f}\frac{B_s}{B_m} + \frac{n}{f}, \frac{1}{4f}\frac{B_s}{B_m} + \frac{n}{f} \right] \tag{1.12}$$

$$\frac{dB}{dt} = -4 \cdot f \cdot H_m \cdot t \quad for\ \ t \in \left[-\frac{1}{4f}\frac{B_s}{B_m} + \frac{n+1}{2f}, \frac{1}{2f} + \frac{1}{4f}\frac{B_s}{B_m} + \frac{2n+1}{f} \right] \tag{1.13}$$

Outside this time limits, the magnetic material is in the saturation condition and thus $\frac{dB}{dt} = 0$. In this way V$_{out}$ consists of equally spaced positive and negative pulses, with amplitude equal to $4 \cdot N \cdot S \cdot \mu \cdot f \cdot H_m$. If a positive external magnetic field H$_{ext}$ is added, it changes the position and the length of the pulse, since it changes the period of time in which the ferromagnetic material is in saturation (2nd and 3rd column in Fig. 1.4). The negative pulse of V$_{out}$ is shifted of the quantity $\frac{H_{ext}}{4 \cdot f \cdot H_m}$, while the positive pulse is postponed of the same amount of time. For a negative magnetic field the delays are the same but opposite in sign. With a Fourier analysis the spectrum of the output induced voltage V$_{out}$ consists of odd harmonics if no external magnetic field is present, while second order and higher order even harmonics appear in presence of external magnetic field.

For a sinusoidal excitation $I = I_0 \cdot sin(2\pi f t)$ we obtain

$$V_{ind} = -\frac{d\Phi}{dt} = -N_{sens} \cdot S \cdot \frac{d}{dt}\left[\frac{\mu \cdot N_{exc} \cdot I_0 \cdot (sin(2\pi \cdot f_{exc} \cdot t)}{l}\right] \tag{1.14}$$

where $\mu = \mu_{eff} \cdot \mu_0$ is the magnetic permeability, f$_{exc}$ is the excitation frequency, N$_{sens}$ the number of sensing coils, N$_{exc}$ the number of excitation coils, l the length of the excitation coils. The sensor sensitivity can be improved by maximizing the induced voltage, and this can be done using the following solutions:

- by increasing the excitation frequency (f$_{exc}$); however, an upper bound to f$_{exc}$ is given by the cut-off frequency of the ferromagnetic material relative permeability;
- by increasing the number of turns of the sensing coil (N$_{sens}$);
- by increasing the cross section of the ferromagnetic material (S), considering that a larger cross-section requires a larger current to saturate the ferromagnetic material and, hence, an increased power consumption.

The amplitude of the second harmonic is equal to:

$$V_{out2} = 8 \cdot N_{sens} \cdot S \cdot \mu \cdot f \cdot H_{ext} \cdot sin\left(\frac{\pi H_s}{H_m}\right) \cdot sin(4\pi f t) \tag{1.15}$$

It is possible to notice that the amplitude is a linear function of the external magnetic field. The read out circuitry has to be able to detect the second order and the even high order harmonics that carry information about the external magnetic field, rejecting the other harmonics of the spectrum.

The main drawback of Fluxgate magnetic sensors realized with the structure shown in Fig. 1.3 is the complex construction of the core and of the coils when they have to be realized within planar technologies (CMOS-IC), in which it would be desirable to fabricate the ferromagnetic core with a post-processing step on-top of the planar process. In this case the structure of Fig. 1.3 can be difficult to implement. For this reason, new topologies of planar integrated micro-Fluxgate have been recently presented in the open literature. For instance, a structure for a differential double axis planar Fluxgate magnetic sensor is shown in Fig. 1.5. The ferromagnetic cores are placed over the diagonals of the excitation coil. Supplying the excitation coil with a suitable current, each half of the single axis core periodically saturates in opposite directions. When no external magnetic field is applied, the two sensing coils of the single axis, connected in anti-series (the current flows in opposite direction generating two opposite magnetic field), show a differential output voltage that ideally is zero. By contrast, when an external magnetic field component is present and parallel to the core, the magnetization in one half of the core is in the same direction as the external magnetic field, while the magnetization of the other half of the core is in the opposite direction (Fig. 1.6). Therefore,

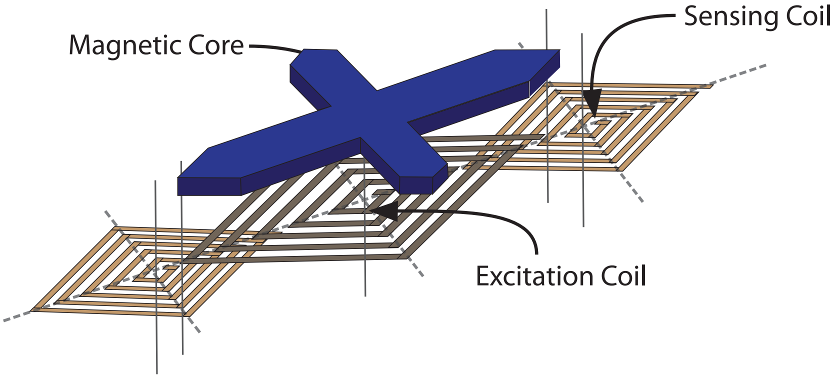

Figure 1.5: Structure of a planar Fluxgate magnetic sensor

the voltage induced in the two sensing coils is not the same and the differential output voltage increases its value, resulting in an amplitude modulation. With a suitable core shape, e. g. cross shape, and with four sensing coils the structure shown in Fig. 1.5 and Fig. 1.6 can be used as a double axis magnetic sensor. The structure can be realized on the top of an IC, achieving very small dimensions and low power consumption.

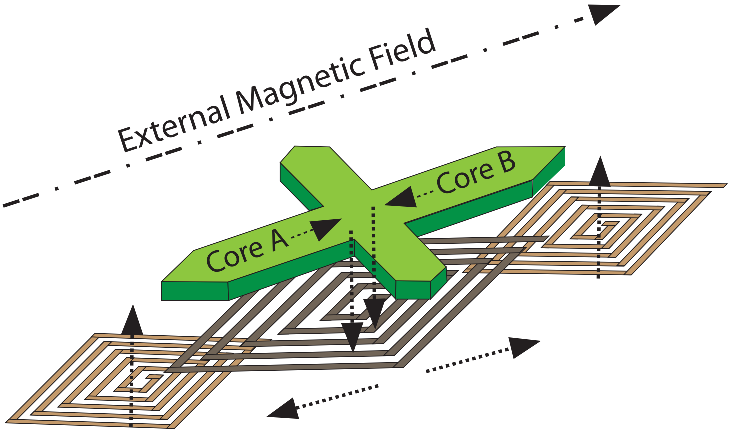

Figure 1.6: Structure of a planar Fluxgate sensor with an external magnetic field

1.3 Digital Compass System Characterization

In this section we describe the characterization of an electronic compass based on a Fluxgate sensor [9]. Before describing in detail the measurement setup, it is worth to provide a short introduction on the system, to explain the obtained experimental results. The measurement system consists of a Fluxgate sensor and an integrated front-end circuit, both realized in CMOS technology. The couple of orthogonal axes of the sensor makes the system suitable for realizing an electronic compass device. Indeed, this measurement system allows us to measure not only the amplitude of the Earth magnetic field (whose full-scale value is of the order of 60 µT), but also its direction. The complete measurement system achieves a maximum angular error of 1.5° in the measurement of the Earth magnetic field direction. An acquisition setup was developed to evaluate the measurement system performance. It consists of a precision mechanical plastic structure, in tower form, a microcontroller-based interface circuit, that provides a digital output through an RS232 serial interface, a PC software suitably developed to post-process the data from the acquisition system and a couple of Helmoltz coils to evaluate the linearity of the system. This setup allowed us to perform a completely automated and numerically controlled characterization of the measurement system. Fig. 1.7 shows the acquisition system and the relative measurement setup.

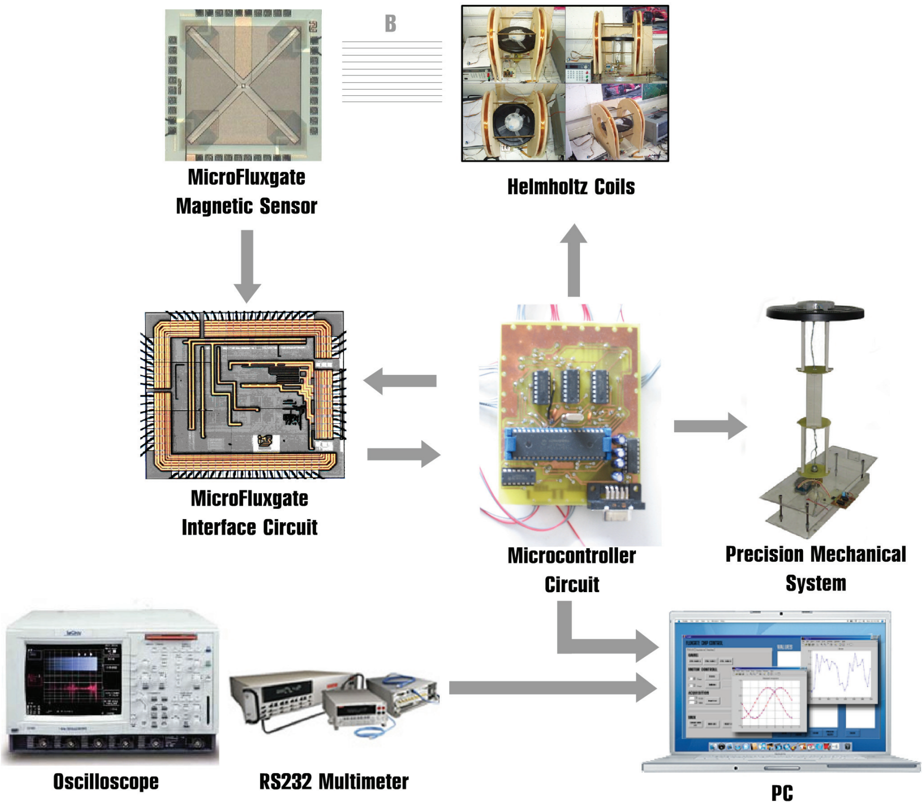

Figure 1.7: Measurement and acquisition systems interaction

1.3.1 Magnetic field measurement system

The Earth magnetic field measurement system consists of 2D planar fluxgate magnetic sensor and an integrated read-out circuit, for exciting the Fluxgate sensor and reading-out the magnetic field magnitude in digital domain.

Fluxgate sensor

When realized with integrated circuit technologies, the three-dimensional geometry of a Fluxgate sensor evolves in a planar structure [10, 11], as shown in Fig. 1.5. In this case, the excitation and sensing coils are implemented as spirals, realized with two different metal layers, while the magnetic core is usually obtained with a post processing of the silicon wafer. In Fig. 1.5 both magnetic axes are shown but, for simplicity, only a pair of sensing coils are indicated. This structure is able to detect a magnetic field coplanar with the structure itself, the output signal being proportional to the projection of the field along the directions of the two cross arms of the magnetic core. The integrated micro-Fluxgate used, whose photograph is shown in Fig. 1.8, has been developed in a 0.5 µm CMOS process and the ferromagnetic core is realized as a post-processing step by dc-magnetron sputtering. The obtained core features the good magnetic properties of the amorphous ferromagnetic material used as target (Vitrovac 6025 X), with a very small thickness (about 1 µm). The thickness was chosen as a compromise between the sensitivity of the device and the power consumption (the thicker the core, the higher is the current required to bring it into saturation). The used technology includes copper metal lines for the excitation coil and aluminum metal for the sensing coils. The total area of the planar copper excitation coil (5.5 µm, 71 turns and 12 µm pitch whose 8 µm metal width and 4 µm of spacing between two metals) is 1760 x 1760 µm^2 and its resistance is about 123.4 Ω. The total area for the aluminium sensing coils (1 µm thickness, 66 turns, 3 µm pitch with 1.4 µm metal width and 1.6 µm

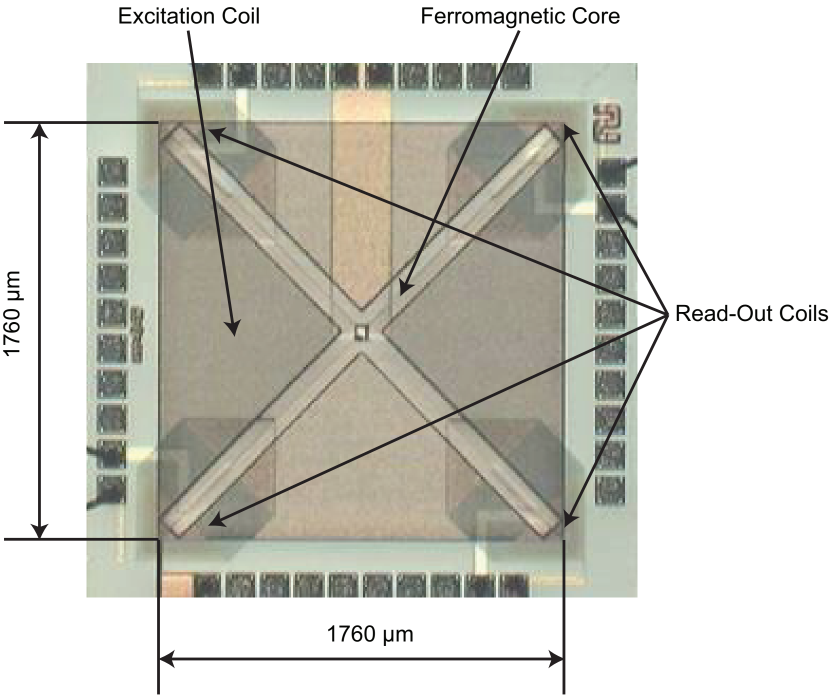

Figure 1.8: Fluxgate sensor micro-photograph

of spacing between two metals) is 650 x 650 µm^2 and their resistance is about 1.84 kΩ. According to the fluxgate sensor operating principle, when excited, the device provides at the sensing coils, two signal whose second harmonic spectral component is proportional to the amplitude of the external magnetic field in the corresponding direction.

Integrated read-out circuit

The integrated read-out circuit [12] consists of three main blocks: an excitation block to provide the required excitation current to the fluxgate sensor, a read-out block to process the sensor output and an A/D converter [13] to translate the analog output of the read-out chain into the digital domain. Fig. 1.9 shows the block diagram of the entire circuit. The circuit [12, 14] is quite flexible and can cope with Fluxgate sensors with different specifications, providing the current neces-

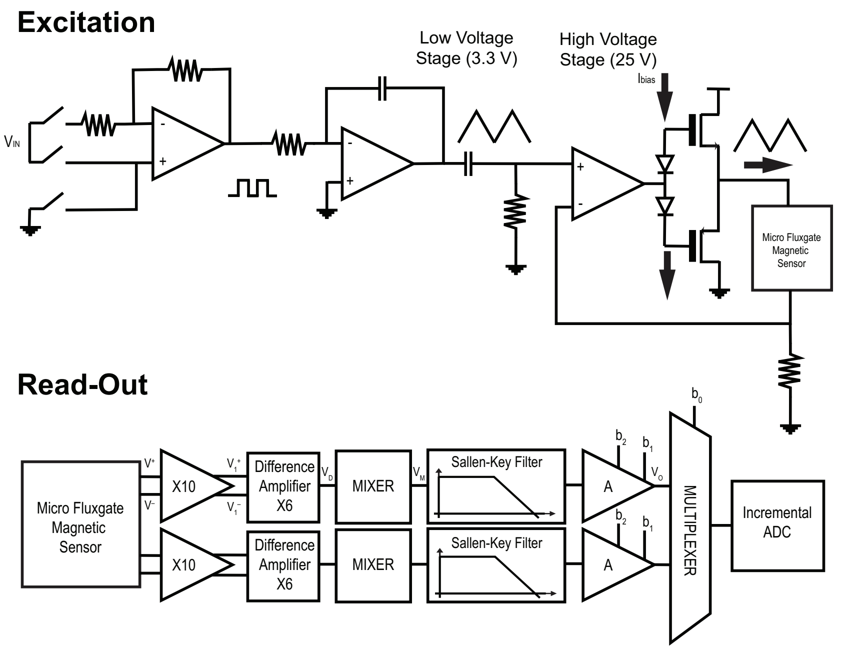

Figure 1.9: Block diagram of the integrated read-out circuit.

sary for their correct operation and reading-out the output voltage. This has two main consequences: first the excitation circuit output stage had to be implemented with a high voltage technology, in order to supply the required current (in the tens of milliampere range) into a wide range of coil resistances (with a worst case of 280 Ω); second the read-out block needs to have a programmable gain to accommodate the various amplitudes of the sensor output signals.

The excitation circuit consists of two different blocks, with two different power supplies: the first one is the low-voltage block, with a supply voltage equal to 3.3 V, while the second, realized with high-voltage transistors, uses a supply voltage up to 25 V. A linear, class-AB output stage has been used in order to minimize the distortion of the excitation current, and allow the interface circuit to excite sensors with different coil impedance. The first block generates a square wave with a frequency equal to 100 kHz and programmable output amplitude, which is then integrated, in order to obtain a triangular waveform, centered around half of the 3.3-V supply voltage. The excitation of the sensor with a triangular current waveform represents a trade-off between the low-noise performance of solutions based on sinusoidal excitation and the simple implementation of solutions based on pulsed excitation [15]. The second block consists of a high voltage mirrored operational amplifier with low-impedance output stage, which receives the triangular waveform at the input and, through a resistive feedback produces a triangular current at the output. A mirrored amplifier allows us to achieve the maximum swing at the output terminal. The class-AB output stage of the amplifier is designed to provide all the current required by the sensor. A decoupling stage between the low-voltage and the high-voltage blocks is necessary to level-shift the triangular wave produced by the low-voltage block around half of the high-voltage power supply.

In order to ensure proper timing for the excitation and read-out blocks, the whole circuit is driven by a clock at 400 kHz. This clock is internally divided by a cascade of flip-flops. The outputs of this timing circuit are two signals: a 100 kHz square wave signal with its complementary output, that is used to drive the excitation block, and a 200 kHz square wave signal used to drive the read-out block and to realize the second harmonic demodulation, needed to measure the sensor output. By using a 400 kHz master clock a duty cycle of 50% on both the 100 kHz and the 200 kHz output waveform can be ensured. A duty cycle different from 50%, indeed, could compromise the demodulation of the signals produced by the sensing coils and, therefore, it has to be avoided.

The two-channel sensor read-out circuit, shown in Fig. 1.9, is able to amplify the differential outputs of the sensing coils and to process the resulting signal, as illustrated in Fig. 1.10. Each channel of the read-out circuit consists of four different blocks. The first block is a gain stage that amplifies each of the two outputs of the

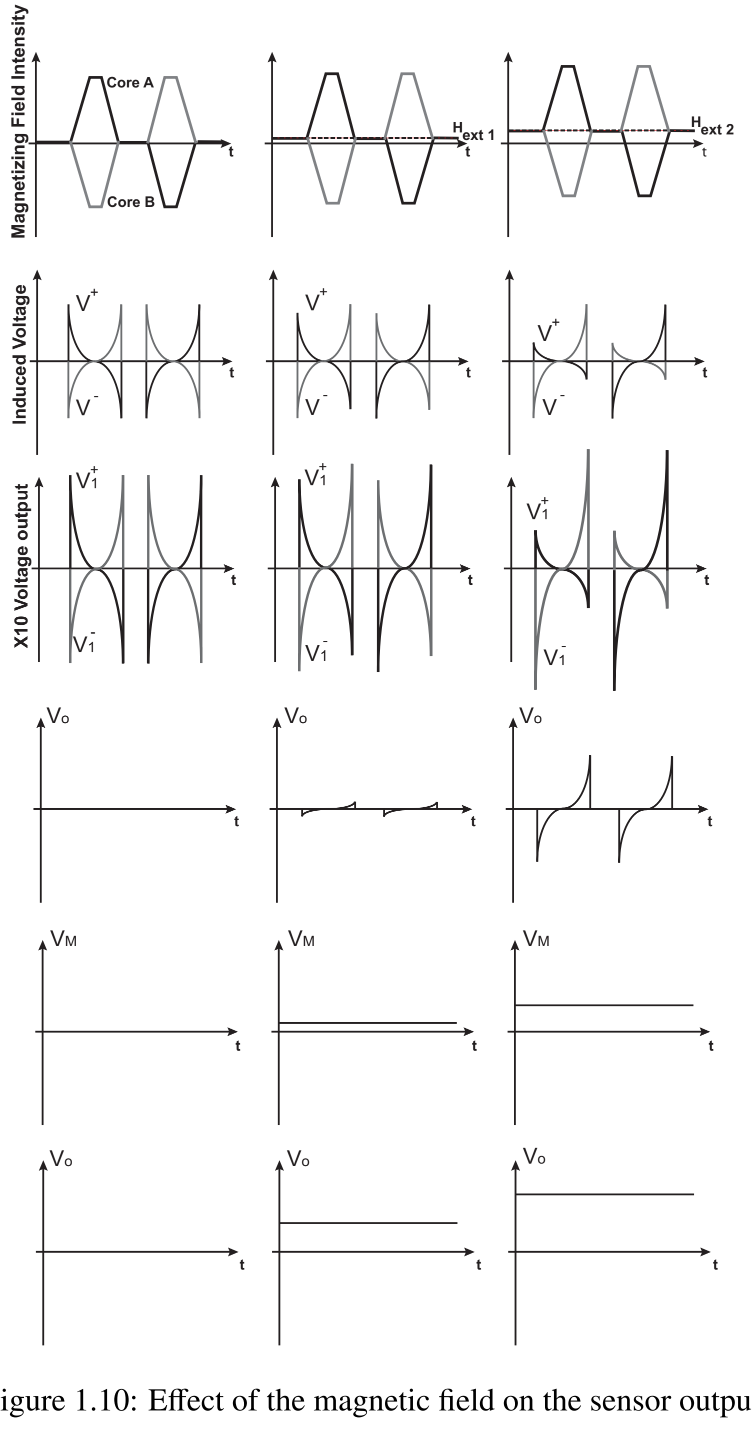

Figure 1.10: Effect of the magnetic field on the sensor output

sensing coils (V^+ and V^-) by a factor of ten. In the second block the difference between the two outputs of the first block (V_1^+ and V_1^-) is amplified again by a factor of six (V_D) and demodulated (V_M), to translate the second and higher order even harmonics, which contain information on the magnetic field, down to *dc*. In order to ensure the correct demodulation of the sensor signal and to avoid problems due to the possible asynchronicity between the clock and the output itself, a quadrature demodulation was implemented. Using this technique and adding together the contribution of the two orthogonal signals, it is possible to avoid errors due to timing misalignments between the read-out clock and the output of the sensor. The demodulation of the signal is performed with the 200 kHz clock generated by the timing circuit. The third block is a second order Sallen-Key low-pass filter that removes all the high frequency components resulting from the demodulation and returns a *dc* value that is proportional to the magnetic field. The difference between this output voltage and the analog ground is the amplified with a digitally programmable gain (from 1 to 100 with digital signals b_1 and b_2) in the last block (V_o). For all the blocks we used a conventional two-stages operational amplifiers. The *dc* output of the read-out chain is finally processed by a 13-bit incremental ADC, and delivered in digital form to the output interface. We used a single ADC with a multiplexer, driven by digital signal b_0 for both the read-out channels. Fig. 1.11 shows the micro-photograph of the integrated front-end chip. The chip has been fabricated with a 0.35 μm CMOS technology with high-voltage option. In order to minimize the presence of noise in the measurement process, we realized a dedicated printed-circuit board for characterizing the interface circuit chip. In particular, on the board we implemented several controls, such as multiplexer circuits, supply voltage filters, alternative discrete circuits to eventually bypass integrated corrupted sub-circuits. Fig. 1.12 and Fig. 1.13 show the layout and the photograph of the realized board, respectively.

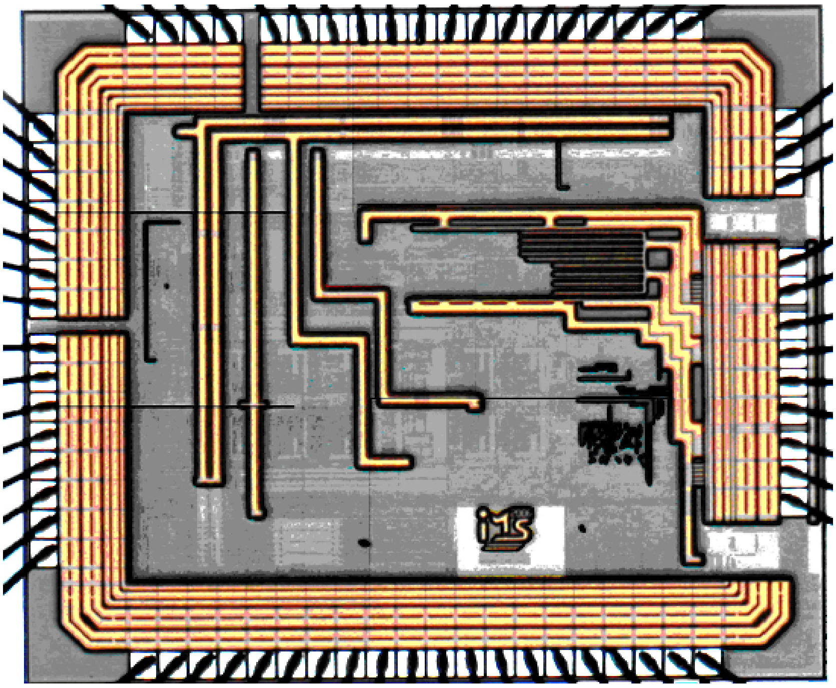

Figure 1.11: Microphotograph of the integrated front-end circuit

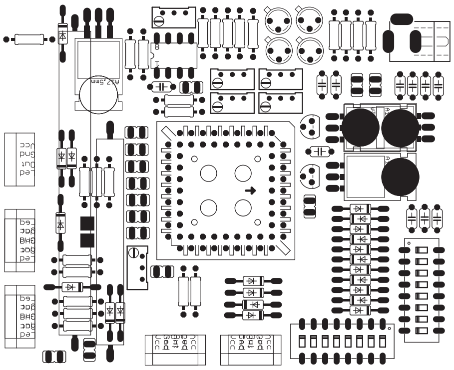

Figure 1.12: Layout of the magnetic sensor interface circuit board

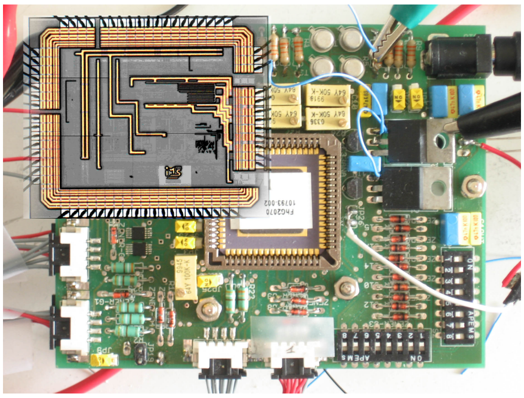

Figure 1.13: Photograph of the magnetic sensor interface circuit board

1.3.2 Automated acquisition system

To guarantee repeatability and reliability of the measurements, a fully automated acquisition system has been developed [16]. The acquisition system is the integration between mechanical and electronic subsystems. To make the measurement process completely automated, a microcontroller-based interface circuit was developed, together with a plastic rotating tower and a dedicated PC software. The automation of the process has allowed to improve the reliability of the measured data more that 50% with respect to a manual setup system.

Stepper motor control and precision rotating plastic tower

The positioning precision of the sensor in the Earth magnetic field is the most critical requirement in the design of the acquisition setup. The main contribution to the angular error obtained in previous manual approaches [12] is closely related to the mechanism of orientation of the sensor with respect to the direction of the external magnetic field. In order to ensure a high level of precision, the manual positioning has been substituted with an automated and numerically controlled process. In particular, we adopted a stepper motor, driven by an appropriate electronic interface. Stepper motors, differently than other motors, turn due to a series of electrical pulses to the motor windings. Each pulse rotates the rotor by an exact angle. These pulses are called ”steps”, hence the name ”stepper motor”. The rotation angle per pulse is set by the motor manufacturing and it is provided in the data-sheet of the motor. They can range from a fraction of a degree (i. e., 0.10°) for ultra-fine movements, to larger steps (i. e. 62.5°). The motor that we used was retrieved from an inkjet printer and provides 0.5 degree/pulse (dpp). In order to obtain a finest precision, a mechanical reduction has been introduced, thus allowing us to obtain a precision well below 0.1°.

Stepper motors consist of a permanent magnet rotating shaft, called the rotor, and electromagnets on the stationary portion that surrounds the motor, called the stator. In order to make the rotor move, the electromagnets of the stator must be excited with a proper sequence, composed of four steps. Whenever the sequence is not correct, the motor would be affected by vibration and noise, but it would not rotate. To explain the behavior of a stepper motor we can consider a simple example with 4 step per turn. This motor, showed in Fig. 1.14, consists of four electromagnets cross placed. In the center of the cross a magnet is free to rotate. A 360°rotation is implemented in four steps:

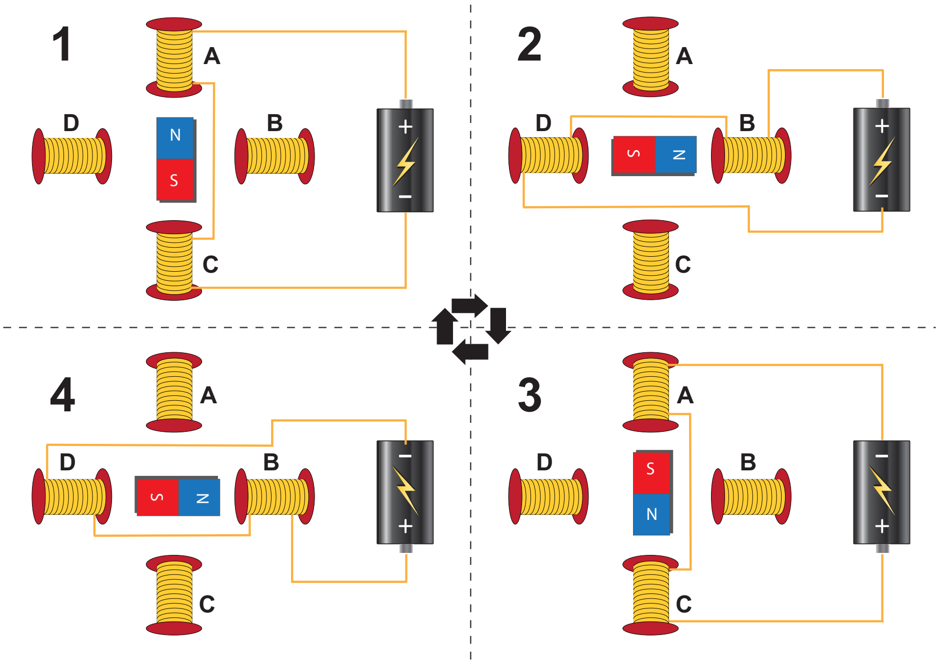

Figure 1.14: Example of stepper motor

- **STEP 1**

  Solenoids A(+) and C(-) are connected in series and are both excited. The rotor is oriented thus to have the *N* pole toward solenoid A, while the pole *S* is oriented in the direction of solenoid C. Therefore, the rotor is oriented in the vertical direction.

- **STEP 2**

  Solenoids B(+) and D(-) are connected in series and are both excited. The rotor is rotated of 90°CW.

- **STEP 3**

  Solenoids A(-) and C(+) are connected in series and are both excited, but with opposite polarity: the current flows in opposite direction, orientating the rotor with a 180°rotation with respect to STEP 1.

- **STEP 4**

  Solenoids B(-) and D(+) are connected in series and are both excited, with opposite polarity with respect to STEP 2. The magnet is rotated further by 90°CW.

In order to control the rotation speed it is enough to modulate the timing of excitations. To avoid any rotation while the system is retrieving data, the stator is constantly in stop mode. The current that flows through the stator coils is rather high (sometimes more than 100 mA). Therefore, a power electronic interface is necessary to drive them. The interface circuit consists of four drivers realized with the scheme shown in Fig. 1.15. The layout of the board implementing the circuit is reported in Fig. 1.16. Transistors T_1 and T_2 are Darlington structures (TIP122). Signal *Ph_in* is provided by a micro-controller and, therefore, the total available current is limited. The implemented solution allows us to exploit the current driving capability of an external supply generator to provides the needed voltage V_M and the required currents. In particular, when *Ph_in* is low T_1 is off, and its collector current is zero. The base voltage of T_2 is then given by

$$V_{B2} = V_{Motor} - I_{B2}R_2 \simeq V_{Motor} \tag{1.16}$$

were I_{B2} is the base current of T_2. Voltage V_{B2} guarantees that T_2 is on, thus providing the required current to the stator solenoid of the motor, connected to *Ph_out*. When *Ph_in* if high, T_1 is on, and V_{B2} is zero, thus turning off T_2. The

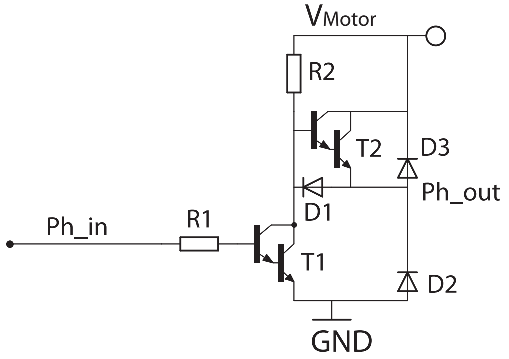

Figure 1.15: Driver adopted to excite a single solenoid of the stator

[t!]

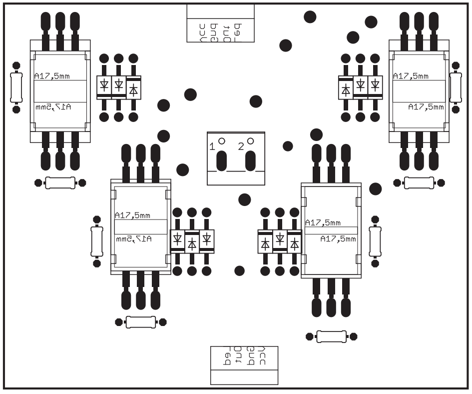

Figure 1.16: Layout of the motor driver board

current delivered to the motor is then zero. Diodes D_1, D_2 and D_3 avoid the back circle of current from the inductive solenoids of the motor.

To avoid any magnetic interaction between the step motor and the Fluxgate sensor a plastic tower has been developed. The complete motor controlled structure is shown in Fig. 1.17. The entire structure is made of plastic components, including the mechanical coupling, in order to avoid any perturbation of the Earth magnetic field. The only metal part is the stepper motor, which is therefore placed at 50 cm distance from the Fluxgate magnetic sensor. Such a mechanical system allows us to control the angular positioning with less than 0.1°accuracy, thus ensuring the

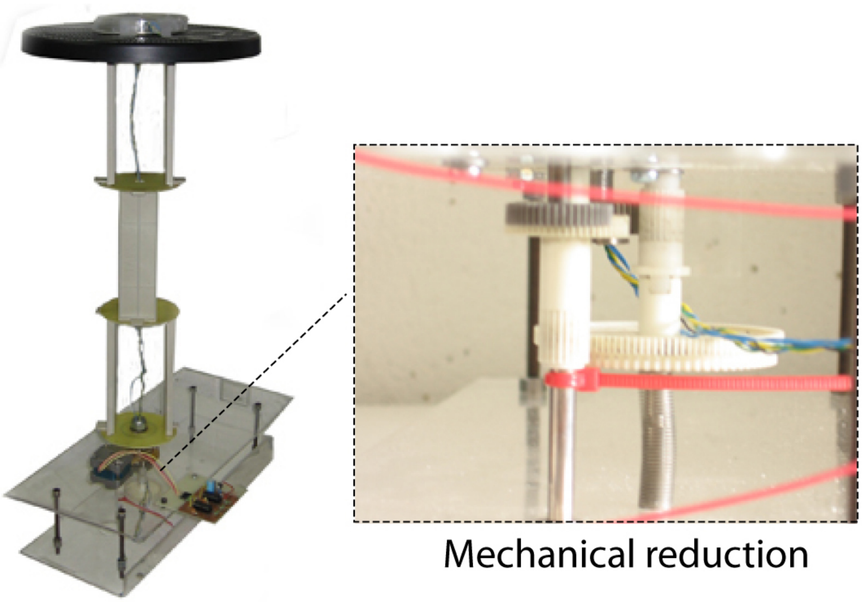

Figure 1.17: Plastic tower

repeatability of the measurements.

Microcontroller-based interface circuit

In order to automate the acquisition process a microcontroller-based management system has been realized. The core of the system is a PIC16F877A by Microchip®. This micro-controller (MCU) provides 40 pins, and 33 can be set as digital input-output ports. In Appendix A the pinout of the MCU is reported, while Fig. 1.18. shows the micro-controller board In order to provide the correct digital signals to the interface circuit chip we set 16 of the MCU ports as digital outputs. In particular, the micro-controller controls the gain and the signal multiplexing in the Fluxgate interface circuit, as well as the synchronized precision mechanical structure for rotating the system. Moreover, it acquires the digital data provided by the ADC implemented on the interface circuit chip. Finally it implements the interfacing between the acquisition system and the PC application specifically de-

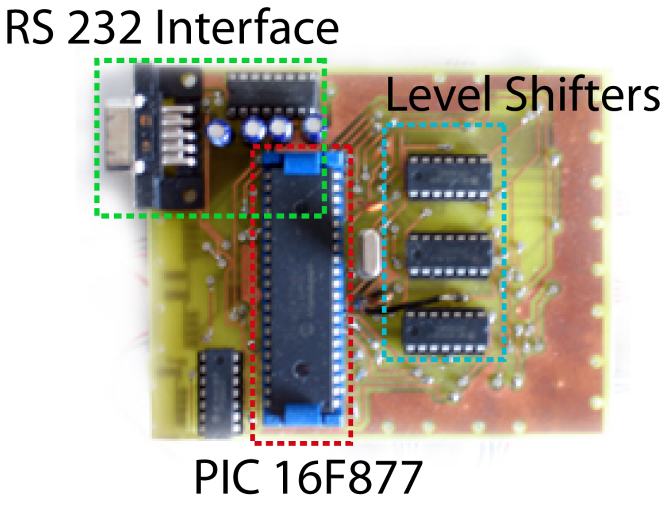

Figure 1.18: Board of the microcontroller-based interface circuit

veloped. The clock frequency of the MCU is 40 MHz. The required 5 V power supply is generated on the interface circuit board. Since the interface circuit chip is supplied with 3.3 V, level shifter have been used. To control the gain and the signal multiplexing of the interface circuit, five dedicated digital pins are used. Moreover, four additional pins are used to generate the four phases required to control the stepper motor of the plastic rotating structure. Finally, 13 input digital pins allow the acquisition in parallel mode of the output of the read-out circuit ADC. The firmware of the MCU has been developed specifically for this application in high-level language, without any performance loss. Table 1.1 summarizes the connections between the micro-controller and the Fluxgate interface circuit chip.

1.3.3 Dedicated software

A dedicated software was developed to control and supervise the entire acquisition process. The front panel of the software is shown in Fig. 1.19. It is a MS Windows based application written in C++ high level language, which manages the data

Table 1.1: MCU control pins

PIC 16F877 Pin	Interface Circuit Pin
RD0	Motor phase 1
RD1	Motor phase 2
RC2	Motor phase 3
RC3	Motor phase 4
RD5	Control Gain 1 (b2)
RD4	Control Gain 2 (b1-1)
RD3	Control Gain 3 (b1-2)
RA4	Mux Control 1
RA5	Mux Control 2
RE(2..0)	BIT(0..2) ADC
RC(1,0)	BIT(3,4) ADC
RD2	BIT5 ADC
RB(1..7)	BIT(6..12) ADC
RB0	EOC ADC
RC4	OVERFLOW ADC

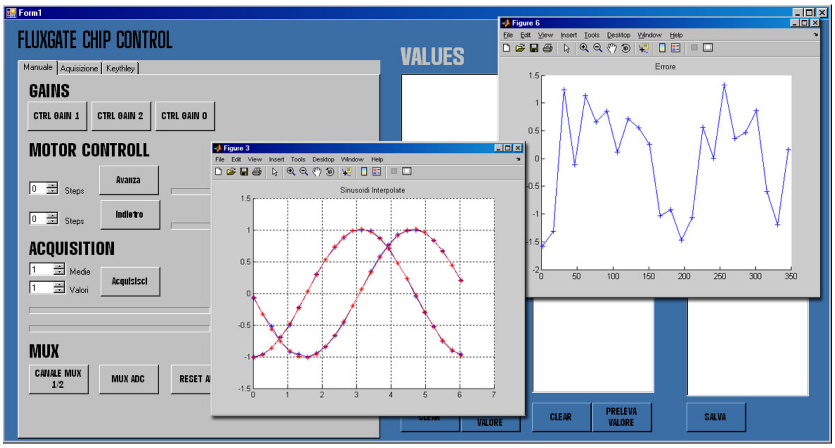

Figure 1.19: Front panel of the software

acquired from the micro-controller. In particular, it is possible to customize the number of acquisitions to average and the number of steps over 360°, it compares analog and digital acquisitions and it manages the compatibility of the files to be processed with Matlab. Furthermore it can verify the measurement setup with dedicated system check software routines.

1.3.4 Acquisition system optimization

The proposed fully automated acquisition setup is the result of an optimization process, which started from a manual approach. In the very first acquisition setup, the sensor was mounted on a plastic disc, which was manually rotated upon a table with 5°reference marks. The output signal of the sensing coils was subtracted by means of a simple operational amplifier based circuit (because of coupling effects it was not possible to simply connect the sensing coils in anti-series). The difference was further amplified with a gain of 100 and read-out with a spectrum analyzer. In spite of the intrinsic sensitivity of the spectrum analyzer this approach lead to a maximum angular error of about 4.5°. Partially this was caused by the manual rotation of the system and partially by the fact that, because of the time required by the spectrum analyzer to make a measurement, a single acquisition per position was performed. A first improvement was the introduction of the integrated read-out circuit, which provides a *dc* voltage directly proportional to the measured field: this signal is available continuously and it is easier to perform an average over a number of subsequent measurements. At this stage the internal average of a Keithley 2000 multimeter was used.

Finally, the proposed acquisition system was introduced, providing a number of benefits:

- the system has a high degree of integration, even in the auxiliary circuitry, helping in improving the signal-to-noise ratio;
- the chance of making errors while reading the data is strongly reduced;
- the precision of the mechanical rotation is as high as 0.1°;

- speed is maximized.

This last characteristic is relevant, since it allows to increase the number of averaged acquisitions for a given position and for a given total time required for a full rotation. Alternatively, the time required for the 360°rotation can be minimized for a given number of averages, lowering the probability of local magnetic perturbation during the measurement (it is worth stressing the fact that the used approach measures the actual Earth magnetic field). In general this automatic acquisition system allows measurements to be performed with up to 720 steps, leading to a much finer angle discretization than the 5°used for the manual rotation. The angular accuracy in the reconstructed position is then improved, as shown in Fig. 1.20. All the values of angular accuracy reported in Fig. 1.20 are calculated by applying fixed calibration coefficients for correcting offset and gain differences between the two axes (for each setup the coefficients are determined from one measurement and the used for any further measurements).

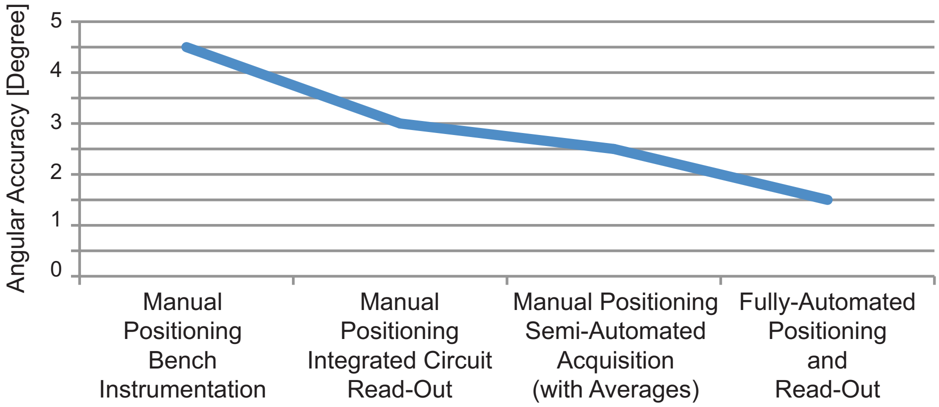

Figure 1.20: Angular accuracy as a function of the acquisition system evolution

1.3.5 Experimental results

The entire acquisition system is fully automated. All the mechanical, electronic and software components have been developed for this particular application. With this acquisition system, the angular accuracy of the measurement system has been pushed down to 1.5°, when rotating the system in the Earth magnetic field, as shown in Fig. 1.21. This is the intrinsic performance of the magnetic field measurement system, but we were able to measure it only with the new acquisition system. The presented system allows to minimize the contribution of noise and precision loss due to the setup, and to maximize the mechanical and electronic precision. In particular with a numerically control approach it has been possible to evaluate the real performance of the measurement system, achieving an improvement of more than 50% respect to the evaluation made with previous manual acquisition systems. The angular accuracy achieved with the automated

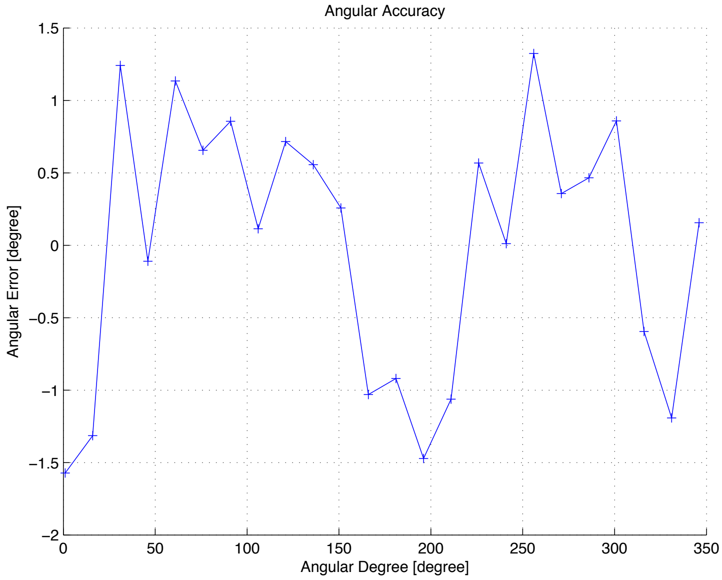

Figure 1.21: Angular accuracy achieved with the automated acquisition system

acquisition system is limited only by the fluxgate sensor and the read-out circuit, thus allowing the actual performance of the device to be evaluated. Fig. 1.22 reports the data acquired from the two axes of the sensor during the complete rotation. The results reported are referred to a 24-point acquisition along 360°. The linearity of the entire system in the range of ±60 µT has been evaluated acquiring the output of the sensor while varying the intensity of the magnetic field with Helmholtz coils. In order to ensure the reliability of the linearity measurement, the axis of the sensor under test has been oriented in the direction perpendicular to the Earth magnetic field, i.e. the sensor has been rotated in order to acquire the maximum and the minimum voltage output, and it has been stopped in the middle position. This guarantees a negligible contribution of the Earth magnetic field to the field impressed with the Helmholtz coils. In this measurement we achieved a maximum linearity error of 3% of the full-scale, as shown in Fig. 1.23. The

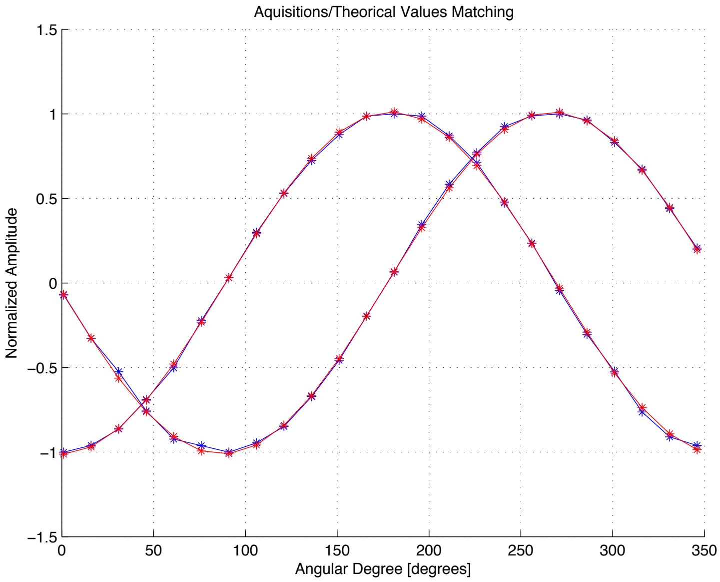

Figure 1.22: Data acquired from the sensor over 360°with the automated acquisition system

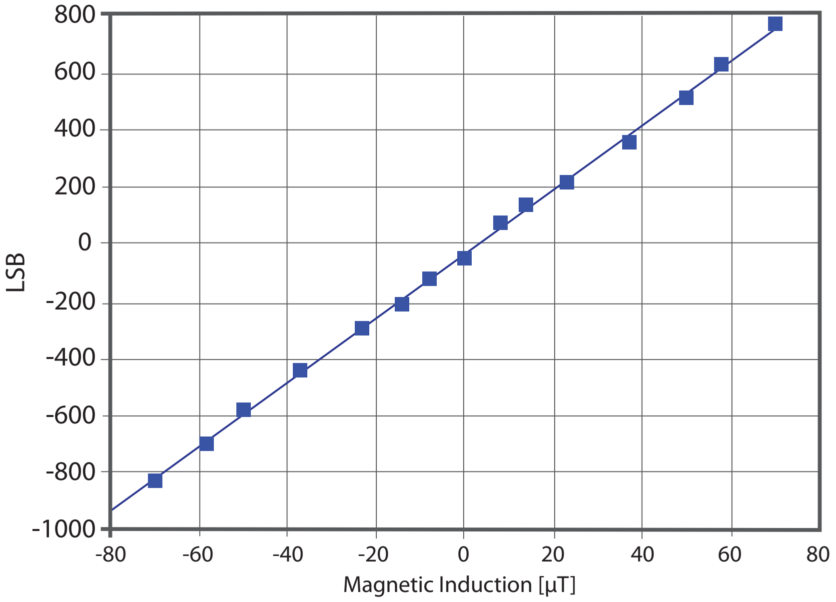

Figure 1.23: Linearity of the complete system

sensitivity obtained is 11 LSB/µT that corresponds to 0.45 mV/µT, considering a 300-mV ADC input voltage swing. All the data collected are in agreement with the performance of the sensor stand-alone, previously measured with dedicated test equipment [12].

1.4 Re-Design of the Fluxgate Magnetic Sensor Interface Circuit

In this section a re-design of the Fluxgate magnetic sensor interface circuit is presented. The new interface circuits targets current measurement applications instead of electronic compasses. The re-design was aimed to reduce the supply voltage and the power consumption of the available interface circuit, thus achieving a complete low-voltage, low-power and high linearity device. The integrated circuit provides the correct excitation signal to the Fluxgate sensors and reads-out the sensor signals from the sensing coils. The designed circuit allows us to deal with sensors featuring different values of the excitation coil resistance and to process the sensing coil signals with a power consumption lower than 1 mW. The interface circuit consists of three different modules, namely a timing block, an excitation block and a read-out chain. The interface circuit, has been implemented with two different excitation circuits, operating at 5 V and 3.3 V, respectively, without any high-voltage process options. The read-out chain performs a synchronous demodulation of the even harmonics, in order to extract the value of the external magnetic field. Furthermore, it is possible to switch-on a 13 bit ADC, to provide at the output the demodulated signal as a digital word.

1.4.1 Introduction

When Fluxgate magnetic sensors are used for current measurements, the electronic interface circuit plays an important role, since it must guarantee high linearity, low-power consumption (for portable applications), reliable results and high magnetic noise rejection. The designed circuit allows us to excite sensors with different values of the excitation coil resistance and to process the sensor signals. The chip consists of three different modules, namely a timing block, an excitation block and a read-out chain. The interface circuit, whose block diagram is shown in Fig. 1.24, has been implemented with two different excitation circuits, operating at 5 V and 3.3 V, respectively, without any high-voltage stage [17]. The read-out circuit allows us to retrieve the information on the external magnetic field from the sensing coil signal. In the interface circuit, we included also a 13 bit ADC [13], to provide the measured magnetic field value as a digital word. The timing block provides control signals for both excitation and sensing. In the considered current measurement application, we have used a fluxgate sensor with an excitation coil featuring 140 Ω resistance and 4 μH inductance, which needs to be excited with a 23 mA current signal with odd symmetry at 100 kHz [10].

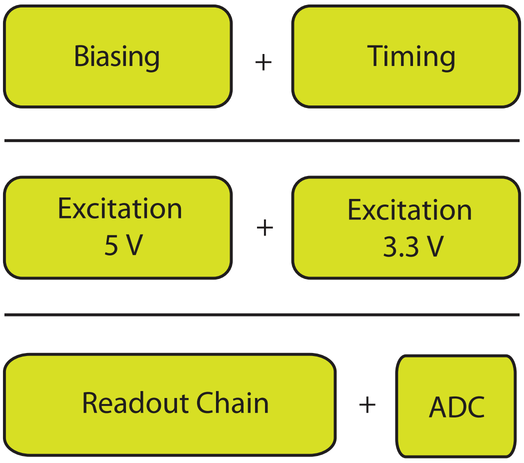

Figure 1.24: System block diagram

1.4.2 Excitation circuits

As already mentioned, we implemented two different excitation circuits, namely a 3.3 V supplied circuit and a 5 V supplied circuit. The first circuit requires the use of an external inductance, while the second is fully integrated. Both circuits provide a 36 mA triangular excitation current at 100 kHz.

3.3-V excitation circuit

Fig. 1.25 shows the excitation circuit operating at 3.3 V. It consists of an H-Bridge, which exploits an external inductance to generate a triangular current excitation signal starting from a square-wave voltage signal. In order to achieve the desired excitation signal, the value of the external inductance is 380 μH. The external 3.3-V, 400-kHz clock, after frequency division by 4, drives the H-Bridge with two opposite square waves at 100 kHz. R_s and L_s represent respectively the resistance and the inductance of the sensor (140 Ω and 4 μH), while L_{ext} represents the 380 μH external inductance needed to obtain the correct parameters of the excitation current signal.

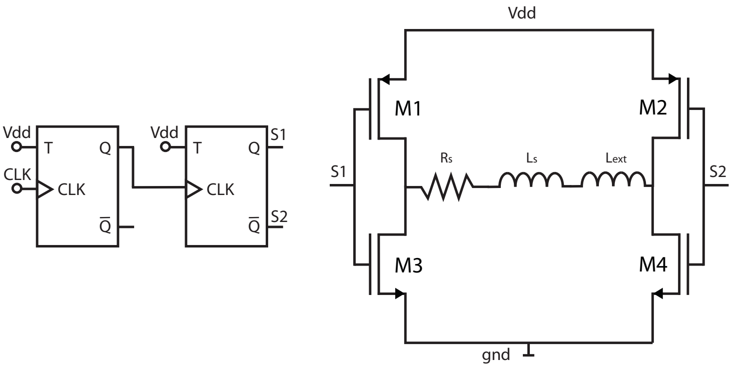

Figure 1.25: Schematic of the 3.3 V excitation circuit

Signals S_1 and S_2 switch at 100 kHz. The aspect ratio of all transistors is 10 mm/0.4 μm. Fig. 1.26 shows the excitation current waveform obtained in simulation.

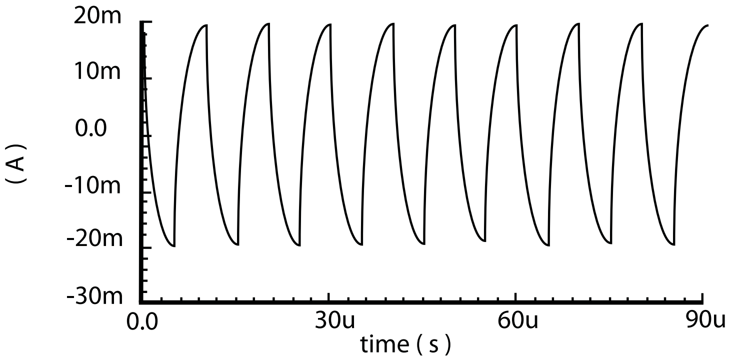

Figure 1.26: Excitation current waveform obtained in simulation with the 3.3-V excitation circuit

5-V excitation circuit

Fig. 1.27 shows the excitation circuit with 5-V power supply. It consists of a triangular wave generator, a voltage driven current generator, a current mirror, and a H-Bridge. The triangular wave generator provides a 130-mV signal around 2.5 V, obtained by integrating the frequency-divided clock and level-shifting it around the proper average value. It is possible to modulate the amplitude of the

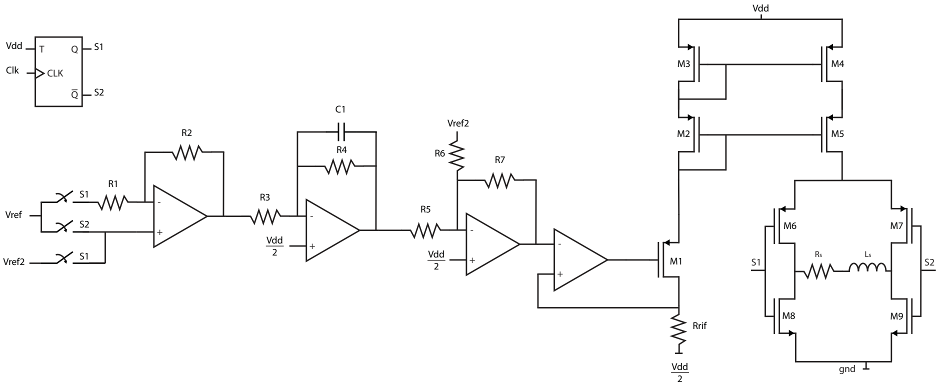

Figure 1.27: Schematic of the 5-V excitation circuit

signal changing the value of V_{ref}. The Wilson current mirror amplifies the current by $K = 10$, thus leading to a 20-mA peak current signal. The 200-kHz H-Bridge driving signals are used to switch alternatively the direction of the current flowing into the excitation coil of the sensor. In particular, when signal $S1$ is high and signal $S2$ is low, transistors $M3$ and $M7$ are switched-on, while transistors $M6$ and $M5$ are switched-off. During this period, the current flowing through the sensor is KI_{ref}. By contrast, when signal $S1$ is low and signal $S2$ is high, transistors $M6$ and $M5$ are switched-on, and the excitation current flowing through the sensor is $-KI_{ref}$. As a result, the sensor is excited with a 40-mA peak-to-peak current, as required. Without the H-Bridge, this behavior would have been possible only with a symmetric supply voltage (±5 V).

Triangular waveform generator

Fig. 1.28 shows the schematic of the circuit used to generate the triangular waveform of the excitation signal at a frequency of 100 kHz. Table 1.2 summarizes the parameters of the devices used in the circuit of Fig. 1.28. The main clock signal is at 400 kHz, and it is provided from outside the chip. A flip-flop is used as frequency divider, providing signals S_1 and S_2 at 200 kHz. When S_1 is high and S_2 is

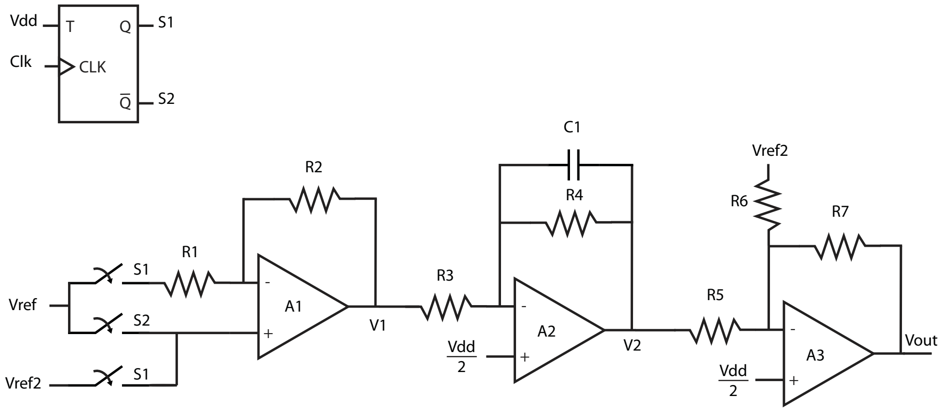

Figure 1.28: Triangular waveform generator

Table 1.2: Design parameters of the triangular waveform generator

R_1	R_2	R_3	R_4	R_5	R_6	R_7	C_1
37 kΩ	37 kΩ	1.25 MΩ	1 MΩ	37 kΩ	37 kΩ	37 kΩ	1pF

low, the first operational amplifier is in inverting configuration with a gain equal to −1 (R_1 and R_2 are equal), and $V_1 = -V_{ref}$. Then, when S_1 becomes low and S_2 high. A_1 is buffer connected, and $V_1 = V_{ref}$. The second stage, A_2, is a Miller integrator. The transfer function of the integrator is given by

$$A_S = -\frac{R_4}{R_3}\frac{1}{1 + sR_4C_1} \tag{1.17}$$

The frequency of the pole in equation (1.17) is

$$p = -\frac{1}{2\pi R_4C_1} \tag{1.18}$$

Amplifier A_3 provides a shifting of the average value of V_2. V_{out} is a triangular voltage signal at 200 kHz with a peak-to-peak value of 130 mV. The average value is 2.5 V. Fig. 1.29 shows the waveform obtained in simulation at the output of the triangular waveform generator.

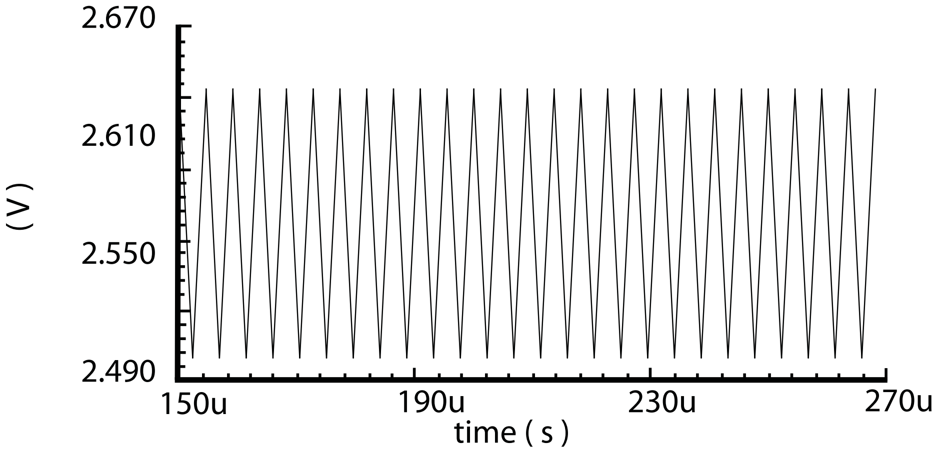

Figure 1.29: Waveform obtained in simulation at the output of the triangular waveform generator

Voltage-driven current generator

The excitation of the sensor requires a precise current signal. Fig. 1.30 shows the solution adopted to transform the voltage signal obtained at the output of the triangular signal generator into a current. Current I_{ref} is given by

$$I_{ref} = \frac{V_{in} - \dfrac{Vdd}{2}}{R_{rif}} \tag{1.19}$$

where V_{in} varies between 2.63 V and 2.5 V. In order to obtain a 2 mA current signal, R_{rif} has been set to 135 Ω.

I_{ref} is a triangular waveform at the same frequency of V_{in} (200 kHz). The current mirror implements a gain of 10, providing to the load (Fluxgate sensor) an excitation current of

$$K \cdot I_{ref} = 10 I_{ref} \tag{1.20}$$

Table 1.3 summarizes the dimension of the transistors of the voltage-driven current generator. Fig. 1.31 shows the current waveform provided to the H-bridge obtained in simulation.

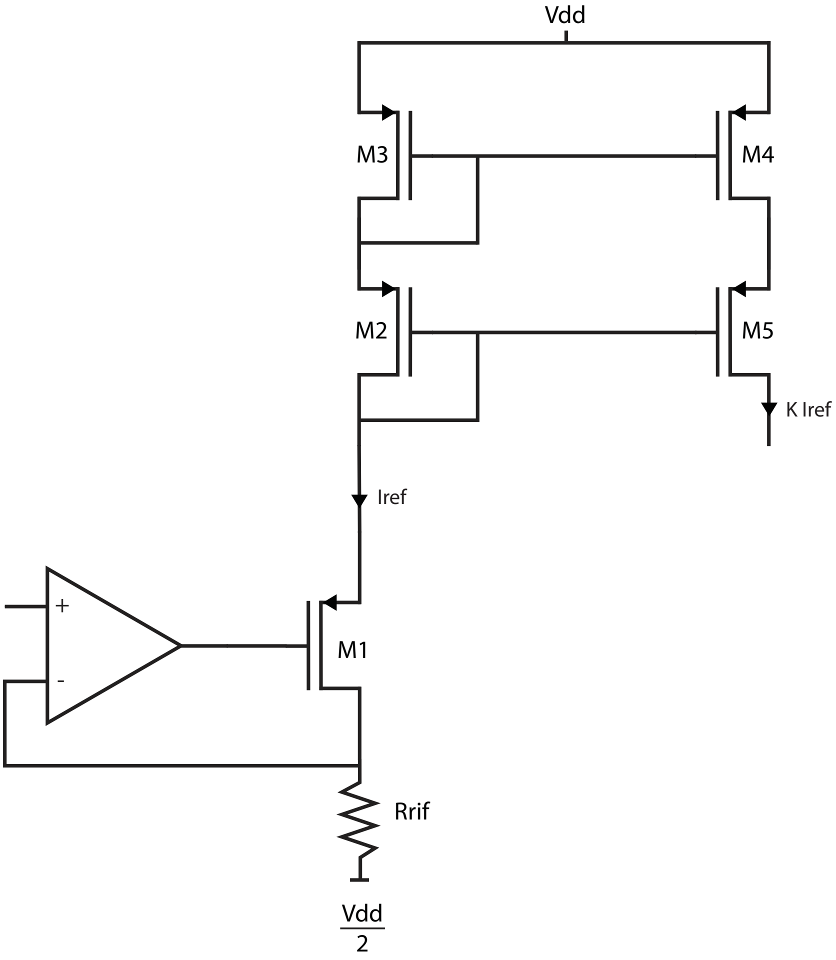

Figure 1.30: Schematic of the voltage-driven current generator

H-bridge

In order to provide the proper excitation current to the Fluxgate sensor we would need a supply voltage value equal to

$$140\,\Omega \cdot 46\ \text{mA} = 6.44\ \text{V} \tag{1.21}$$

but the available supply voltage is only 5 V. Therefore, a full H-Bridge solution has been adopted, to effectively double the allowed voltage drop across the sensor with a single 5-V supply voltage. In particular, with the circuit scheme of

Table 1.3: Design parameters of the of the voltage-driven current generator

M_1	M_2	M_3	M_4	M_5
$\frac{400\mu m}{0.5\mu m}$	$\frac{400\mu m}{0.5\mu m}$	$\frac{400\mu m}{0.5\mu m}$	$\frac{4000\mu m}{0.5\mu m}$	$\frac{4000\mu m}{0.5\mu m}$

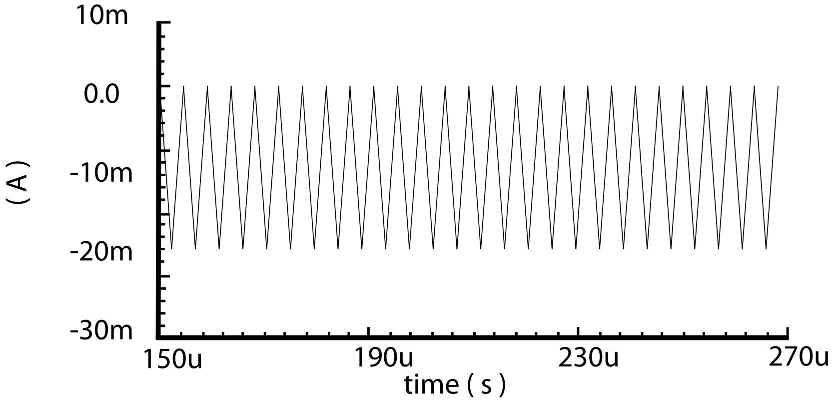

Figure 1.31: Current waveform delivered to the H-bridge obtained in simulation

Fig. 1.32, the 10 mA current provided by the voltage-driven current generator flows in both direction through the Fluxgate sensors excitation coils, thus saturating the ferromagnetic core alternatively, according to the hysteresis curve. When S_1 is high and S_2 is low, M_3 and M_7 are on, while M_6 and M_5 are off. In this condition the current that flows through the sensor is $K \cdot I_{ref}$. When S_1 is low and S_2 is high M_3 and M_4 switch-off and M_5 and M_5 switch-on. In this case the excitation current becomes $-K \cdot I_{ref}$. The switching of S_1 and S_2 is at 200 kHz, thus exciting the sensor with a current at 100 kHz and double amplitude. Fig. 1.33 shows the excitation current obtained in simulation from the designed circuit.

1.4.3 Read-out chain

Fig. 1.34 shows the block diagram of the read-out chain. The pick-up coils of the

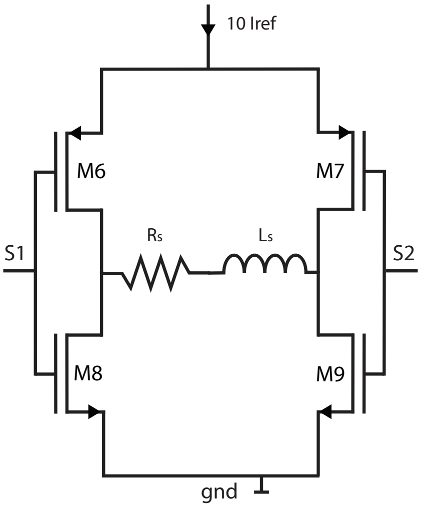

Figure 1.32: Full H-Bridge circuit scheme

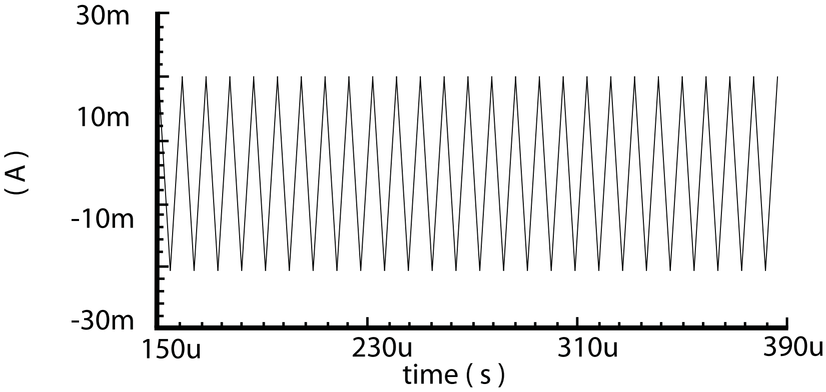

Figure 1.33: Current waveform delivered to the sensor obtained in simulation

planar fluxgate magnetic sensor detect the signal induced by the rising and falling edges of core magnetizing current (Fig. 1.35). As well known, the frequency of the differential voltage produced by the pick-up coils is twice the frequency of the excitation current. Therefore, it is possible to extract the information on the external magnetic field by a synchronous demodulation. The single-channel sensor readout circuit is able to measure the outputs of the sensing coils and to process the resulting signal. The channel of the readout circuit consists of four

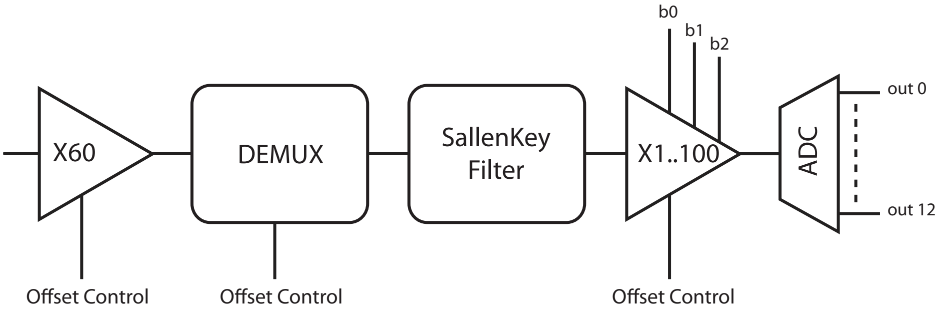

Figure 1.34: Block diagram of the read-out chain

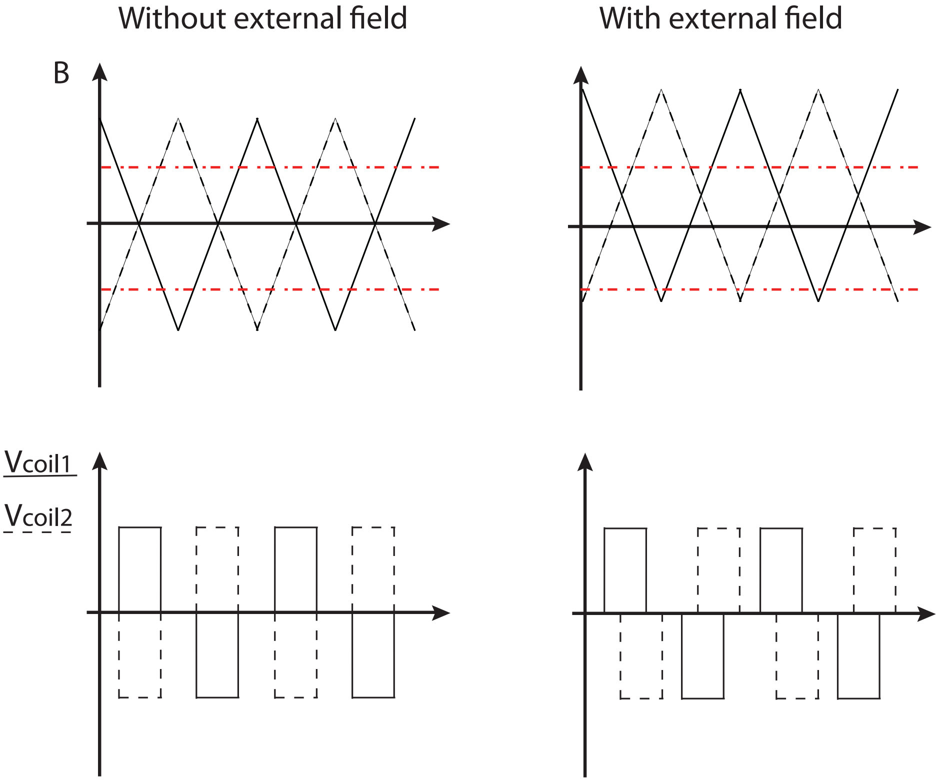

Figure 1.35: Effect of the external magnetic field over the sensor

different blocks. The first block is a gain stage that amplifies each of the two outputs of the sensing coils by a factor of 60. In the second block then the signal is demodulated. In order to ensure a correct demodulation of the sensor signal and to avoid problems due to the asynchronicity between the clock and the output of the sensor itself, a quadrature demodulation has been implemented. Using this technique and adding together the contribution of the two orthogonal signals, it is possible to avoid errors due to timing misalignments between the readout clock and the output of the sensor. The readout process is done at a frequency equal to 200 kHz. The third block is a second order Sallen-Key low-pass filter that removes all the high frequency components resulting from the demodulation and returns a DC value that is proportional to the magnetic field. The difference between this output voltage and the analog ground is then amplified with programmable gain (from 0 to 100) in the last block.

In order to achieve low power consumption, we adopted the following solutions:

- single read-out circuit;
- dedicated operational amplifiers with low power consumption.

Therefore, we designed the following blocks:

- low charge injection switches;
- low output resistance operational amplifier with a bandwidth of 200 kHz, with low power consumption;
- low output resistance operational amplifier with a bandwidth of 10 kHz, with low power consumption;
- coherent quadrature demodulator;
- Sallen-Key filter with a bandwidth of 500 Hz;
- variable gain operational amplifier.

Switches

All the switches used in the interface circuit have to feature low charge injection and clock feed-through. To reduce the clock feed-through a transfer-gate configuration has been adopted, with a couple of complementary MOS transistors driven by two opposite phases. In order to minimize the charge injection, we used dummy-switches. Considering the simple circuit shown in Fig. 1.36, we can assume that, when the switch turn off, half of the channel charge flows trough the drain, and half through the source. Therefore, the charge collected by capacitor C$_H$ is given by

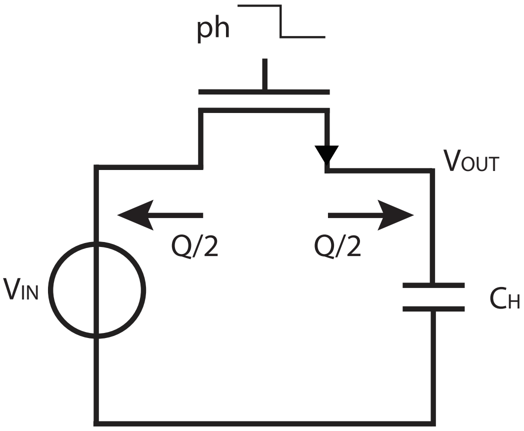

Figure 1.36: Charge injection

$$\Delta Q_H = \frac{C_{OX}WL(V_{GS} - V_{Th})}{2} \tag{1.22}$$

where V$_{Th}$ is the threshold voltage of the MOS transistor. We can estimate the relative variation of V$_{OUT}$ as

$$\Delta V_{OUT} = \frac{C_{OX}WL(Vdd - V_{in} - V_{Th})}{2C_H} \tag{1.23}$$

In order to estimate the clock-feedthrough effects we can refer to Fig. 1.37. On the falling edge of the clock, the parasitic gate capacitance of the n-MOS realizes

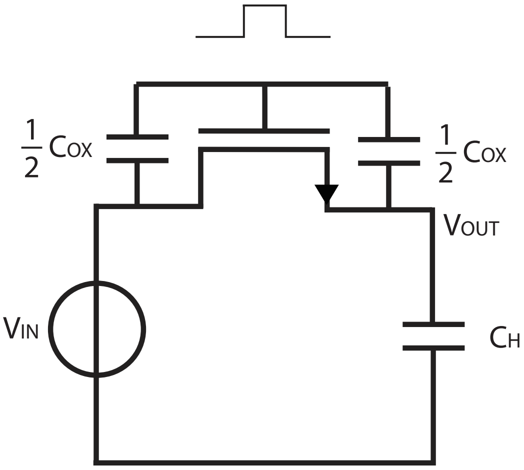

Figure 1.37: Clock feed-through

a capacitive divider with C_H. The variation of V_{OUT} results

$$\Delta V_{OUT} = \frac{C_0}{C_0 + C_H} Vdd \tag{1.24}$$

where C_0 is the parasitic capacitance, given by

$$C_0 = C_{OX} W L_D \tag{1.25}$$

L_D being the length of the overlap area between drain/source and gate. Fig. 1.38 shows the implemented circuit solution, while Table 1.4 summarizes the transistor dimensions.

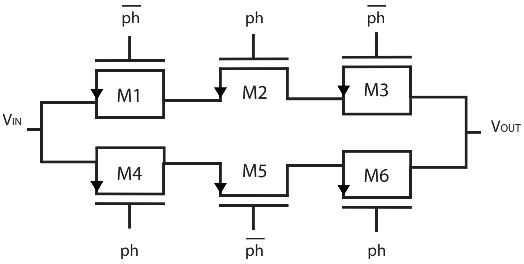

Figure 1.38: Schematic of the switches

Table 1.4: Transistors dimensions of the switches

M_1	M_2	M_3	M_4	M_5	M_6
$\frac{30\mu m}{0.35\ \mu m}$	$\frac{60\ \mu m}{0.35\ \mu m}$	$\frac{30\ \mu m}{0.35\ \mu m}$	$\frac{30\ \mu m}{0.35\ \mu m}$	$\frac{60\ \mu m}{0.35\ \mu m}$	$\frac{30\ \mu m}{0.35\ \mu m}$

Operational Amplifier

Fig. 1.39 shows the schematic of the operational amplifiers used in the integrated interface circuit. The same circuit architecture, but with different design parameters, has been used for all the amplifiers of the circuit:

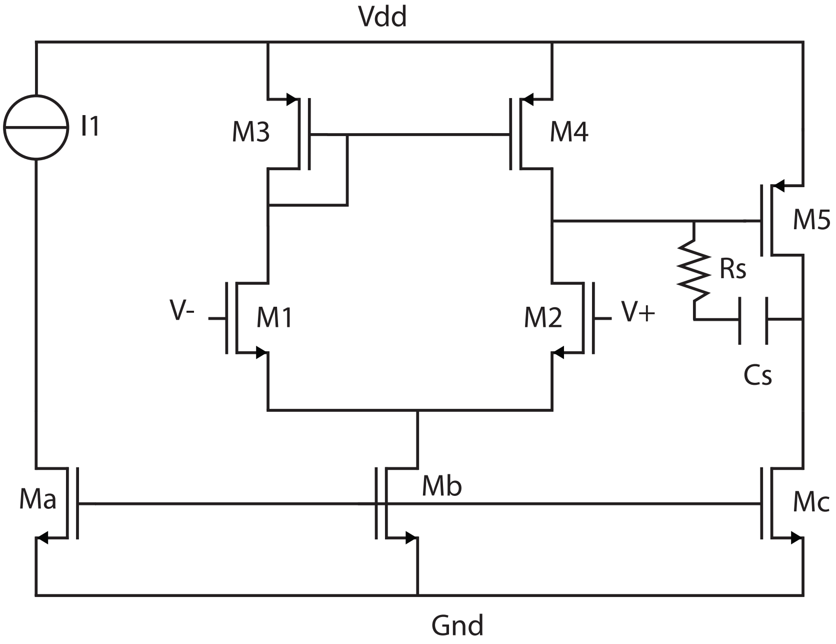

Figure 1.39: Schematic of the operational amplifiers

- before the demodulator (large bandwidth);
- after the demodulator (narrow bandwidth).

The amplifiers used before and after the demodulator are different in terms of transistor dimensions and bis current, thus featuring different power consumption, bandwidth and gain.

The structure of Fig. 1.39 consists of two stages. The low-frequency gain is given by

$$A_v = A_1 A_2 = \frac{g_{m1} g_{m5}}{(g_{m2} + g_{m4})(g_{m5} + g_{mc})} \tag{1.26}$$

To study the operational amplifier behavior at high frequency, we can refer to the equivalent circuit shown in Fig. 1.40. Resistor R_1 represents the output resistance of the first stage ($\mathrm{R}_1 = \mathrm{r}_{02}//\mathrm{r}_{04}$), while R_2 is the output resistance of the second stage ($\mathrm{R}_2 = \mathrm{r}_{05}//\mathrm{r}_{0C}$), C_1 is the total capacitance between the first and the second stage, and C_2 the output capacitance.

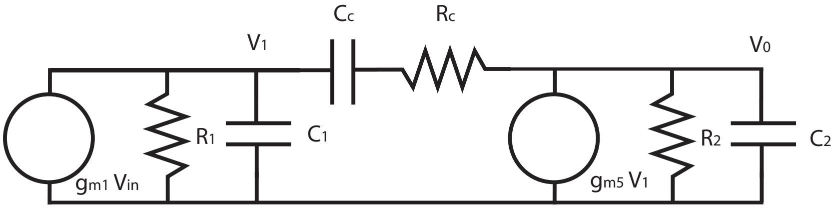

Figure 1.40: Equivalent circuit of the operational amplifier

The transfer function of the circuit is

$$\frac{V_o}{V_{in}} = A_v \frac{[1 + s(R_c - 1/g_{m5})C_c]}{\left(1 + \dfrac{s}{p_1}\right)\left(1 + \dfrac{s}{p_2}\right)} \tag{1.27}$$

where

$$p_1 \simeq \frac{-1}{g_{m5} R_2 R_1 C_C} \tag{1.28}$$

and

$$p_2 \simeq \frac{-g_{m5} C_C}{C_1 C_2 + (C_1 + C_2) C_C} \tag{1.29}$$

This transfer function features also a zero placed at

$$z = \frac{1}{(R_C - 1/g_{m5})C_C} \tag{1.30}$$

If we assume that the pole given by equation (1.28) is the dominant pole, we obtain a gain-bandwidth product given by

$$f_T = \frac{g_{m1}}{2\pi C_C} \tag{1.31}$$

In order to obtain the best transistor dimensions for achieving the desired specifications, we used the g_m/I_D method. The curve g_m/I_D reduces the range of values for the best dimension search. The relation between g_m/I_D and the bias point of the transistors can be explained using the definition of g_m, that is

$$\frac{g_m}{I_D} = \frac{1}{I_D}\frac{\delta I_D}{\delta V_{GS}}\bigg|_{V_{DS}=constant} = \frac{\delta log(I_D)}{\delta V_{GS}}\bigg|_{V_{DS}=constant} \tag{1.32}$$

This relation can be obtained in two ways:

- experimentally;
- analytically (or by means of circuital simulators).

We adopted the second method, even if the results are closely dependent on the reliability of the used transistor models (Fig. 1.41).

The cutoff frequency of the operational amplifiers before the demodulator must be higher than 200 kHz, for obvious reasons. The resulting dimensioning of this family of operational amplifiers is summarized in Table 1.5. Fig. 1.42 shows the Bode diagram of the operational amplifiers dimensioned according to Table 1.5. The operational amplifiers used after the demodulator require low bandwidth and slew-rate, because the information contents of the Fluxgate sensing coils signal has already been down-converted to dc. Therefore, the focus has been put on minimizing the power consumption. The dimensions of the transistors used are

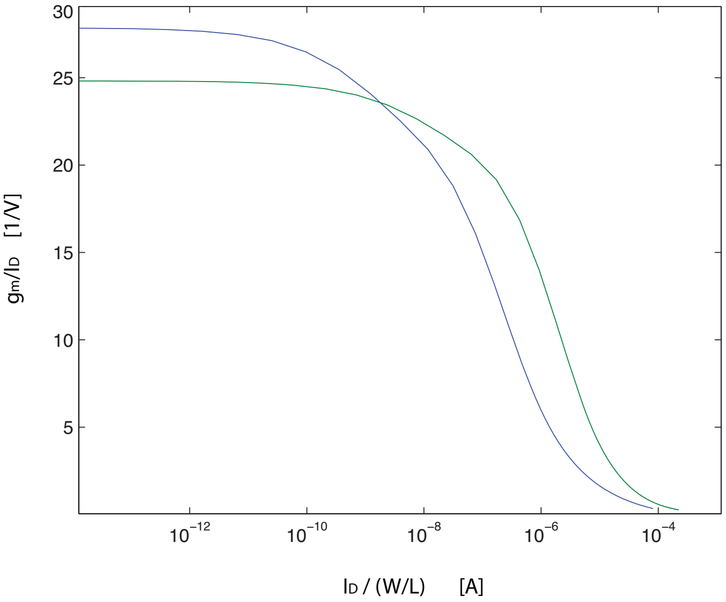

Figure 1.41: Relation between g_m and I_D obtained with the circuit simulator

reported in Table 1.6. The Bode diagram obtained for these amplifiers is shown in Fig. 1.43. Table 1.7 summarizes the features of the the two families of operational amplifiers.

Instrumentation amplifier

The first block in the read-out chain is an instrumentation amplifier. Indeed, the output signal of the Fluxgate sensor is affected by common mode components,

Table 1.5: Transistors dimensions of the operational amplifiers used before the demodulator

M_1	M_2	M_3	M_4	M_5	M_A	M_B	M_C
$\frac{27\ \mu m}{0.4\ \mu m}$	$\frac{27\ \mu m}{0.4\ \mu m}$	$\frac{6\ \mu m}{1\ \mu m}$	$\frac{6\ \mu m}{1\ \mu m}$	$\frac{26\ \mu m}{1\ \mu m}$	$\frac{9\ \mu m}{1\ \mu m}$	$\frac{9\ \mu m}{1\ \mu m}$	$\frac{21\ \mu m}{1\ \mu m}$

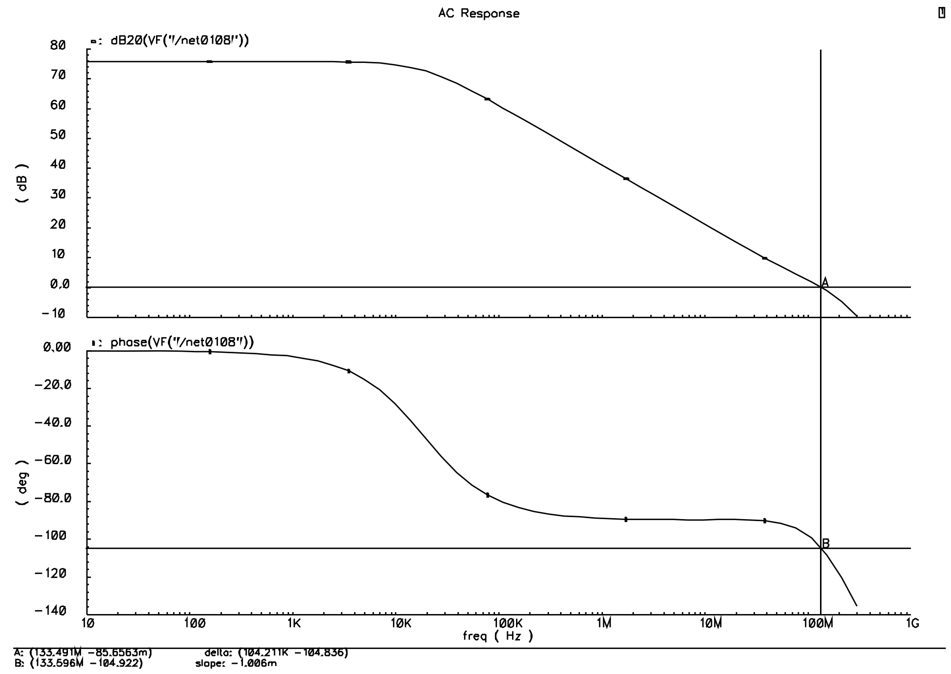

Figure 1.42: Bode diagram of the operational amplifiers used before the demodulator

due to capacitive coupling between the excitation and the sensing coils. This topology of amplifier has been adopted to collect only the useful differential signal. The main feature of an instrumentation amplifier is, in fact, the high common mode rejection. The schematic of the instrumentation amplifier used is shown in Fig. 1.44. The circuit analysis is carried out assuming $A_{1,2,3}$ as ideal. Thanks to the virtual ground V_1 and V_2 are directly applied across R_1. Therefore, the current flowing in R_1 and R_2 is given by

$$i = \frac{(V_1 - V_2)}{R_1} \tag{1.33}$$

The differential voltage signal across the outputs of A_1 and A_2 results

$$V_{01} - V_{02} = \left(1 + \frac{2R_2}{R_1}\right)(V_1 - V_2) \tag{1.34}$$

Table 1.6: Transistors dimensions of the operational amplifiers used after the demodulator

M_1	M_2	M_3	M_4	M_5	M_A	M_B	M_C
$\frac{2\ \mu m}{0.3\ \mu m}$	$\frac{2\ \mu m}{0.35\ \mu m}$	$\frac{2\ \mu m}{1\ \mu m}$	$\frac{2\ \mu m}{1\ \mu m}$	$\frac{3\ \mu m}{1\ \mu m}$	$\frac{4\ \mu m}{0.5\ \mu m}$	$\frac{7\ \mu m}{0.5\ \mu m}$	$\frac{10\ \mu m}{0.5\ \mu m}$

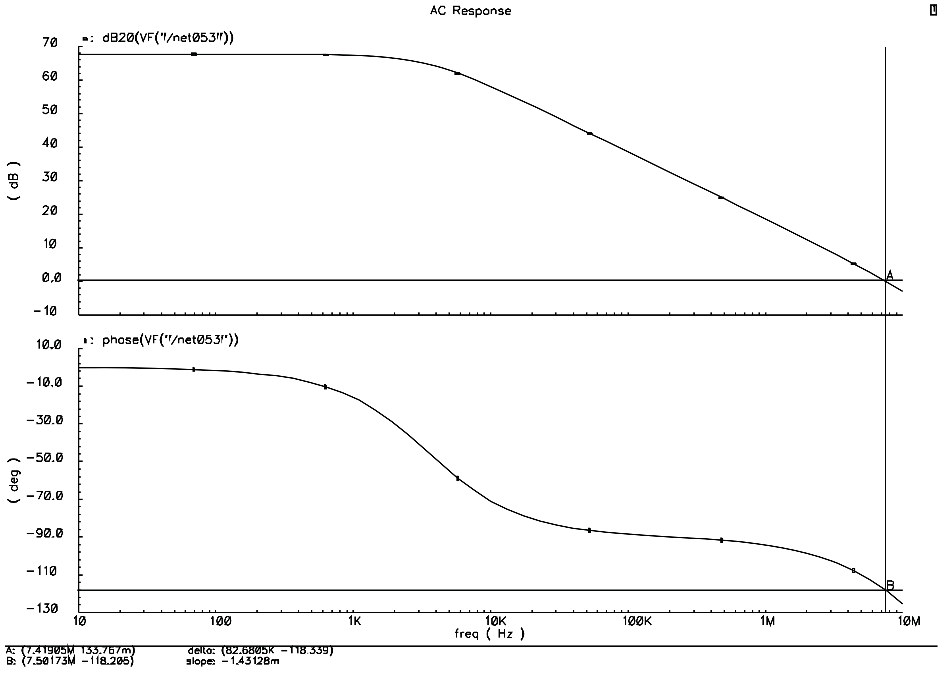

Figure 1.43: Bode diagram of the operational amplifiers used after the demodulator

and the output voltage V_0 is

$$V_0 = -\frac{R_4}{R_3}(V_{01} - V_{02}) \tag{1.35}$$

Fig. 1.45 shows the transient response of the amplifier to an ideal Fluxgate output signal.

Table 1.7: Summary of the operational amplifiers features

Type	Tech	Supply	Gain	BW	Ph M	Slew-rate	P
1	0.35μm	3.3V	75dB	133MHz	76°	55-46V/μs	168μW
2	0.35μm	3.3V	67dB	7MHz	62°	3.1-3.3V/μs	16μW

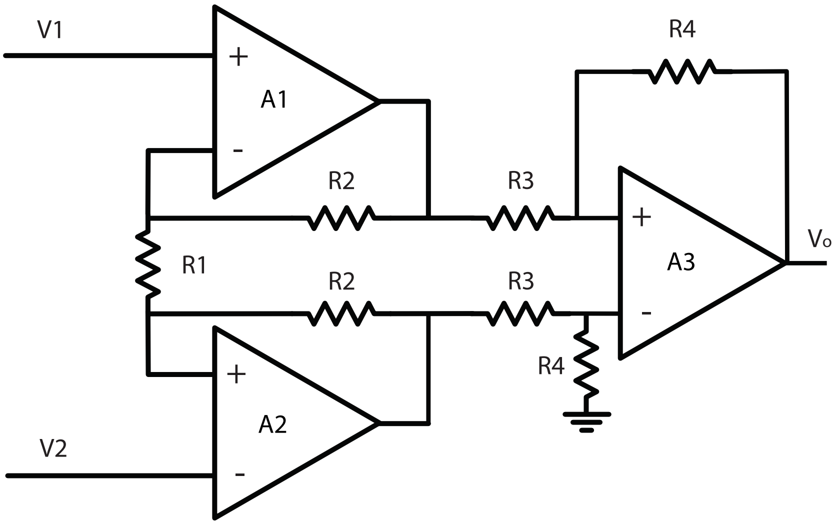

Figure 1.44: Instrumentation amplifier

Coherent quadrature demodulator

In order to retrieve the second harmonic component from the Fluxgate sensor output signal, a coherent quadrature demodulator has been developed. The demodulation is achieved by multiplying the signal with a 200 kHz square wave V$_{LO}$ (200 kHz frequency of the second harmonic of the excitation signal). In particular, assuming a sinusoidal input signal V$_{IN}$, we obtain

$$V_{IN} = X_0 sin(\omega_{IN}t) \tag{1.36}$$

$$V_{LO} = \frac{4}{\pi}\left[sin(\omega_{LO}t) - \frac{1}{3}sin(3\omega_{LO}t) + \frac{1}{5}(5\omega_{LO}t) + ...\right] \tag{1.37}$$

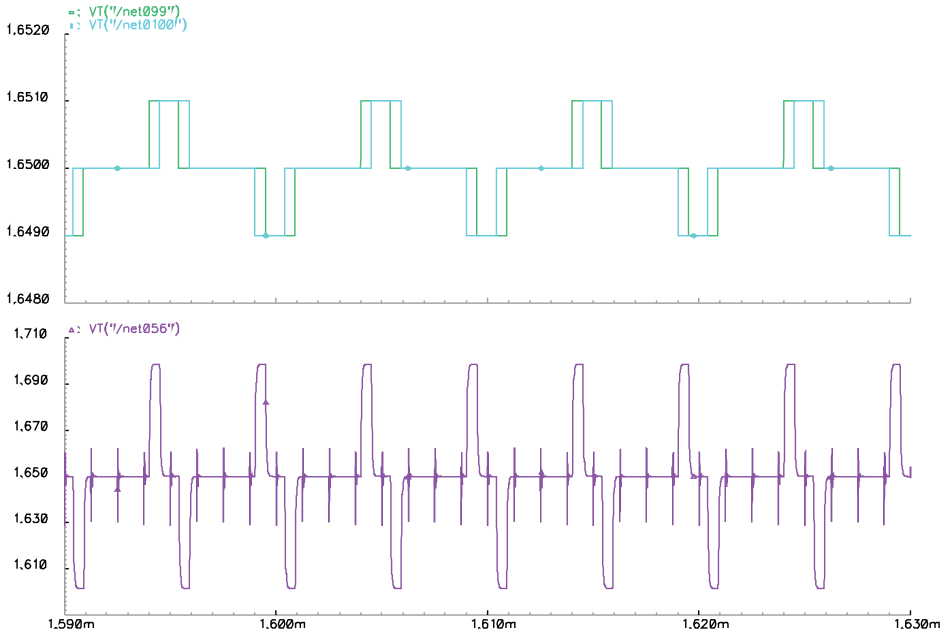

Figure 1.45: Instrumentation amplifier transient response to an ideal Fluxgate output signal

$$V_{IN} \cdot V_{LO} = \frac{2}{\pi}\Big[cos(\omega_{LO} - \omega_{IN})t + cos(\omega_{LO} + \omega_{IN})t + ...\Big] \tag{1.38}$$

The signal $V_{IN} \cdot V_{LO}$ contains several high frequency components that will be eliminated by low-band pass filter, while the component at 200 kHz is down-converted to dc ($\omega_{LO} = \omega_{IN}$), as all the other even harmonic components. This calculation is ideal, since it does not take into account the delays of the devices before the demodulator (i. e. the phase relation between the amplified Fluxgate output signal and the demodulation clock). In order to retrieve the information on the external magnetic field independently of the delays, a quadrature demodulator has been actually implemented.

Sallen-Key filter

The output of the demodulator contains the useful information at *dc*, but it also contains several spurs. Therefore, we introduced a filter for removing any high-frequency unwanted signal components. The filter implements a second order Butterworth transfer function with a cut-off frequency of 550 Hz and a Q factor of 0.707, to guarantee a maximally flat response in the base-band. Fig. 1.46 shows the schematic of the circuit. The transfer function of the proposed circuit is

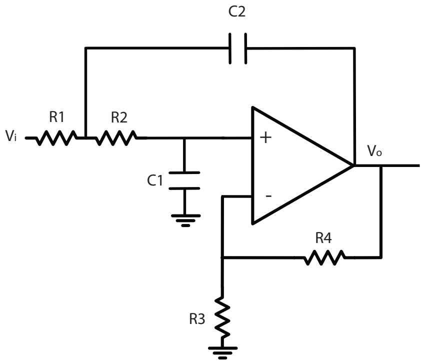

Figure 1.46: Schematic of the Sallen-Key filter

$$A(s) = \frac{\dfrac{K}{R_1R_2C_1C_2}}{s^2 + s\left(\dfrac{1}{R_1C_1} + \dfrac{1}{R_2C_1} + \dfrac{1-K}{R_2C_2}\right) + \dfrac{1}{R_1R_2C_1C_2}} \tag{1.39}$$

The filter gain

$$K = 1 + \frac{R_3}{R_4} \tag{1.40}$$

has been set to 1, and, so, R_4=0 and R_3=+∞. We also imposed

$$C_2 = \frac{\sqrt{2}}{2\pi f R} \tag{1.41}$$

and

$$C_1 = \frac{C_2}{2} \tag{1.42}$$

With f = 500 Hz and R = 7 MΩ, we obtain C_2 = 64 pF and C_1 = 32 pF.

Fig. 1.47 shows the simulated frequency response of the filter. The achieved cutoff frequency is indeed 500 Hz.

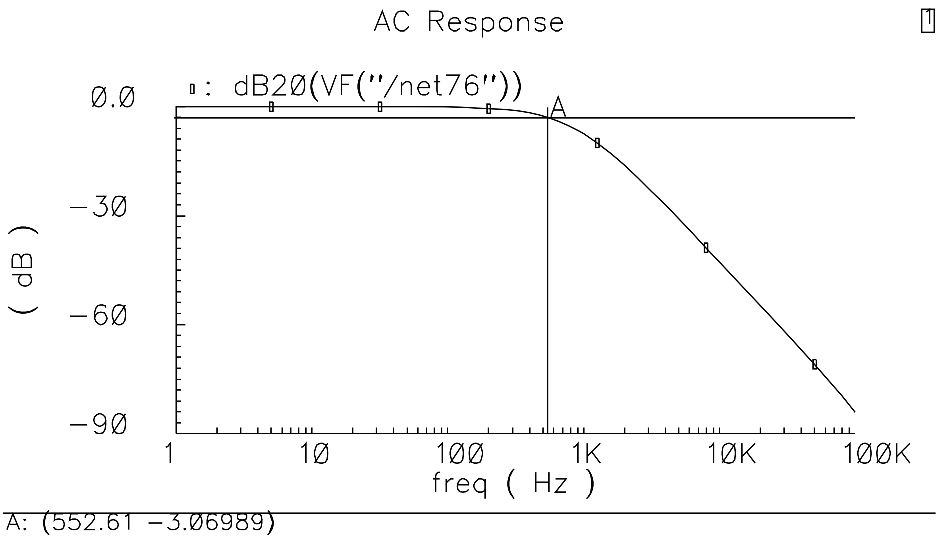

Figure 1.47: Frequency response of the Sallen-Key filter

Programmable gain amplifier

After the Sallen-Key filter, the information on the external magnetic field is represented by the difference V_D between the filter output voltage and the analog ground (1.65 V). In order to obtain a voltage compatible with the input range of the subsequent ADC, considering different sensors with different sensitivities, V_D has to be further amplified. Therefore, we developed a programmable-gain amplifier, whose gain can be selected between 1 and 100 by means of 3 bits (Fig. 1.34). Fig. 1.48 shows the schematic of the circuit, while Fig. 1.49 illustrates the corresponding logic circuit for decoding the 3 programming bits. Table 1.8 summarizes the possible gain values.

1.4.4 Experimental Results

The proposed interface circuit has been integrated in a 0.35-µm CMOS process. Fig. 1.50 shows the micro-photograph of the chip. Fig. 1.51 shows the maximum

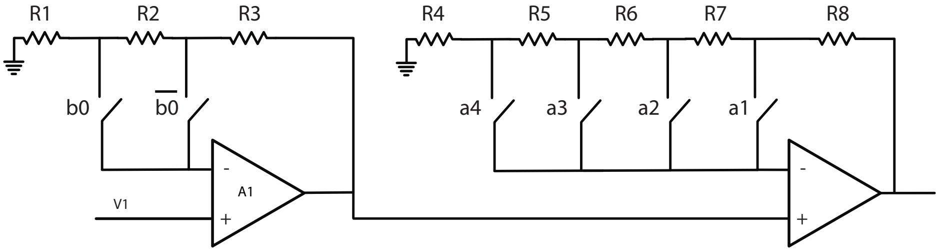

Figure 1.48: Programmable gain amplifier

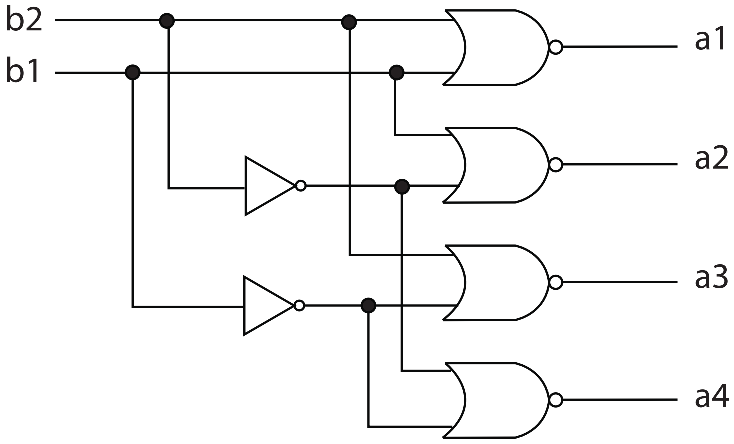

Figure 1.49: Programmable gain amplifier logic circuit scheme

linearity error of the system (Fluxgate sensor and interface circuit) normalized to the full-scale of the applied magnetic field as a function of the full-scale magnetic field itself. In order to obtain this curve, we applied the magnetic field with a couple of Helmholtz coils. The axis of the Helmholtz coils has been oriented perpendicular to the Earth magnetic field, to avoid undesired contributions to the applied magnetic field. The maximum linearity error degrades for large values of the full-scale magnetic field, because of the saturation in the ferromagnetic material of the considered fluxgate sensor, as expected. Fig. 1.52 shows the transfer characteristic of the system for a full-scale magnetic field of 100 µT (±50 µT). Finally, Fig. 1.53 shows the relative linearity error with the same full-scale magnetic

Table 1.8: Possible gain values of the programmable gain amplifier

b0	b1	b2	Gain
0	0	0	1
0	0	1	2
0	1	0	5
0	1	1	10
1	0	0	10
1	0	1	20
1	1	0	50
1	1	1	100

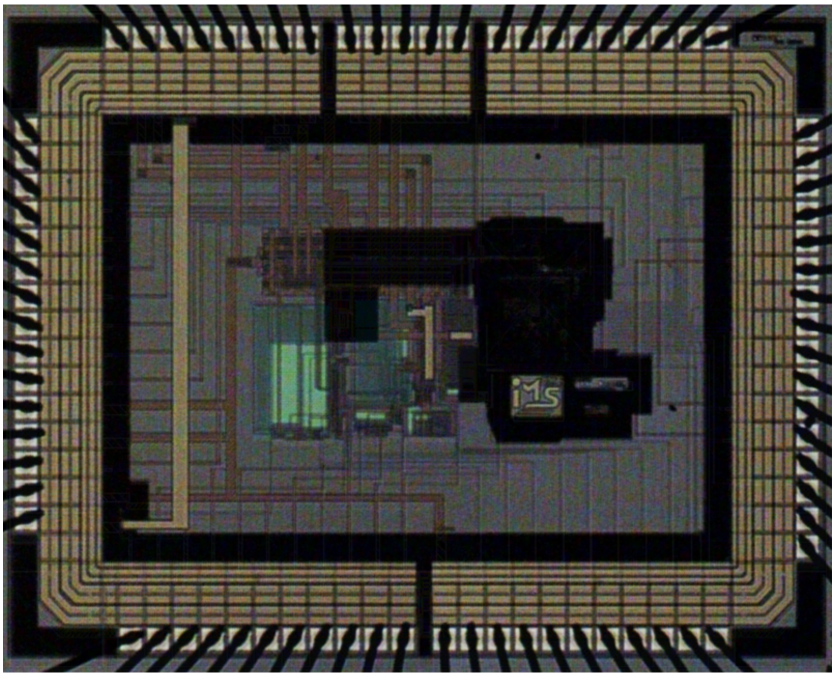

Figure 1.50: Microphotograph of the interface circuit chip

field.

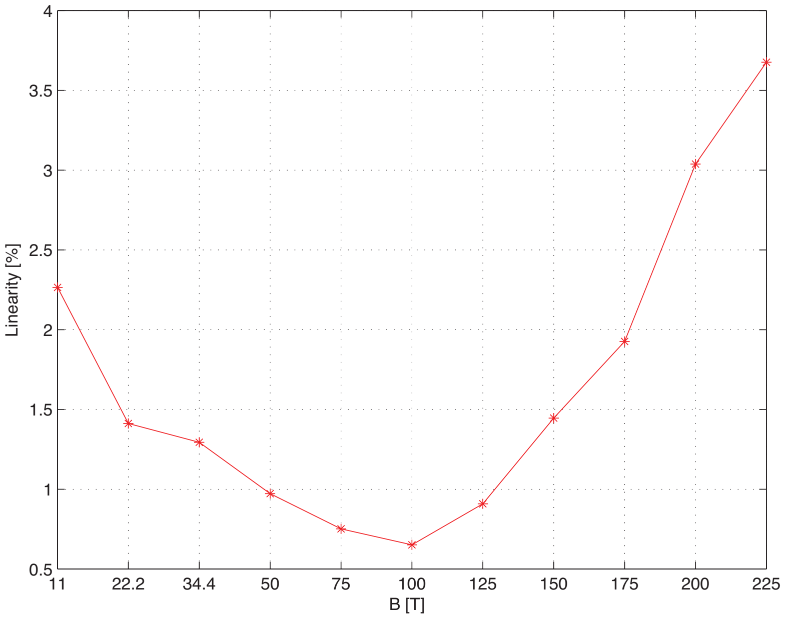

Figure 1.51: Maximum relative linearity error of the system as a function of the full-scale magnetic field

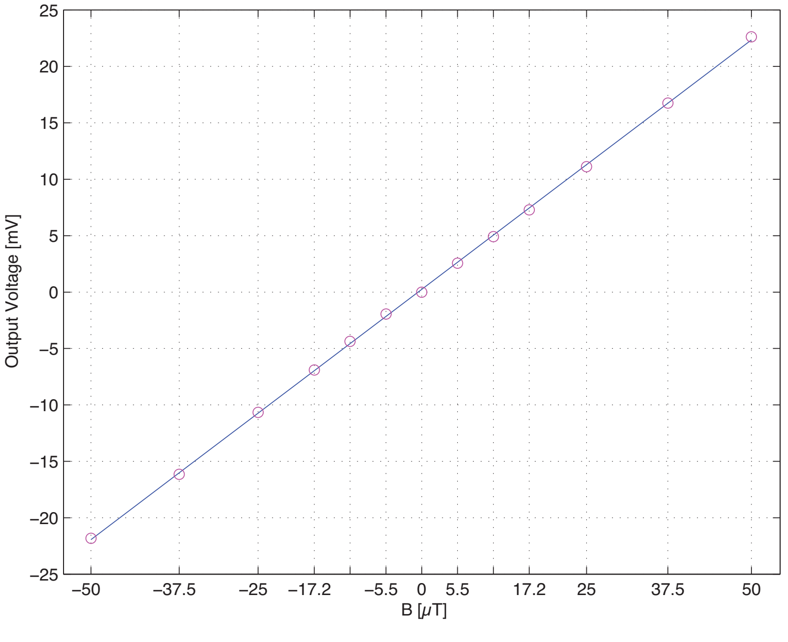

Figure 1.52: Transfer characteristic of the system for a full-scale magnetic field of 100 μT (±50 μT)

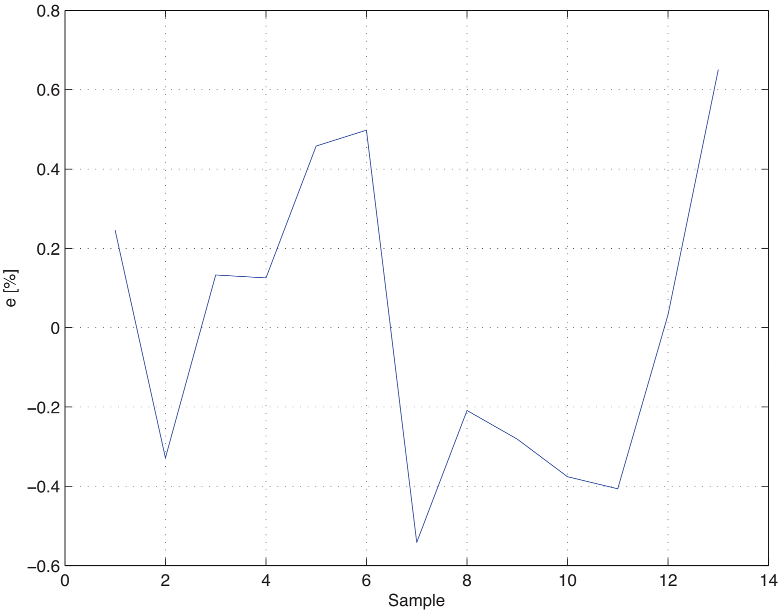

Figure 1.53: Relative linearity error of the system for a full-scale magnetic field of 100 μT (±50 μT)

Chapter 2

Energy Harvesting

In this chapter we present the activity on energy harvesting. In particular, we developed several integrated solutions to retrieve the energy needed to supply a microsystem from the environment, thus avoiding the use of batteries and making the system completely autonomous. The energy source that has been considered is light, and the exploited process to convert it into electrical power is the photoelectric effect of a p-n junction on silicon, commonly used in CMOS fabrication technology.

2.1 Introduction

Modern ultra-low-power integrated circuits have reached such a level of integration and processing efficiency that many applications no longer require traditional batteries. These applications include complex and often power-intensive wireless sensor networks that may involve sampling various sensors and communicating wirelessly. By harvesting minuscule amounts of wasted energy from the environment, such systems are enabled with near infinite up-time without a battery as its primary power source. Not only does energy harvesting enhance current

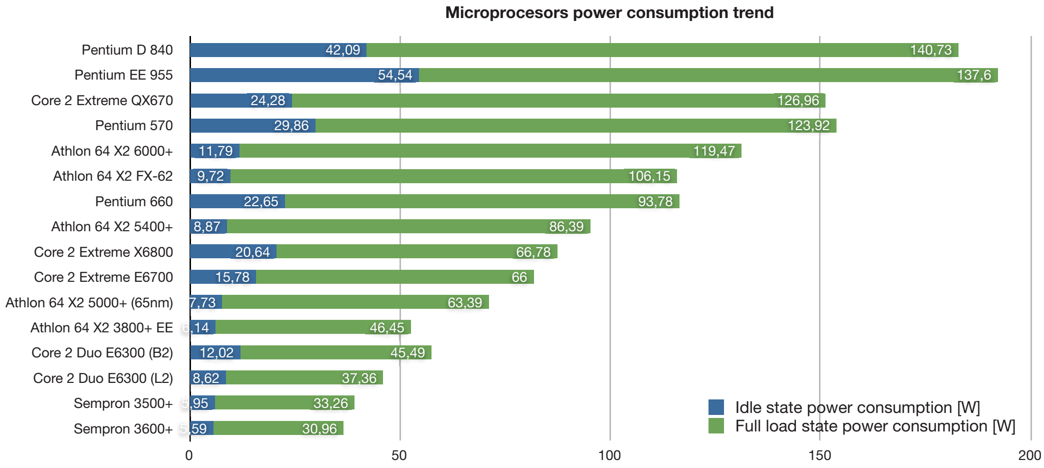

Figure 2.1: Trend of power dissipation in microprocessors design field

applications by eliminating their dependency on the battery, but it also enables entirely new applications that were not feasible given the finite lifetime and size of batteries. Similar to Moore's Law, which defines the trend of digital technology to double in transistor count every two years, an inverse trend occurs for power consumption. Roughly every 18 months, the power dissipation of digital systems is cut in half. Despite the technology scaling, electrochemical batteries [18] are characterized by a slow growth in terms of energy density, and represent an add on of weight and volume, limiting the lifetime of the devices. Advancements in power efficiency already had very significant results for small, ultra-low-power microcontrollers (MCUs) specifically designed for battery-powered applications and have resulted in designs where battery life has exceeded 10 years. For typical ultra-low-power MCUs, it is common for standby current to be less than 1 µA, and active current consumption in the 200 µA/MIPS range. Since the clock rate of these MCUs is typically in the order of 25 MHz or less, the peak current consumption is always relatively small and can be powered with simple power supplies. Power consumption of a given application is rarely characterized by a single MCU's current draw. Analog conversion circuitry, power regulation, and communication devices each play a part in the system and consume power even when they are not active. By integrating the functionality of each of the devices into a single chip using a single low-power fabrication process, it is not only possible to significantly reduce the leakage current of the overall system, but by giving a single MCU control to disable peripherals that are not in use, power consumption can be reduced even further. A single, highly integrated device will typically consume less power than separate discrete solutions; a single device also simplifies the design and reduces the cost and area required for a given function.

Traditional batteries, such as lithium-ion cells, have been the default source for power in portable electronics for decades; however, traditional batteries place hard restrictions on product usability, lifetime, and cost of ownership. While processing power roughly doubles ever two years, battery technology advances at a much more sluggish pace. Historically, battery capacity has doubled every 10 years. In addition to the very slow growth in their energy capacity, traditional batteries have a limit to the total practical energy density they can provide. Present-day lithium-ion batteries, which are popular due to their high energy-to-weight ratio, have an energy density of 150 to 200 Wh/kg. Research has shown that it is possible to increase their energy density by tenfold within a few years; however, even if this is achieved, we must still consider practical safety concerns. Given improper use, batteries with extremely high energy densities can become dangerous, explosive devices. For most battery-operated devices, the cost associated with owning and operating the device is rarely limited to the initial cost of manufacturing it. In the long term, replacing the battery can have a significant impact on the overall cost of ownership. This is especially critical in applications where battery replacement is impractical or has high labor costs associated with maintenance. Take for example water meters that must be buried underground. Accessing the water meter would require digging it up, which in colder climates might be one meter or deeper underground. Thanks to this unavoidable inaccessibility, the replacement cost of the battery could be in the $100 to $200 range per water meter. Miniaturization of products has been an ongoing trend in most application spaces, but the driving force has come from consumer electronics and medical applications. For consumer products, the demand for smaller and sleeker devices has driven innovation for more highly integrated electronics given the finite amount of space that products are expect to take up. While integration at the IC level has kept up with consumer demand, the power source is not benefiting from miniaturization. The space allowed for batteries is shrinking, the lifetime for which they are expected to operate is longer, and the amount of power they are expected to provide has also increased. The requirements for batteries in modern electronics have far exceeded what can be delivered. Despite the challenges with traditional batteries, it is possible to maintain functionality with today rechargeable batteries, or we may even forgo the battery altogether if we couple an ultra-low-power embedded processor with a power supply that harvests energy from its environment. Alternative power sources could extend the lifetime of low-power systems, such as mobile and sensor nodes[19], reducing the volume-dependency and the weight. Therefore, harvesting systems [20] [21] [22] are becoming the new challenge in both research and commercial communities. In most cases, in fact, the final device is located in environments with many energy sources, such as lights, vibrations or thermal gradients. In this case energy scavenging represents an optimum option to increase the performance of the device.

2.2 Micro Energy Harvesting

In principle, energy harvesting has been around for thousands of years. The first waterwheels have been dated back to as far as the fourth century B.C. The waterwheel effectively harvested the energy from flowing water and transferred it to mechanical energy. Similarly, present-day wind farms or solar arrays all use the same principle of operation and usually provide power back to the main grid. These large-scale applications can be referred to as macro energy harvesting. On the other hand, micro energy harvesting, which we will be focusing on, is the principle that enables small, autonomous devices to capture energy from the environment and store it. While micro and macro energy harvesting may be similar in principle, their scope and applications are radically different. The portion of the system that harvests energy consists of two main parts:

- the component that converts the ambient energy from the environment;
- a means of storing the energy for later use by the application.

Although the rest of the system can be defined in an infinite number of ways and is dependent on the task at hand, energy-harvesting systems typically contain similar components given that they are ideal for sensor network applications. An ultra-low-power MCU will be the heart of the system and is responsible for the majority of the processing, sensing, and communication. The MCU will interface to any number of sensors to collect data from its environment and will usually transfer or receive data via a wireless transceiver. Since energy harvesting systems are completely untethered, they each act as autonomous systems. The sources of energy to harvest are similarly numerous, and more esoteric systems continue to be introduced. However, the most common sources for ambient energy are light, thermal, radio frequency (RF), and vibration. The characteristics of typical energy harvesters are summarized in Table 2.1. Each has unique advantages and disadvantages, and the specific harvesting technology is dependent on the application and the use case. Clearly, a device outfitted with a solar panel would not benefit if it sits in a dark cave all day. The key to an energy-harvesting system is to take en-

Table 2.1: Characteristics of typical energy harvesters

Energy Source	**Characteristics**	**Efficiency**	**Harvester power**
Light	Outdoor Indoor	10-25%	100 mW/cm^2 100 μW/cm^2
Thermal	Human Industrial	~ 0.1% ~ 3%	60 μW/cm^2 10 mW/cm^2
Vibration	~Hz-Human ~Hz-Machines	25-50%	4 μW/cm^2 800 μW/cm^2
Radio Frequency (RF)	GSM 900 MHz WiFi 2.4 GHz	~50%	0.1 μW/cm^2 0.001 μW/cm^2

ergy that is readily and predictably available and collect what would otherwise be wasted power. The element used to store the power would act as an energy buffer for the rest of the application. The size and technical properties of the buffer is dependent on the application. If the application requires long periods of time to elapse between when it accesses an available energy source, a very large buffer is required; however, if the application is constantly around the energy source and rarely needs to be active (low duty-cycle applications), a very small buffer would be sufficient. In order to accommodate the widest possible cases, the ideal energy buffer would have the following properties:

- negligible leakage (self discharge);
- unlimited capacity;
- negligible volume;
- no need for energy conversion;
- efficient energy acceptance and delivery.

Table 2.2: Characteristics of typical energy storage options

	Li-Ion battery	**Thin-film battery**	**Super cap**
Recharge cycles	Hundreds	Thousands	Millions
Self-discharge	Moderate	Negligible	High
Charge time	Hours	Minutes	Sec-minutes
Physical size	Large	Small	Medium
Capacity	0.3-2500 mAHr	12-1000 µAHr	10-100 µAHr
Environmental impact	High	Minimal	Minimal

Unfortunately, the ideal storage element does not exist, but several options are available including rechargeable batteries (such as alkaline, nickel-cadmium, and lithium-ion), super capacitors, or thin-film batteries. While rechargeable batteries in various chemistries and super capacitors are well-established technologies that continue to improve, thin-film batteries have only recently begun to proliferate in the market and serve as a good alternative to super capacitors. Key parameters of each type of storage technology are listed in Table 2.2.

2.3 Photovoltaic Energy Harvesting Process

Light could be considered the most copious energy source in many indoor environment, even if outdoor application seldom can be apart from using photovoltaic scavengers, that can reach conversion efficiencies from 20% in standard monocrystalline planar technology, till almost 50% [23][24]in multi-material planar wafers, with an availability of $1000W/m^2$ of the sun. Moreover the photo-electric phenomena [25] of doped silicon allows to retrieve the higher quantity of power respect other types of harvesters. In this paragraph we discuss the basic principles of solar cells. The role of a solar cell into an energy harvesting microsystem is to convert the optical incident power into electrical power. In solar cells (and photodetectors) the optical energy is absorbed in a semiconductor and generates excess of electron-hole pairs, producing photocurrents. The output terminal of a solar cell is connected to a resistive load, so that the input optical power is converted to electrical power. The simple p-n junction solar cell is considered in the energy harvester integrated solution that will be described in this chapter. The main characterization of a solar cell is made in terms of short circuit current, open circuit voltage, maximum power and conversion efficiency.

2.3.1 Optical absorption

According to the wave-particle duality principle, the light wave can be treated as particles, which are referred to as photons. The energy related to a photon is $E = h\nu$ where h is Plank's constant and ν is the frequency. We can also relate wavelength and energy by

$$\lambda = \frac{c}{\nu} = \frac{hc}{E} = \frac{1.24}{E}\ \mu\mathrm{m} \tag{2.1}$$

where E is the photon energy in eV and c is the speed of light.

There are several possible photon-semiconductor interaction mechanisms. For example, photons can interact with the semiconductor lattice whereby the photon energy is converted into heat. Photons can also interact with the semiconductor impurity atoms, either donors or acceptors, or they can interact with defects into the semiconductor. However those kinds of interaction for an energy harvesting application are undesired, and, so, are considered as source of efficiency loss because any optical power related to those phenomena cannot be converted into electrical power. The basic photon interaction process of greater interest is the interaction with valence electrons. When a photon collides with a valence electron, enough energy may be imparted to elevate the electron into conduction band. Such a process generates electron-hole pairs and creates excess carrier concentrations.

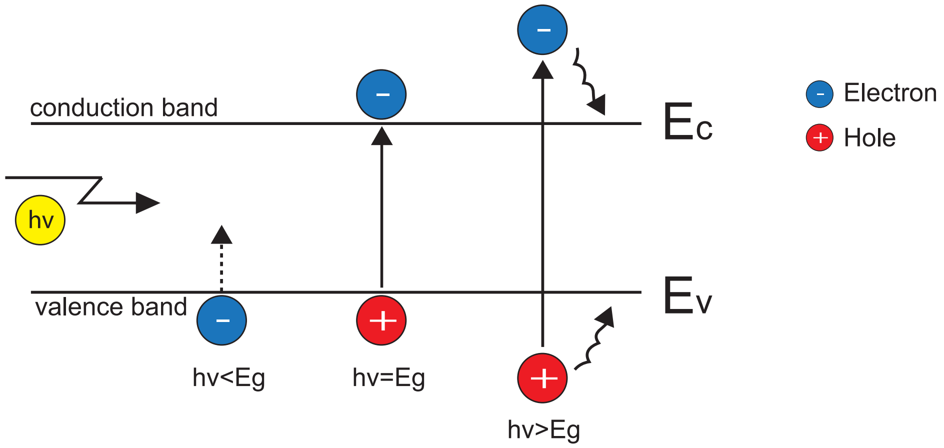

Figure 2.2: Optically generated electron-hole pair formation in a semiconductor

Photon absorption coefficient

When a semiconductor is illuminated, the photons can be absorbed or may propagate trough the semiconductor, depending on the photon energy and on the band-gap energy E$_g$. In particular, if the photon energy E is less than E$_g$ the photons are not readily absorbed. In this case the material is completely transparent. If $E = h\nu \geqslant E_g$, the photon can interact with a valence electron, providing enough energy to it to elevate to the conduction band. The valence band contains many electrons and the conduction band contains many empty states, so the probability of this interaction is high when $h\nu > E_g$. This interaction creates an electron in the conduction band, and an hole in the valence band (electron-hole pair). The basic absorption process for different values of $h\nu$ are shown in Fig. 2.2. When $h\nu > E_g$ and an electron-hole pair is created, the excess energy can be transfered to the electron or hole as kinetic energy, which will be dissipated as heat in the semiconductor. In other words, the efficiency loss in the photoelectric process is intrinsic in the process itself.

The intensity of the photon flux is denoted by I$_\nu$(x) and is expressed in terms of energy/cm^2-sec. If we assume that an incident photon flux at the position x emerges at the position $x + dx$, it is possible to evaluate the absorbed energy per unit time at the distance dx. In particular it is given by

$$\alpha I_\nu(x)dx \tag{2.2}$$

where α is the absorption coefficient. The absorption coefficient is the relative number of photons absorbed per unit distance, given in units of cm^{-1}. In particular:

$$I_\nu(x + dx) - I_\nu(x) = \frac{dI_\nu(x)}{dx} \cdot dx = -\alpha I_\nu(x)dx \tag{2.3}$$

or

$$\frac{dI_\nu(x)}{dx} = -\alpha I_\nu(x) \tag{2.4}$$

If the initial condition is given as $I_\nu(0) = I_{\nu 0}$, then the solution to the differential equation (2.4) is

$$I_\nu(x) = I_{\nu 0}e^{-\alpha x} \tag{2.5}$$

The intensity of the photon flux decreases exponentially with the distance though the semiconductor material. The photon intensity as a function of x for two general values of absorption coefficient is shown in Fig. 2.3. If the absorption coefficient is large, the photons are absorbed over a relatively short distance.

The absorption coefficient in the semiconductor is a very strong function of photon energy and band-gap energy. The absorption coefficient increases very rapidly for $h\nu > E_g$, or for $\lambda < 1.24/E_g$.

2.3.2 Solar cells

A solar cell is a p-n junction device with no voltage directly applied across the junction. The solar cell converts photon power into electrical power and delivers this power to a load. These devices have long been used for the power supply of satellites and space vehicles, and also as the power supply to some calculators.

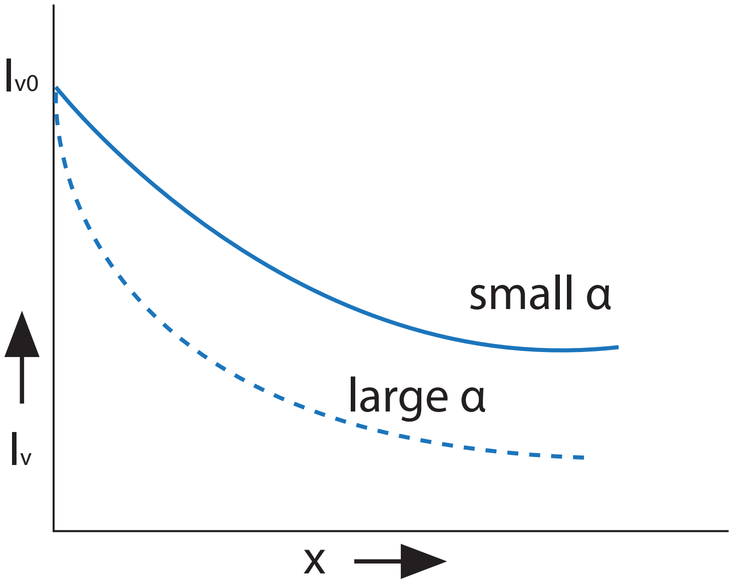

Figure 2.3: Photon intensity versus distance for two absorption coefficients

In Fig. 2.4 a p-n junction solar cell with a resistive load is shown. Even with zero bias applied to the junction, an electric field exists in the space charge region as shown in the figure. Incident photon illumination can create electron-hole pairs in the space charge region that will be swept out producing the photo-current I$_L$ in the reverse-bias direction as shown.

The photo-current I$_L$ produces a voltage drop across the resistive load which forward biases the p-n junction. The forward-bias voltage produces a forward-bias current I$_F$ as indicated in the figure. The net p-n junction current, in the reverse-bias direction, is

$$I = I_L - I_F = I_L - I_S\left[\mathrm{e}^{\left(\frac{eV}{kT}\right)} - 1\right] \tag{2.6}$$

where the ideal diode equation has been used. As the diode becomes forward biased, the magnitude of the electric field in the space charge region decreases, but does not go to zero or change direction. The photo-current is always in the

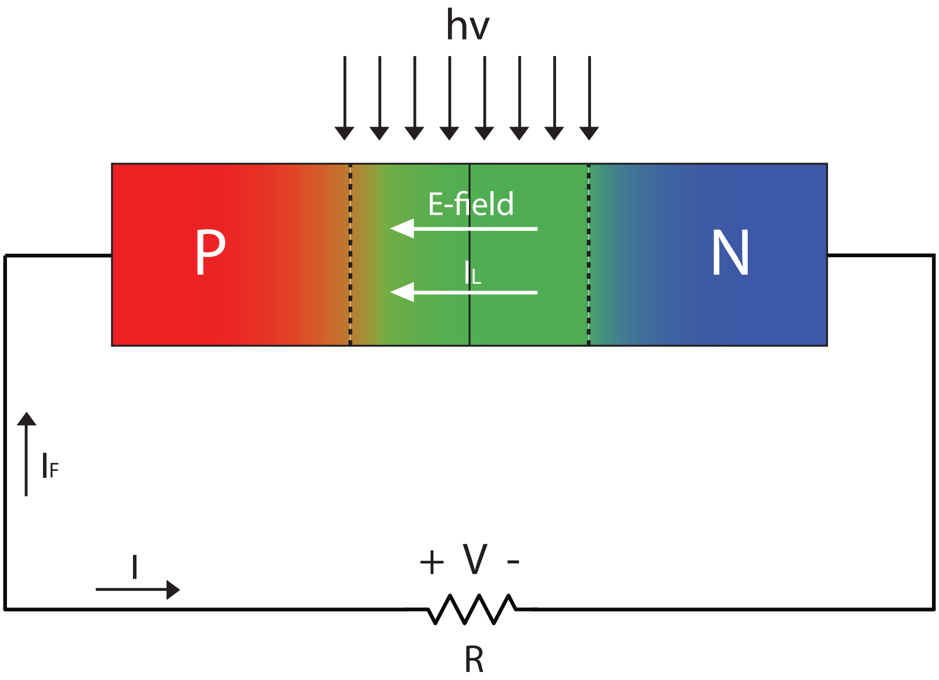

Figure 2.4: A p-n junction solar cell with resistive load

reverse-bias direction and the net solar cell current is also always in the reverse-bias direction.

There are two cases of interest. The short circuit condition occurs when R = 0 so that V = 0. The current in this case is referred to as the short-circuit current, or

$$I = I_{SC} = I_L \tag{2.7}$$

The second limiting case is the open-circuit condition and occurs when R → ∞. The net current is zero and the voltage produced is the *open-circuit voltage*. The photocurrent is just balanced by the forward-biased junction current so we have

$$I = 0 = I_L - I_S\left[\mathrm{e}^{\left(\frac{eV_{OC}}{kT}\right)} - 1\right] \tag{2.8}$$

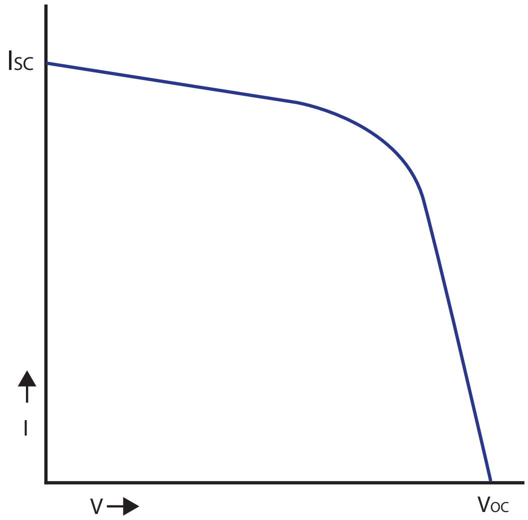

Figure 2.5: I-V characteristics of a p-n junction solar cell

thus the open-circuit voltage V$_{OC}$ is

$$V_{OC} = V_t \ln\left(1 + \frac{I_L}{I_S}\right) \tag{2.9}$$

A plot of the diode current I as a function of the diode voltage V from equation (2.6) is shown in Fig. 2.5. It is possible to note the short-circuit current and the open-circuit voltage points on the curve. The power delivered to the resistive load is

$$P = I \cdot V = I_L \cdot V - I_S\left[\mathrm{e}^{\left(\frac{eV_{OC}}{kT}\right)} - 1\right] \cdot V \tag{2.10}$$

It is possible to find the current and the voltage which will deliver the maximum power to the load by setting the derivative of P equal to zero, or dP/dV = 0. Using equation (2.10), we find

$$\frac{dP}{dV} = 0 = I_L - I_S\left[\mathrm{e}^{\left(\frac{eV_{OC}}{kT}\right)} - 1\right] - I_S V_m\left(\frac{e}{kT}\right)\mathrm{e}^{\left(\frac{eV_m}{kT}\right)} \tag{2.11}$$

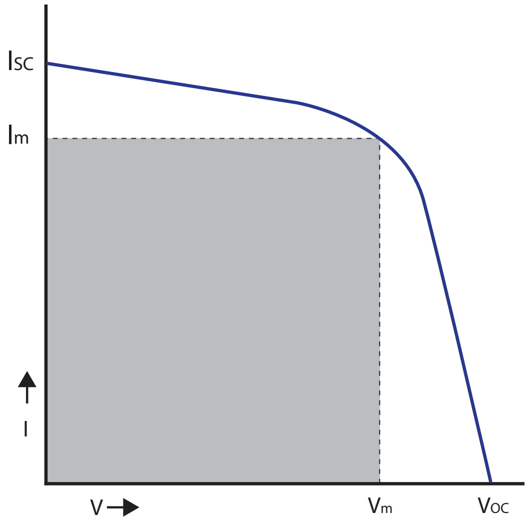

Figure 2.6: Maximum power rectangle of the solar cell I-V characteristics

where V_m is the voltage which produces the maximum power. We can now rewrite equation (2.11) in the form

$$\left(1+\frac{V_m}{V_t}\right)e^{\left(\frac{eV_m}{kT}\right)}=1+\frac{I_L}{I_S} \tag{2.12}$$

The value of V_m may be determined by trial and error. Fig. 2.6 shows the maximum power rectangle where I_m is the current when $V = V_m$.

2.4 Integrated Micro-Solar Cell Structures for Harvesting Supplied Microsystems in 0.35-μm CMOS Technology

In this section we present a solar harvester test chip, realized to characterize several integrated solar cell structures, gathering the information required to design a complete power management system for handling the harvested energy. In particular, we realized photodiodes with three different geometries of the p-diffusion, and three different dimensions of the n-well. The chip is realized in a 0.35-μm

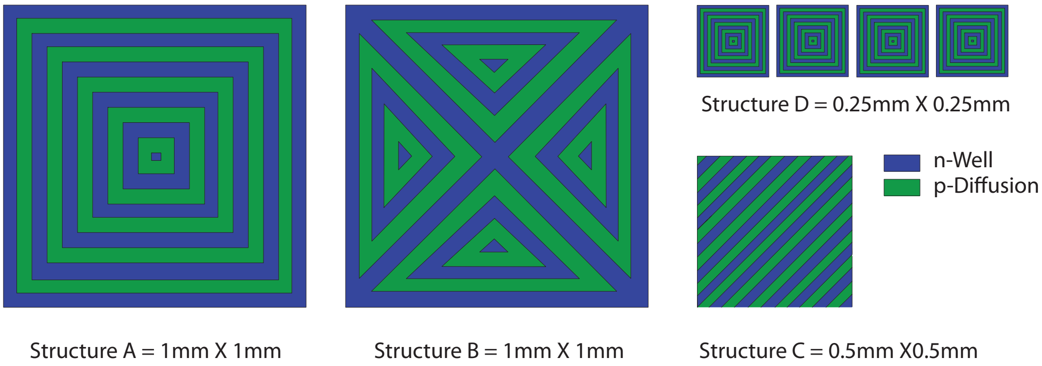

Figure 2.7: Geometries and dimensions of the realized micro solar cells

CMOS technology, and the diodes feature different active area density, depending on the geometry of the p-diffusions. In order to evaluate the harvesting performance of the solar cells in real applications, we developed an equivalent circuit of the devices, based on the experimental data and we used it to design a power management system specific for discrete-time applications.

2.4.1 Solar cells characterization

In order to create a circuit model to simulate the scavenger system, we realized a test chip in 0.35-µm CMOS technology with several p-n junction in an open package, thus allowing illumination of the chip. Fig. 2.7 shows the different p-diffusion geometries realized to maximize the active area density, and the relative dimensions on-chip. The presented work is focused on the characterization of the solar structures in terms of geometry dependent efficiency and relative performance improvement. Each solar cell can be modeled as a couple of p-n junctions. Fig. 2.8 shows the cross-section and the equivalent circuit. The upper diode (between p-diffusion and n-well) is the desired harvester, while the deeper one is a parasitic diode, whose junction is composed by the n-well and the low doped p-substrate. In the used technology it is not possible to realize a floating diode

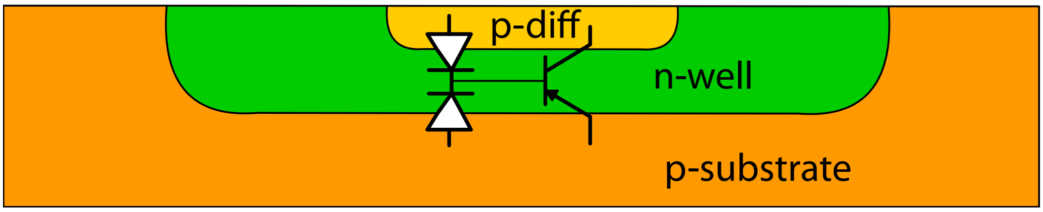

Figure 2.8: Cross-section and equivalent circuit of realized solar structures

Table 2.3: Dimensions of the realized solar cell structures

Type	Harvester Area [mm^2]	Harvester Perimeter [mm]	Parasitic Area [mm^2]	Parasitic Perimeter [mm]
A	24.39	642.5	1	4
B	0.29	827.8	2	5.6
C	0.072	207.4	0.5	2.9
D	0.18	47.1	0.06	1

without parasitic diode and the parasitic diode cannot be shielded from the incident light. Therefore, the parasitic diode provides photo-generated power as the actual harvester. Tab. 2.3 summarizes the dimensions and the equivalent active area for each structure. All the photovoltaic structures implemented on the test chip can be used for several purposes:

- as high efficiency micro solar cell;
- as harvester for integrated microsystems integrated on the same chip;
- as photodiode based light sensor.

The characterization of this test chip is focused on the first two applications, on the basis of geometry dependent efficiency. In order to characterize the micro solar cell as a stand alone device, it is useful to connect the substrate to the p-diffusion, thus connecting the two diodes in parallel. The current contributions of

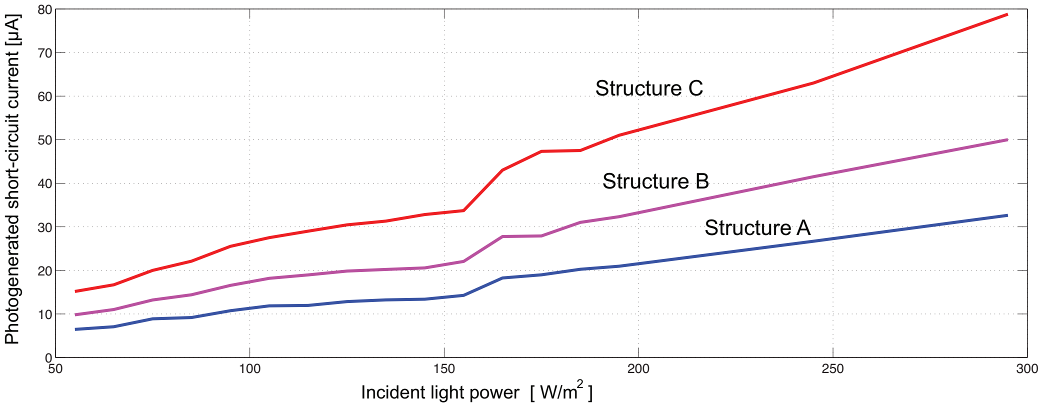

Figure 2.9: Short-circuit photo-generated current as a function of the incident light power

both diodes are, therefore, added. Fig. 2.9 shows the result of the measurement of the photo-generated short-circuit current as a function of the incident light power for the realized structures. All curves have been normalized to the area of structure C. The most efficient structure is structure C. The output power of this structure, obtained with an illumination of 300 W/m^2, is shown in Fig. 2.11. The conversion efficiency of the integrated micro solar cells, depending on the p-diffusion geometry, is reported in Tab. 2.4. Device C features an efficiency as large as 17%. In order to avoid contributions form other devices on the chip, both terminals of all the diodes not being tested are short-circuited to the substrate. The largest photo-generated current contribution is given by the parasitic diode, since its junction is deeper and the substrate is less doped than the p-diffusion, thus leading to a higher efficiency than in the corresponding harvester.

Fig. 2.10 shows the contribution of the harvesters with floating substrate diode, without any normalization on the area, thus emphasizing how the geometry of structure C, that is 75% smaller than the others, achieves optimal performance in terms of photoelectric-conversion efficiency. As expected, geometry C, featuring the largest relative active area density, is the most efficient diode structure.

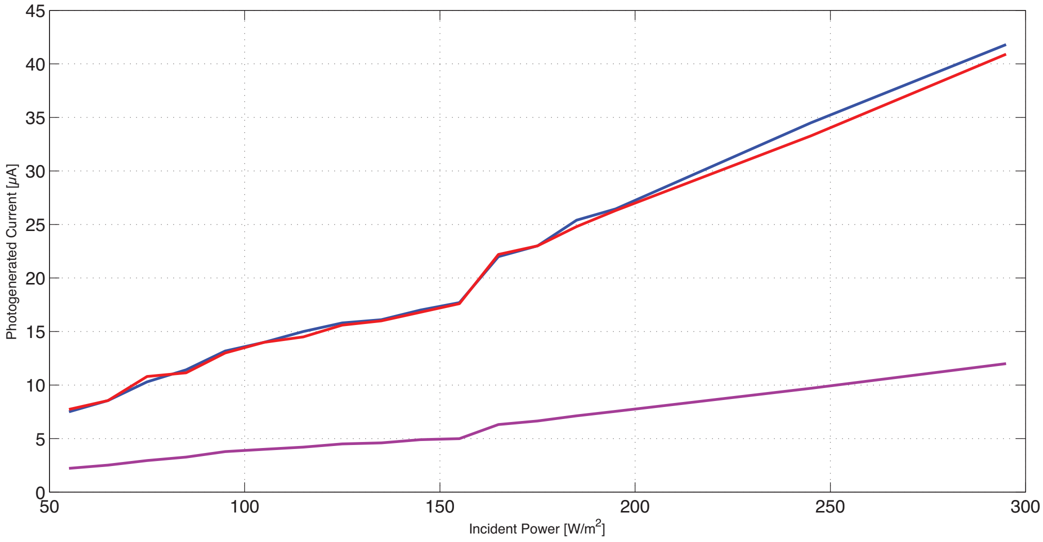

Figure 2.10: Short-circuit photo-generated current as a function of the incident light power with floating parasitic diode

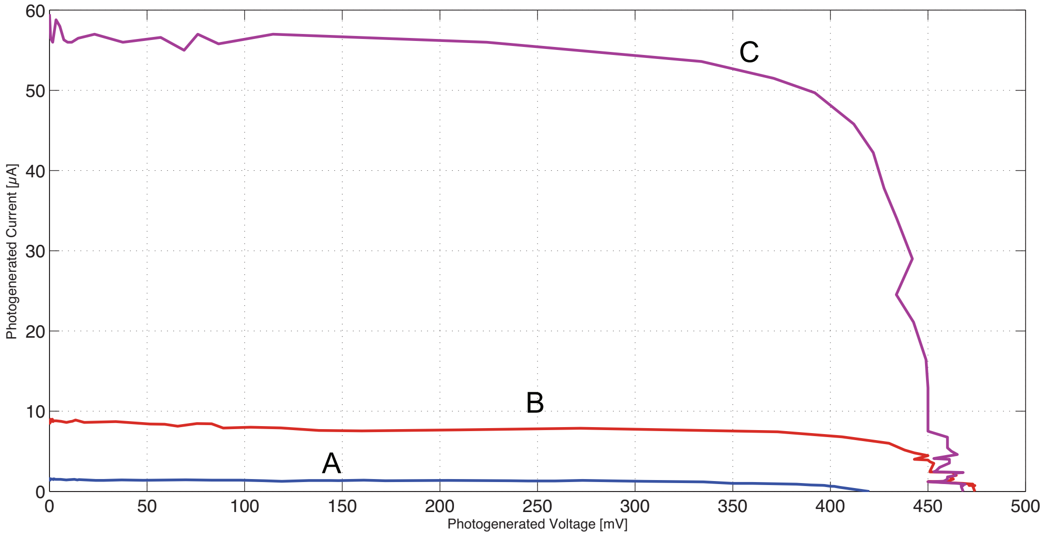

Figure 2.11: Power curves of structure C: (Curve A) harvester contribution with short-circuited parasitic diode, (Curve B) harvester contribution with floating parasitic diode and (Curve C) sum of both contributions

Table 2.4: Conversion efficiency of the solar cell structures

Type	Harvester diode with floating substrate diode	Harvester diode with short-circuited substrate diode	Parasitic diode with floating harvester diode	Harvester and substrate diodes in parallel
A	2.91%	0.44%	9.45%	9.45%
B	3.02%	0.44%	15.12%	15.12%
C	2.91%	1.04%	17.64%	17.01%
D	2.26%	0.56%	11.9%	12.6%

In order to use the diode structures as harvesters to supply an integrated microsystem, realized on the same chip, it is necessary to hold the p-substrate to the lowest voltage value. Therefore, the parasitic diode must be short-circuited (i. e. the substrate must be connected to the n-well and not to the p-diffusion). The resulting structure is not just equivalent to a couple of diodes, but it has to be modeled with a PNP transistor. This is due to the interaction of the currents of the two junctions (transistor effect). In particular, when the junction between p-substrate and n-well is short-circuited, it contributes negatively to the current of the harvester diode. This causes a loss of efficiency, reducing the photo-generated current. For example, with device C, for 300 W/m^2 the current is reduced from 10 μA, obtained when the substrate is floating, to 2.5 μA. To validate the PNP transistor model, we extracted the Ebers-Moll parameters in the absence of light. When the substrate diode is short-circuited, it is necessary to consider the transistor effects also in light irradiation condition.

In view of the obtained results, with the proposed micro solar cells, it is possible to actually design an integrated microsystem with a significant power budget, considering that the incident power in an usual spring day is, at least, 600 W/m^2.

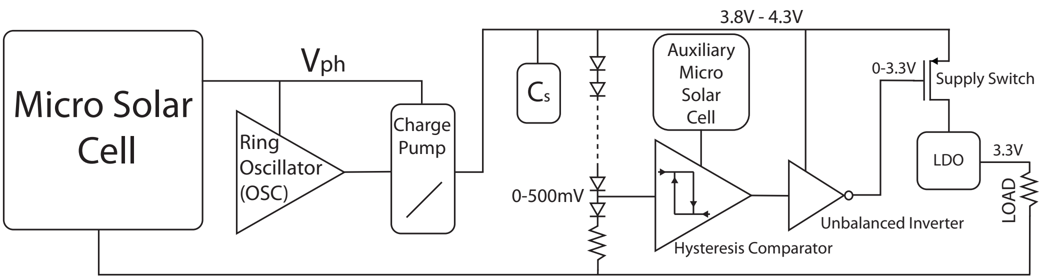

Figure 2.12: Block diagram of the proposed system

2.4.2 Power management system chip

Since a solar energy scavenger is intrinsically a discrete-time power source, which varies with the environmental conditions, photovoltaic systems need an energy storage device and a power management system [26]. Fortunately, many applications, such as sensor network nodes [27, 28, 29, 30] or, in general wireless embedded systems [31, 32] that operate in discrete-time regime, consume power only during short time-slots [33]. In the system that is being presented, an integrated miniaturized solar cell is used as energy source and a power management system has been developed [32], to handle the collected energy. The block diagram of the system is shown in Fig. 2.12, where a generic sensor system has been adopted as load [34]. The circuit elevates with a charge pump the voltage produced by the miniaturized solar cell and charges an external capacitor, in order to supply with 3.3 V through a linear voltage regulator (LDO) the load for a given time-slot, in asynchronous discrete-time regime. The time-slots dedicated to energy accumulation and system operation are established automatically by the system. With this solution it is possible, by choosing the value of the capacitance, to trade the amount of power available for the load with the time required to accumulate it, thus allowing to supply the load for the required time-slot with the required current with a given duty-cycle. The proposed power management circuit consists of an hysteresis comparator and an unbalanced inverter, that controls a switch to connect the load to the storage capacitance. The comparator monitors the charge voltage on the storage capacitor. When the stored charge is sufficient to reach a voltage equal to 4.3 V the comparator provides a signal that, by means of the unbalanced inverter, connects the LDO to the supply voltage (i. e. the storage capacitor), thus supplying the load. When the voltage on the storage capacitor decreases below 3.8 V, the LDO is disconnected and the load switched off. In Section 2.4.1 we presented the solar source characterization of the same structure implemented on this chip, used to design an equivalent circuit described in Section 2.4.3. Those results are fundamental for the design of the subsequent power management system. In Section 2.4.4 we describe the charge pump used to elevate the solar cell voltage to a usable value, while Section 2.4.5 and Section 2.4.8 present the power management system and the LDO, respectively. Finally, in Section 2.4.9 we derive the criteria for the choice of the value of the storage capacitance.

2.4.3 Miniaturized solar cell model

On the basis of the results obtained from the characterization of the test chip, we developed an equivalent circuit model of the solar cell implemented on the harvester chip. Fig. 2.11 shows the power curve used to create the equivalent circuit model, illustrated in Fig. 2.13. In particular, by means of a Matlab algorithm which needs only five measured values of the output power to find the appropriate model parameters, we achieved the following result:

- I_{ph} = 12.28 µA;
- A_D = 100 µm^2;
- P_D = 40 µm;

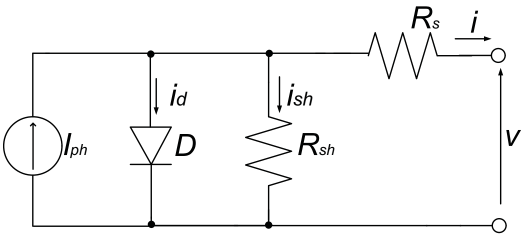

Figure 2.13: Solar cell circuit model

- R_{sh} = 40 kΩ;
- R_s = 2.27 kΩ.

Current generator I_{ph} represents the photo-generated current of a 1 mm^2 solar structure, with the geometrical path of p diffusion of structure C in Fig. 2.7. A_D and P_D are the area and the perimeter of the loss diode D, respectively. The loss diode represent the loss of dark current which flows across the device under an applied voltage, or bias. Resistor R_{sh} is the shunt resistance of the equivalent circuit of the solar cell while R_s is the output series resistance. Indeed, in actual cells some power is dissipated trough the contacts resistance and trough leakage currents around the sides of the device. These effects are equivalent electrically to two parasitic resistances in series (R_s) and in parallel (R_{sh}) with the cell. The series resistance arises from the resistance of the cell material to current flow, particularly trough the front surface to the contacts, and from resistive contacts. Series resistance is a particular problem at high current densities, for instance under concentrated light. The parallel or shunt resistance arises from leakage of current trough the cell, around the edges of the device and between contacts of different polarity. It is a problem in poorly rectifying devices. When parasitic resistances are included, the equation of the current provided to the load by the

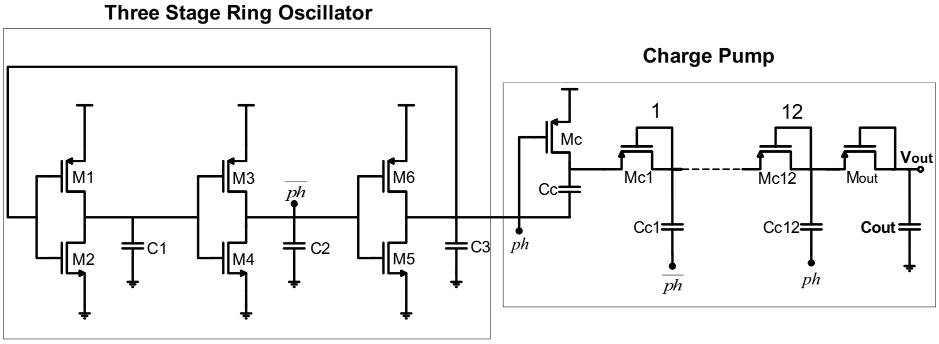

Figure 2.14: Schematic of the ring oscillator and of the charge pump

cell becomes

$$I_{LOAD} = I_{ph} - I_0\left(e^{\frac{q(V+IR_s)}{kT}} - 1\right) - \frac{V+IR_s}{R_{sh}} \tag{2.13}$$

The output power curve of the created model is very close to the power curve of the referred cell illuminated with an incident light power of 400 W/m^2.

2.4.4 Ring oscillator and charge pump

The ring oscillator and the charge pump shown in Fig. 2.14 represent the front-end block of the power management circuit. In order to allow the voltage across the storage capacitor to reach at least 4 V, a Dickson charge pump [35] has been implemented. The circuit requires two non-overlapping clock phases, *ph* and $\overline{ph}$, with amplitude equal to the voltage produced by the micro solar cell V_{ph}. The charge pump operates by moving charge along the diode chain, charging the capacitors to increasing voltages. The charge pump has been designed to obtained a voltage of 5 V, starting from $V_{ph} \cong 500$ mV, thus requiring 12 stages. A three stage ring oscillator provides the clock phases for the charge pump with a frequency equal to 29.5 kHz, which correspond to the best trade-off between time required to charge C_c and the charge transfer rate. The performance of the system is limited by the supply voltage, which is equal to the open-circuit voltage V_{ph}

of the integrated micro solar cell, that forces all transistors to work in the sub-threshold region. Such a system provides a very low current flow through each transistor, introducing an efficiency loss in terms of charge transfer, and hence, in terms of charging time. In order to provide a constant voltage of 3.3 V to the load with a significant current for an established time slot, a storage capacitor is necessary. Therefore, the proposed system is only suitable for loads operated in discrete-time regime, such as sensor network nodes.

2.4.5 Power monitoring circuit

In order to control the voltage across the storage capacitor and hence the stored energy, we developed a power monitoring circuit, which consists of an hysteresis comparator and a voltage level shifter. The management circuit provides a control signal to a switch, which connects the load to the storage capacitor when the voltage across the storage capacitor reaches 4.3 V and disconnects the load when it becomes lower than 3.8 V. In order to avoid discharging the storage capacitor, the comparator is supplied directly by an auxiliary solar cell, while the inverter is connected to the storage capacitor voltage. The total current consumption of the monitoring block is less than 10 nA when the load is disconnected.

2.4.6 Hysteresis comparator

In order to control the charge and discharge status of the external capacitor, the hysteresis comparator monitors the voltage on the capacitor, connects the load when it reaches 4.3 V, and disconnect it when it decrease to 3.8 V. The schematic of the comparator circuit is shown in Fig. 2.15. Hysteresis is required to have a rising threshold different from the falling threshold. The hysteresis value of this solution is proportional to the ratios β_{MP4}/β_{MP3} and β_{MP5}/β_{MP10}. Assume that initially the input voltage V$_{ref}$ is much lower than the threshold voltage of the

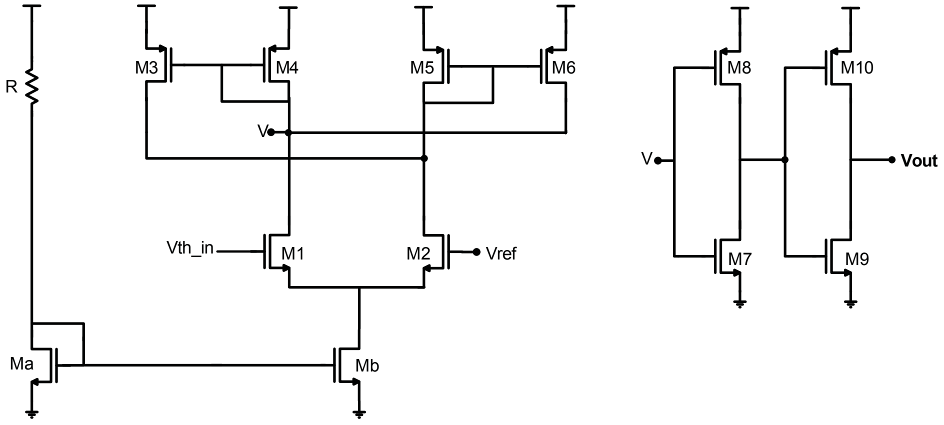

Figure 2.15: Schematic of the hysteresis comparator

comparator. In this case all the current flows through M1 and M4; M5 and M6 are off and consequently the output voltage is low. M3 is on too, but no current is flowing in it. Initially when the input voltage increases nothing happens until $V_{ref} \simeq V_{th_in}$. At this point some current starts to flow into M2 from M3 and M1 and I$_{M1}$ starts to decrease. Therefore, the following relations can be written, assuming α_r as the ratio β_{M3}/β_{M4} (footer r stands for rising):

$$I_{M_2} = I_{M_3} = \alpha_r I_{M_4} \tag{2.14}$$

$$I_{M_1} + I_{M_2} = I_{R_{bias}} \tag{2.15}$$

$$I_{M_1} + \alpha_r I_{M_4} = I_{R_{bias}} \tag{2.16}$$

$$I_{M_2} = \alpha_r I_{M_4} \propto (V_{ref} - V_{th\text{-}in})^2 \tag{2.17}$$

If the input voltage is increased further on, M2 demands for more current that can come only from M3 that mirrors I$_{M4}$ with the ratio α_r, while I$_{M4}$ is decreasing. At a certain point, M3 ($\alpha_r I_{M4}$) cannot validate the equation (2.16), because I$_{M3}$ = I$_{M1}$ is too low and consequently M3 goes on, providing the current M2 is asking, given by

$$I_{M_2} + I_{M_3} = I_{R_{bias}} \tag{2.18}$$

The last value of V$_{in}$ that verifies equation (2.16) is the rising-decision threshold and the difference $V_{th-in} - V_{ref}$ is the value of the rising-hysteresis that is proportional to α_r. So its value can be changed by the α_r parameter: the larger is α_r, the longer equation (2.16) is verified and the higher is the rising-hysteresis that validates equation (2.17). It is important to point out that all equations are true only when V$_{th-in}$ $\cong$V$_{ref}$ and equation (2.18) only when the output voltage is high. The same operations happen symmetrically in the falling decision.

2.4.7 Voltage level shifter

In order to drive properly the load switch a voltage level shifter has been implemented. In particular when the voltage across the storage capacitor (V$_{storage}$) reaches the established value, the level shifter has to drive the connection switch to be on, while during the charging phase to be off, in order to disconnect the load and avoid the power consumption. Fig. 2.16 shows the schematic of the voltage level shifter. When V$_{IN}$ in high, V$_{G_{M2}}$ is low, M1 is on, and V$_{G_{M4}}$ is low, thus switching on M4. Consequently V$_{out}$ is set to V$_{storage}$. When V$_{IN}$ is low, the behavior of the system is symmetrical and hence the output node is at ground value.

2.4.8 Voltage regulator

In order to provide a fixed 3.3 V supply to the actual load, a linear voltage regulator (LDO) has been implemented. It consists of a a bandgap circuit and a regulator circuit. This block is supplied when the storage capacitor has reached the proper voltage. Fig. 2.4.8 shows the schematic of the voltage regulator. The total current consumption of the circuit is less than 2 µA.

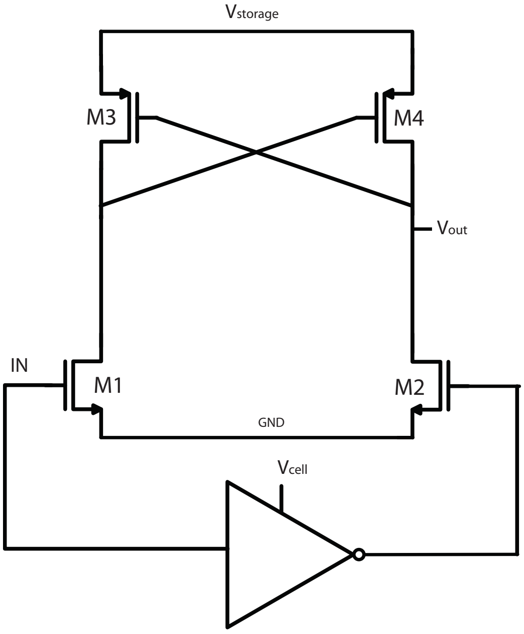

Figure 2.16: Schematic of the voltage level shifter

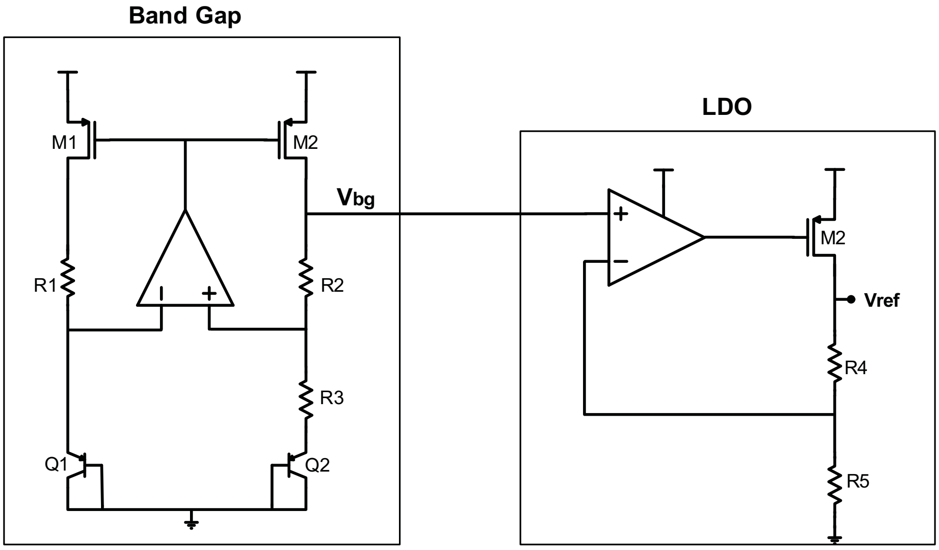

Figure 2.17: Schematic of the linear voltage regulator

Bandgap circuit

The bandgap circuit provides a stable voltage reference (V_{bg}) as reference input of the LDO. It operates compensating the negative temperature coefficient of a *pn*-junction voltage V_{be}, with the positive temperature coefficient of the thermal voltage V_T. The output voltage of the circuit is

$$V_{bg} = V_{be} + mV_T \tag{2.19}$$

where m depends on the bandgap circuit topology. With the topology used, m coefficient is given by

$$m = \frac{R_2}{R_1} \ln\left[\frac{(W_1/L_1)}{(W_2/L_2)}\frac{A_2}{A_1}\right] \tag{2.20}$$

Even if the supply voltage follows the discharge curve of the storage capacitor, V_{bg} remains constant.

LDO

The LDO provides a stable 3.3 V supply voltage with an input voltage ranging from 3.3 V to 4.8 V, allowing the actual load to operate properly. In particular, the output voltage is given by

$$V_{ref} = V_{bg}\frac{R_4 + R_5}{R_4}. \tag{2.21}$$

Simulation results demonstrate that the output voltage has a maximum error of 0.3% over the whole input voltage range, although, in order to reduce the power dissipation, R_4 and R_5 are in the MΩ range. The total current consumption is about 1 µA.

2.4.9 Storage capacitor sizing

The storage capacitor is an external component, and, hence, its value can be chosen on the basis of the actual load power consumption. In particular, the charge transfer rate of the charge pump in the range from 3.8 V to 4.3 V is less than

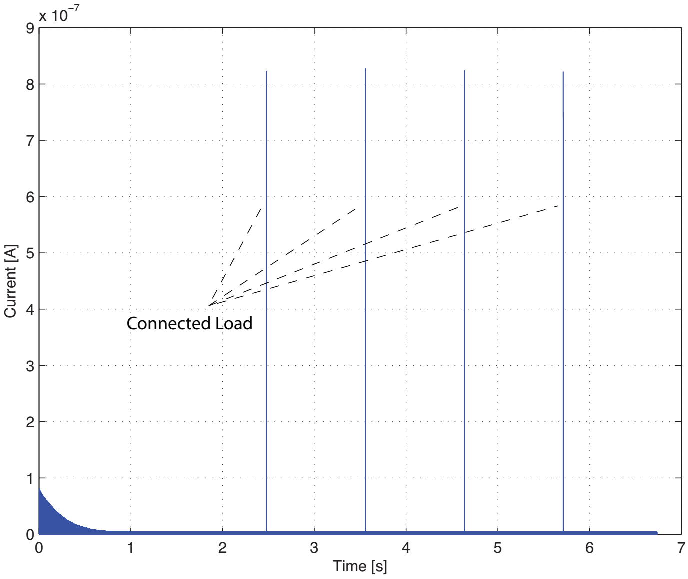

Figure 2.18: Simulation of the current flowing through the storage capacitor

10 nA. Most of efficiency is lost in the charge pump, but this is not particularly important, because the system is able to store energy and provide it to the actual load only when it is enough to allow proper operation in an established time-slot. Fig. 2.18 shows the current in a 10 nF storage capacitor during the charge process and when the load is connected. The storage capacitor voltage working cycle is shown in Fig. 2.19. If the load would require longer working time it is enough to use a larger storage capacitor, leading to a lower duty cycle. In particular the charging time is proportional to the current I_{load} that the load needs for a time-slot t_w. [h!]

2.4.10 Experimental results

Fig. 2.20 shows the micro-photograph of the realized chip. In order to characterize this harvester solution, we initially verified the correct behavior of the power management system. Indeed, the monitoring of the stored charge in the external

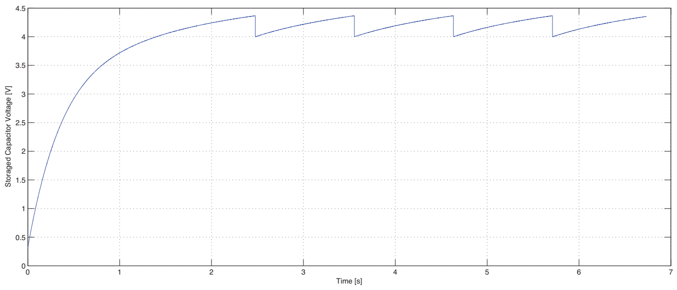

Figure 2.19: Simulation of the voltage across the storage capacitor

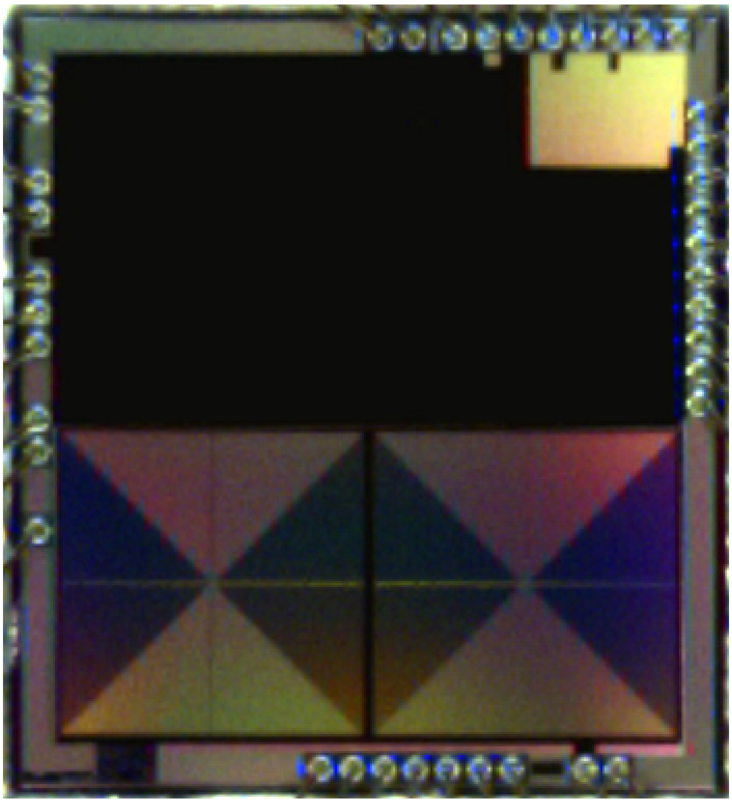

Figure 2.20: Microphotograph of the chip

capacitor is correct, and the driving signal of the voltage level shifter is determined by a free setting threshold dependency of the comparator. Fig. 2.21 shows the result of an acquisition from the oscilloscope during a working cycle. As it

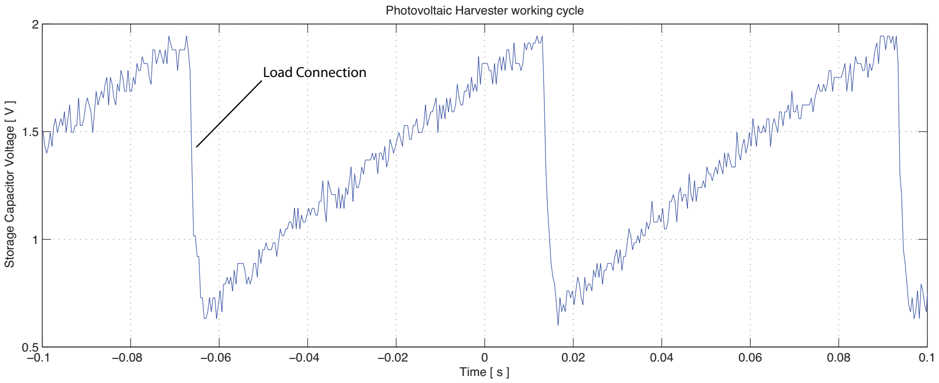

Figure 2.21: Measurement of the voltage across the storage capacitor

is possible to notice, when the voltage across the storage capacitor reaches the desired value, the accumulated charge is transfered to the load. The working cycle presented in Fig. 2.21 corresponds to the voltage across a resistor of 1 MΩ, connected as load to the drain of the output pMOS switch. This transistor presents a problematic leakage current that elevate the drain voltage proportionally to the impedance applied as load. This represent a problem because this leakage current is subtracted to the output of the charge pump, limiting the maximum reachable voltage across the storage capacitor. This problem can be solved in a second release with a more complex electronic structure for the connection pMOS switch.

2.5 Integrated Stabilized Photovoltaic Energy Harvester

In this section we present a second solution of photovoltaic power generator. The energy harvesting device exploits the power generated by several on-chip micro photovoltaic cells connected in series to provide the supply voltage and the reference voltages for an integrated voltage regulator and an autonomous temperature sensor. The regulator operates also with low illumination levels or large load currents, and tolerates a wide variation of the voltage produced by the micro photovoltaic cell chain. In order to allow the series connection of several photovoltaic cells, we used an SOI technology, where parasitic p-n junctions to the substrate are not present. This photovoltaic harvester is particularly suitable for continuous time systems, such as sensor supply. The efficiency of this solution is drastically improved, because of the absence of the charge pump. The SOI technology in fact allows to isolate the photovoltaic structures with an oxide trench, thus eliminating the problem of the common substrate. The system consists in a series of 35 trenched p-n junction, a bandgap reference voltage circuit [36] and a high voltage LDO circuit [37]. This regulator allows us to provide a fixed 3.3 V supply, also in low environment illumination conditions, as the large number of solar cells in series allow each cell to decrease its voltage of almost 20%, as it happens when the power curve change due to illumination variations, or larger load power request than typical.

2.5.1 Micro solar cells

Figure 2.22 shows the realized solar cell structure. Each cell is composed by a p-well insulated with oxide from the common p-substrate of the chip. In order to create p-n junctions, several rows of n-diffusion have been realized within the p-well. This configuration allows us to create series structures, and provide a voltage higher than 3.3 V. In particular, as the open circuit voltage V_{oc} obtained for each illuminated cell is almost 500 mV, the entire chain can provide 17.5 V. This value ensures that the system can work, ideally, even with a 20% reduction of nominal open circuit voltage. The voltage reduction can be caused by an illumination reduction, or an high load power request. Moreover the series configuration of solar cells, allows us to obtain all the reference voltages required for the entire system. The geometrical dimensions of each cell are 385 μm $\times$ 245 μm. The

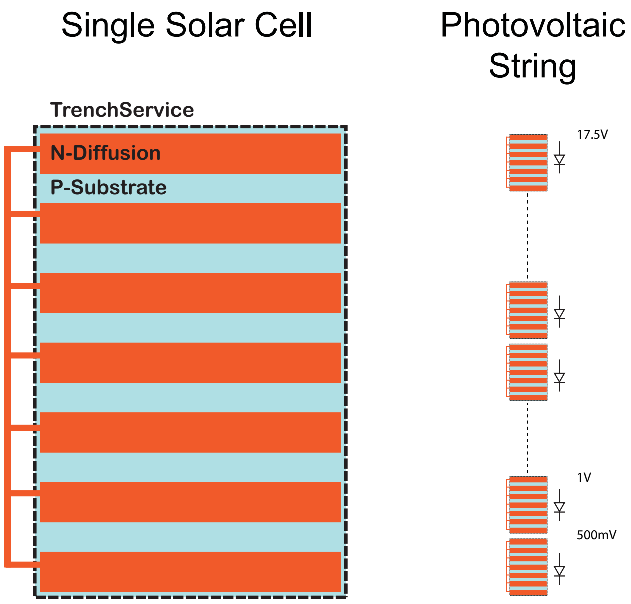

Figure 2.22: Integrated micro solar cell structure

width of the depletion region is defined as

$$x_{dr} = \sqrt{\frac{3\epsilon_{si}(\phi_{bi})}{q}(\frac{1}{N_a} + \frac{1}{N_d})} \tag{2.22}$$

where ϵ_{si} is the silicon dielectric permittivity, q the charge of the electron, N_a the p-type substrate doping concentration, N_d the n-diffusion doping concentration and ϕ_{bi} is the built-in potential, given by

$$\phi_{bi} = V_t ln(\frac{N_a N_d}{n_i^2}) \tag{2.23}$$

where V_t is equal to the thermal voltage. Substituting the respective values in each variable, x_{dr} results equal to 3.2 µm. Keeping some safety margin, the dimensions of the n-diffusion and the space among each row has been set to 5 µm. To estimate the photo-generated power, we refer to the obtained results of the characterization of the realized test chip presented in the paragraph 2.4.1. In particular consider the power curve of Fig. 2.11-C. As the doping concentrations can be assumed as the same, and the area of the SOI solar cell is almost 2.7 smaller that the measured, we can estimate a short-circuit current I_{sc} of about 22µA.

2.5.2 Bandgap Reference Circuit

The output voltage of a bandgap reference is obtained by adding two components: the base-emitter voltage of a BJT transistor (V_{be}) and a term proportional to the absolute temperature (V_{PTAT}). These two components feature temperature coefficients with opposite sign. In particular, it is well known that to compensate the temperature dependence of V_{be} we have to multiply $V_T = kT/q$ by approximately 22. If this condition is satisfied, the resulting output voltage, approximately equal to 1.2 V, is at first order temperature independent.

Fig. 2.23 shows the schematic of the bandgap reference circuit used in the proposed system. This circuit must manage the variations of the supply voltage, due to illumination reduction or output power changes, providing a constant reference voltage, equal to 1.199 V, to the LDO. The current that flows in $M4$ and $M5$ is mirrored in $M3$, thus biasing the two external branches with $I_{d_{M3}} = I_{d,M8} + I_{b,Q1} + I_{b,Q2}$. Since $I_{d,M4} = I_{d,M5}$, it results that $V_{gs,M6} = V_{gs,M7}$. The BJT transistors, with emitter area ratio equal to 8, drain the same current, leading to a ΔV_{be} equal to $V_T \ln(8)$. The resulting current flowing through the BJT transistors is

$$I_{R1} = \frac{V_T \ln(8)}{R1}. \tag{2.24}$$

At 27 °C I_{R1} is equal to about 1 µA. Since the same current is mirrored in $M3$ and $M8$, the total power consumption of the circuit is

$$P_{TOT} = (I_{d,M3} + I_{d,M4} + I_{d,M5} + I_{d,M8} + I_{c,Q1} + I_{c,Q2})\, V_{dd}. \tag{2.25}$$

with V_{dd} equal to the photo-generated voltage of the 7th micro-photovoltaic cell of the series chain (nominally 3.5 V). The total current consumption obtained in simulation is equal to 4.17 µA. Tab. 2.5 reports the dimensions of each component of the circuit.

As shown in Fig. 2.23 the used bandgap reference circuit does not require any operational amplifier. The output voltage is fixed by the feedback loop including

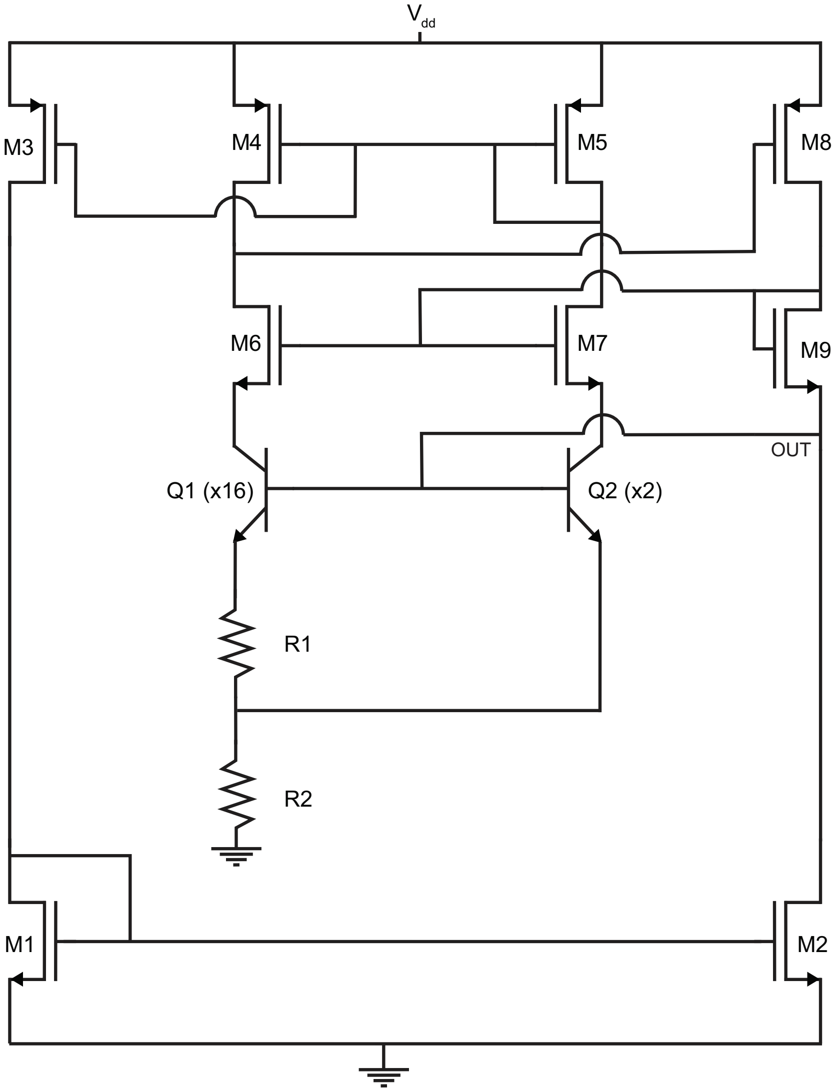

Figure 2.23: Schematic of the bandgap reference circuit

Table 2.5: Component Dimensions of the Bandgap Reference Circuit

Component Name	***Component Parameter***
$M4$, $M5$, $M3$, $M8$	W = 10 µm, L = 4 µm
$M6$, $M7$, $M9$	W = 5 µm, L = 2 µm
$M1$, $M2$	W = 5 µm, L = 4 µm
$R1$	40 kΩ
$R2$	200 kΩ

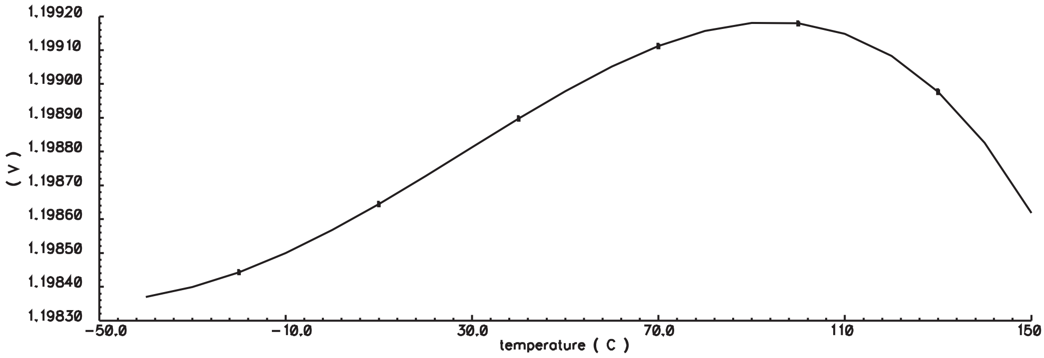

Figure 2.24: Simulated temperature dependence of the bandgap reference voltage

transistor $M8$, which compensates any eventual variation of $V_{be,Q1,Q2}$. The cascode transistors $M6$ and $M7$ are used to increase the gain of the loop. Considering in simulation a temperature ranging from −40 °C to 150 °C, the output voltage in typical conditions shows a variation of 0.8 mV, corresponding to 3.5 ppm/°C, as illustrated in Fig. 2.24. In worst cases the variation of the output voltage ranges from 6.6 mV to 8 mV (from 29 ppm/°C to 35 ppm/°C).

In order to emulate a reduction of the incident light power, we simulated the bandgap reference circuit with a ramp applied to the power supply voltage V_{dd}, finding the minimum micro-photovoltaic cell voltage required to start-up the circuit at different temperatures. The achieved results are summarized in Tab. 2.6. In order to reduce the power consumption, current $I_{d_{M3}}$ is mirrored to bias also the LDO circuit.

Table 2.6: Minimum Bandgap Reference Circuit Operating Voltage

Temperature [°C]	***Minimum Photovoltaic Cell Voltage*** **[mV]**
−40	365.4
27	362.4
150	352

2.5.3 LDO Circuit

The schematic of the proposed LDO circuit is shown in Fig. 2.25. It consists of an error amplifier ($M6$, $M7$, $M4$, $M5$, $Mbias$), an output stage ($M1$, $M2$, $M8$, $M9$, Ma, Mb), a pass transistor (Mc) and a resistive divider ($R1$, $R2$). The circuit is basically an operational amplifier with resistive feedback. The output voltage (V_{out}) is an amplified version of the bandgap voltage reference ($V_{Bandgap}$). Transistor $M1$ mirrors the current of the bandgap circuit, biasing the output stage composed of transistors $M8$ and $M9$. The error amplifier is supplied with the voltage obtained from the 7th photovoltaic cell of the series chain (V_{dd}, as the bandgap reference circuit), while the output stage and the pass transistor are supplied by the maximum voltage of the chain, corresponding to the 35th cell (HV_{dd}), with a nominal

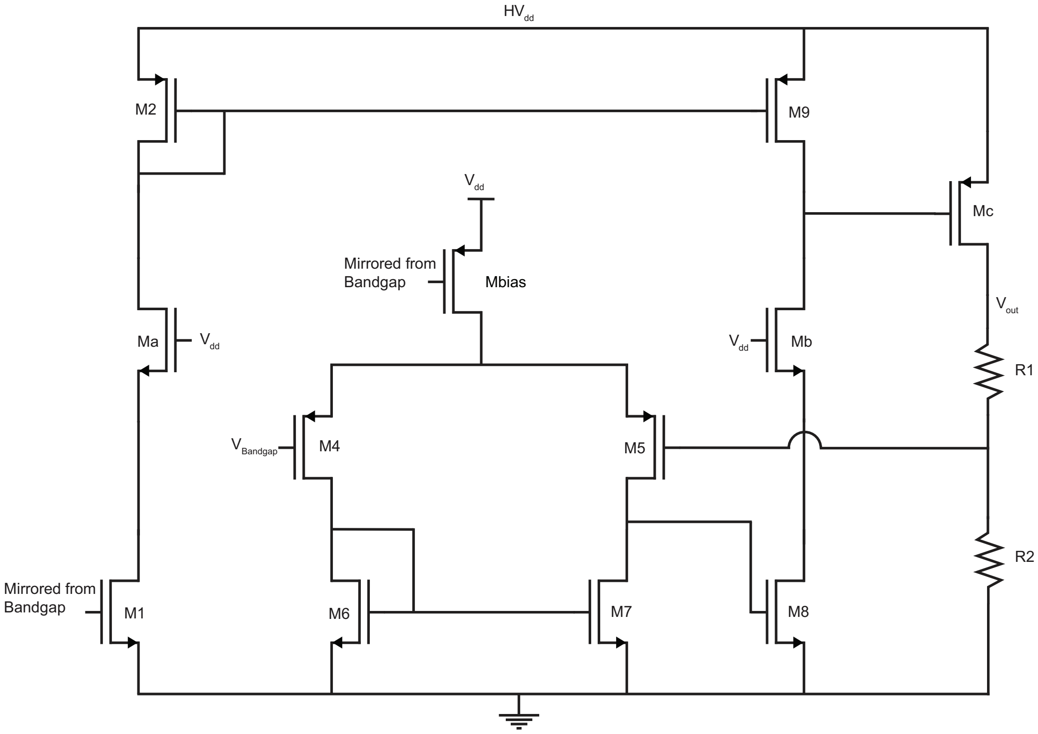

Figure 2.25: Schematic of the LDO circuit

Table 2.7: Component Dimensions of the LDO Circuit

Component Name	***Component Parameter***
$M2$, $M9$	W = 6 µm, L = 4 µm
Ma, Mb	W = 6 µm, L = 2 µm
Mc	W = 24 µm, L = 2 µm
$M1$, $M3$	W = 10 µm, L = 4 µm
$M4$, $M5$	W = 10 µm, L = 2 µm
$M6$, $M7$	W = 4 µm, L = 4 µm
$M8$	W = 0.5 µm, L = 0.35 µm
$R1$	1 MΩ
$R2$	1.8 MΩ

value of 17.5 V. To protect $M1$ and $M8$ from the high voltage, we introduced a cascode structure with the high-voltage transistors Ma and Mb.

The transfer function of the LDO circuit can be written as

$$\frac{V_{out}}{V_{Bandgap}} = \frac{A}{1 - A\beta}, \tag{2.26}$$

where

$$A = g_{m5}\left(r_{ds5} \| r_{ds7}\right) g_{m8} r_{ds9} \tag{2.27}$$

and

$$\beta = \frac{R2}{R1 + R2}. \tag{2.28}$$

Assuming $A\beta \gg 1$, we obtain

$$\frac{V_{out}}{V_{Bandgap}} = 1 + \frac{R2}{R1} = 2.8, \tag{2.29}$$

and, hence, starting from a bandgap reference voltage of 1.2 V, we obtain an output voltage equal to 3.3 V. Tab. 2.7 summarizes the dimensions of all the devices of the proposed LDO circuit.

The total current consumption of the LDO circuit is 3.25 µA, while the total power dissipation depends on the incident light.

Table 2.8: Minimum System Operating Voltage

Temperature **[°C]**	***Minimum Photovoltaic Cell Voltage*** **[mV]**
–40	390.8
27	362.4
150	352

2.5.4 Simulation Results

The whole system has been extensively simulated at transistor level, considering also temperature and process variations. To simulate the variation of the incident light intensity, the system has been supplied with a ramp voltage. In particular, we varied the single cell voltage in a range between 0 V and 0.5 V (V_{dd} ranges from 0 V to 3.5 V, while HV_{dd} ranges from 0 V to 17.5 V). Tab. 2.8 summarizes the minimum voltage required for the system to properly start-up at different temperatures, while Fig. 2.26 shows the transient simulation at 27 °C.

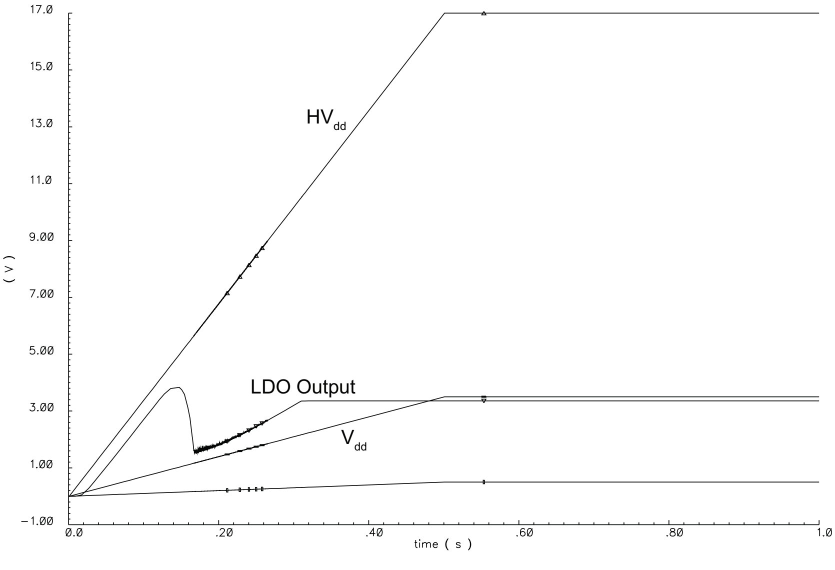

Figure 2.26: Transient simulation of the system start-up with variable illumination

Fig. 2.27 shows the output voltage of the proposed system as a function of the temperature in the range from −40 °C to 150 °C. The overall output variation results about 2.2 mV. The phase margin of the system results 75° with 10 pF of capacitive load.

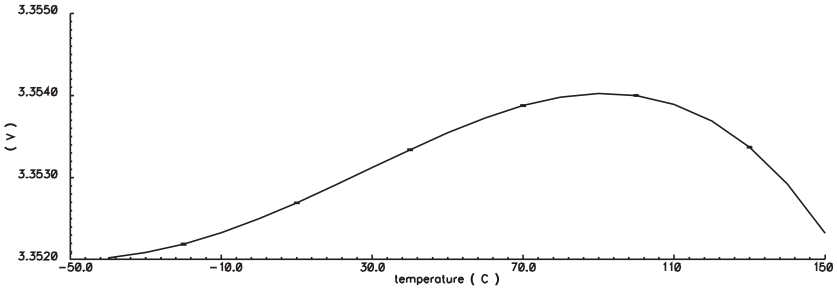

Figure 2.27: System output voltage as a function of temperature

Fig. 2.28 shows the layout of the chip. The total area is about 4.5 mm^2, with only 10% occupied by the electronics. Tab. 2.9 summarizes the simulated performance of the system.

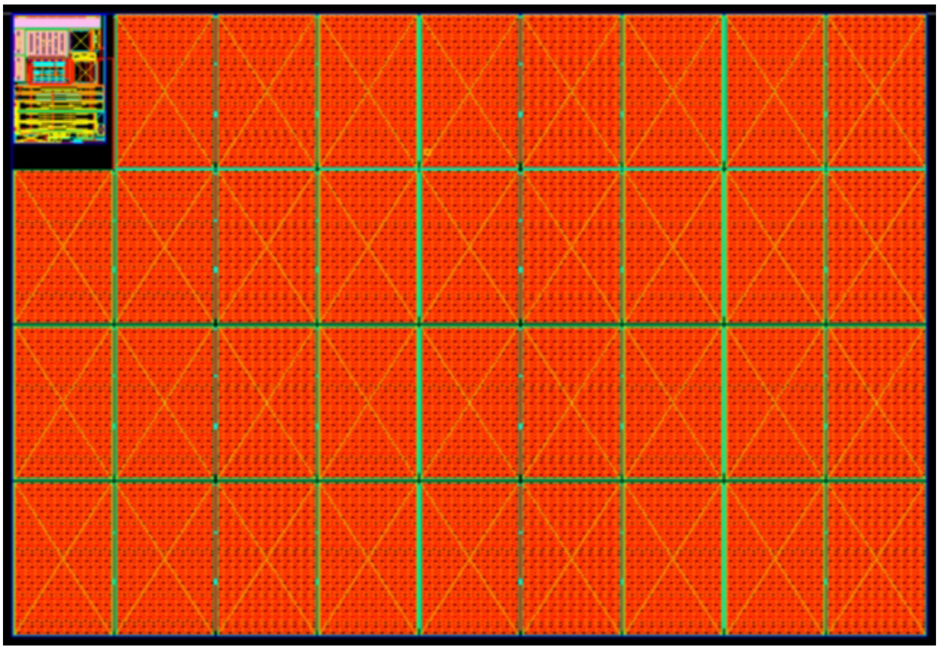

Figure 2.28: Layout of the chip

Table 2.9: System Performance

Parameter	***Value***
PSRR (DC)	−130 dB
PSRR (1 kHz)	−82.6 dB
PSRR (100 kHz)	−42.9 dB
Phase margin (10 pF load)	75°
Bandgap current consumption	4.17 µA
Bandgap temperature variation (−40 °C – 150 °C)	800 µV (3.5 ppm/°C)
LDO current consumption	3.25 µA
Output voltage temperature variation (−40 °C – 150 °C)	2.2 mV (3.5 ppm/°C)
Total current consumption	7.42 µA
Minimum photovoltaic cell voltage (27 °C)	362 mV

2.5.5 Temperature Sensor

In order to validate the adopted energy harvesting concept, we also implemented on-chip a temperature sensor. To this end, the temperature dependent bias current of the bandgap circuit has been mirrored in an additional branch. This current, flowing through a resistor produces a temperature dependent voltage, as shown in Fig. 2.29. The value of the sensing resistor is 6.8 MΩ, and the system has been simulated in the temperature range from −40° C to 150° C.

2.5.6 Experimental Results

Fig. 2.30 shows the microphotograph of the implemented device. The total area of the chip is about 4 mm^2, and it has been fabricated with a 0.35-µm SOI CMOS technology. The electronics has been shielded by a metal layer to avoid illumination, and it is represented by the matt rectangle on the left bottom side of Fig. 2.30. Fig. 2.31 shows the power curve of a reference photovoltaic cell, obtained changing the load current value with a power of the incident constant spectrum light equal to 300 W/m^2. Fig. 2.32 shows the power curve on a resistive load applied to

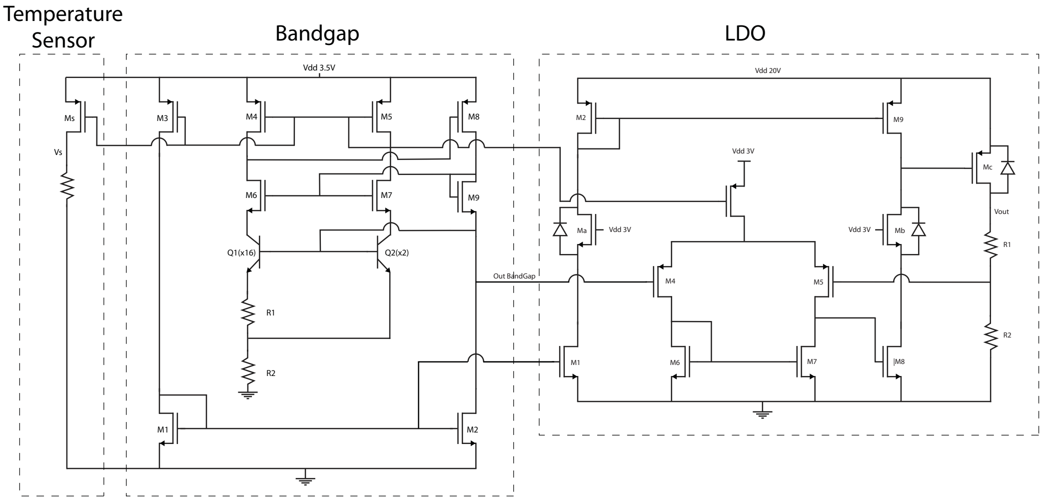

Figure 2.29: Schematic of the complete system including the autonomous temperature sensor

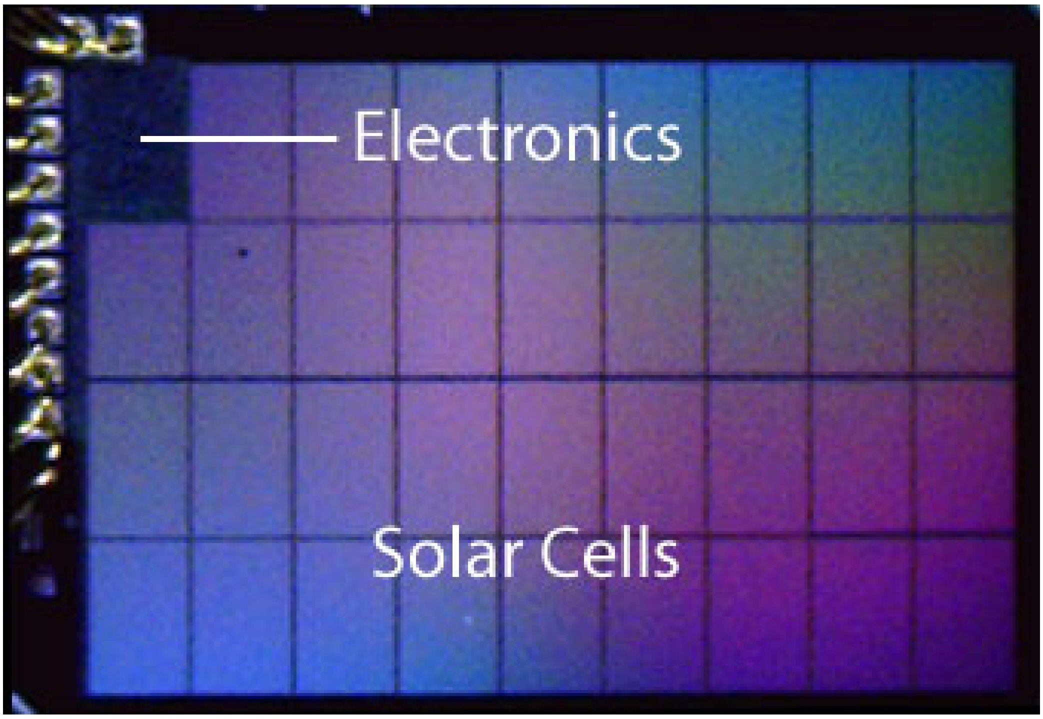

Figure 2.30: Microphotograph of the chip

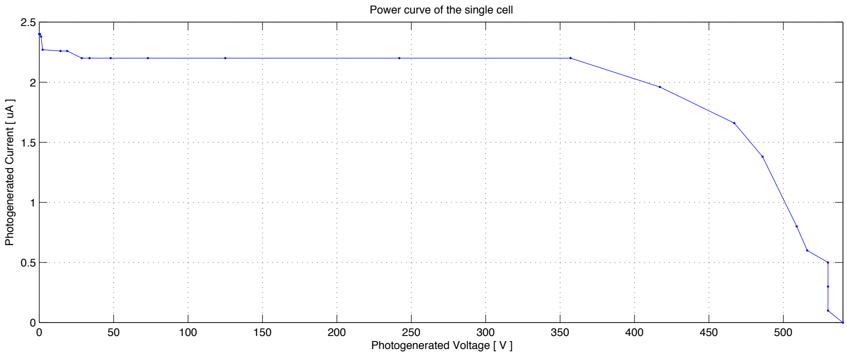

Figure 2.31: Power curve of a reference photovoltaic cell

the voltage regulator. The characterization has been obtained with a constant incident light power of 600 W/m^2. Fig. 2.33 shows the transfer characteristic of the temperature sensor, measured monitoring the temperature in a range from 27° C to 60° C. The measured linearity is 4.2%, with a sensitivity of 3.8 mV/° C . Fig. 2.34 summarizes the performance of the system.

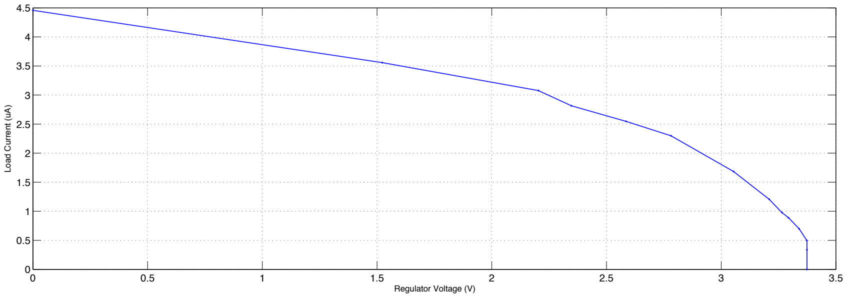

Figure 2.32: Power curve of the voltage regulator

2.5.7 Outlook

Micro-energy harvesters from various sources such as light, motion, thermal, or RF will allow engineers to circumvent the physical burden of batteries and applications no longer have to be limited by their accessibility for maintenance. Low-

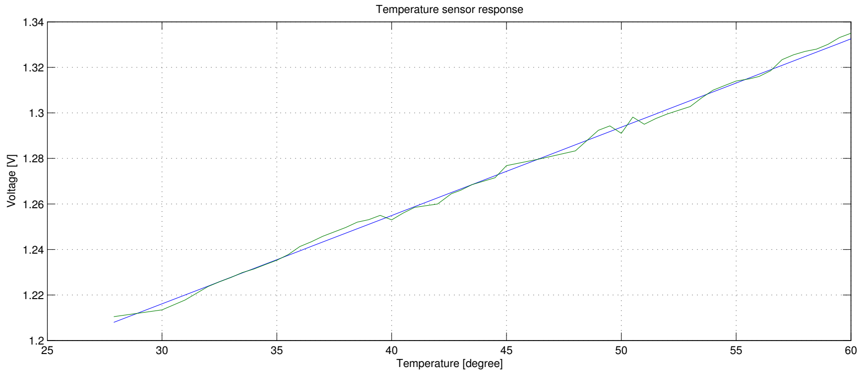

Figure 2.33: Temperature sensor response

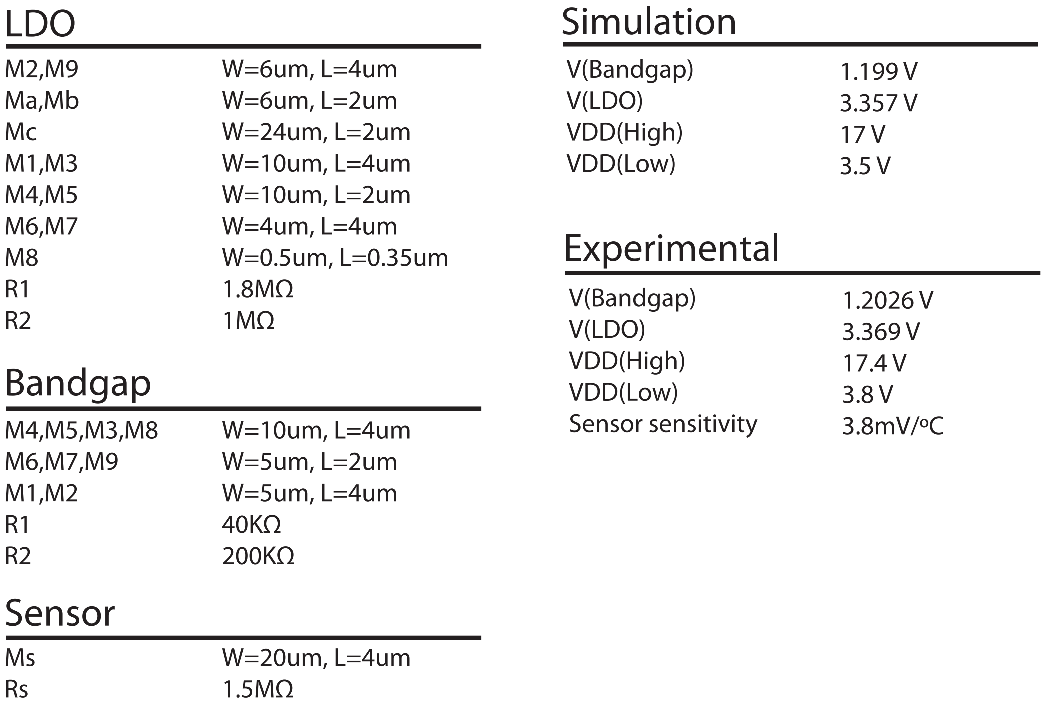

LDO	
M2,M9	W=6um, L=4um
Ma,Mb	W=6um, L=2um
Mc	W=24um, L=2um
M1,M3	W=10um, L=4um
M4,M5	W=10um, L=2um
M6,M7	W=4um, L=4um
M8	W=0.5um, L=0.35um
R1	1.8MΩ
R2	1MΩ

Bandgap	
M4,M5,M3,M8	W=10um, L=4um
M6,M7,M9	W=5um, L=2um
M1,M2	W=5um, L=4um
R1	40KΩ
R2	200KΩ

Sensor	
Ms	W=20um, L=4um
Rs	1.5MΩ

Simulation	
V(Bandgap)	1.199 V
V(LDO)	3.357 V
VDD(High)	17 V
VDD(Low)	3.5 V

Experimental	
V(Bandgap)	1.2026 V
V(LDO)	3.369 V
VDD(High)	17.4 V
VDD(Low)	3.8 V
Sensor sensitivity	3.8mV/°C

Figure 2.34: Summary of the performance of the system

cost, autonomous sensor networks will not only enrich our lives by providing valuable data about the status of our environment, but they will do so with no long term, reoccurring cost or impact on the environment. Energy harvesting will extend the usable life of existing products and will enable design options that were not possible before. Some applications may sound like science fiction today, but the technology exists to enable a new generation of applications. By harvesting the vibrational energy, intelligent sensors will be able to be implanted in roads, bridges, and buildings at the time of construction, providing real-time feedback on the structural integrity guaranteeing our safety. By harvesting energy from the sun, farmers will be able to monitor the health of their crop using low-cost, disposable sensors, producing greater crop yield with lower maintenance. By harvesting the heat from the skin, smart band-aids smaller than a quarter will be able to monitor patient's vital signs and transmit the information wirelessly to a central medical base station, without having to tether a patient to a machine. We just need to break the design engineer's mold of what a traditional power source needs to look like and embrace the benefits of perpetually powered energy harvesting systems.

Appendix A

PIC 16F877 Datasheet

MICROCHIP

PIC16F87X

Devices Included in this Data Sheet:

- PIC16F873
- PIC16F874
- PIC16F876
- PIC16F877

Microcontroller Core Features:

- High performance RISC CPU
- Only 35 single word instructions to learn
- All single cycle instructions except for program branches which are two cycle
- Operating speed: DC - 20 MHz clock input
  DC - 200 ns instruction cycle
- Up to 8K x 14 words of FLASH Program Memory,
  Up to 368 x 8 bytes of Data Memory (RAM)
  Up to 256 x 8 bytes of EEPROM Data Memory
- Pinout compatible to the PIC16C73B/74B/76/77
- Interrupt capability (up to 14 sources)
- Eight level deep hardware stack
- Direct, indirect and relative addressing modes
- Power-on Reset (POR)
- Power-up Timer (PWRT) and
  Oscillator Start-up Timer (OST)
- Watchdog Timer (WDT) with its own on-chip RC oscillator for reliable operation
- Programmable code protection
- Power saving SLEEP mode
- Selectable oscillator options
- Low power, high speed CMOS FLASH/EEPROM technology
- Fully static design
- In-Circuit Serial Programming™ (ICSP) via two pins
- Single 5V In-Circuit Serial Programming capability
- In-Circuit Debugging via two pins
- Processor read/write access to program memory
- Wide operating voltage range: 2.0V to 5.5V
- High Sink/Source Current: 25 mA
- Commercial, Industrial and Extended temperature ranges
- Low-power consumption:
  - < 0.6 mA typical @ 3V, 4 MHz
  - 20 μA typical @ 3V, 32 kHz
  - < 1 μA typical standby current

Pin Diagram

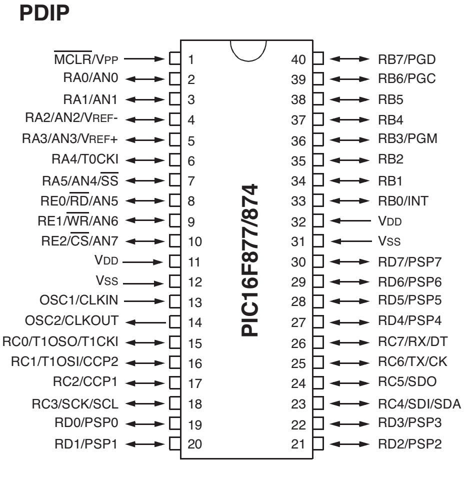

Peripheral Features:

- Timer0: 8-bit timer/counter with 8-bit prescaler
- Timer1: 16-bit timer/counter with prescaler, can be incremented during SLEEP via external crystal/clock
- Timer2: 8-bit timer/counter with 8-bit period register, prescaler and postscaler
- Two Capture, Compare, PWM modules
  - Capture is 16-bit, max. resolution is 12.5 ns
  - Compare is 16-bit, max. resolution is 200 ns
  - PWM max. resolution is 10-bit
- 10-bit multi-channel Analog-to-Digital converter
- Synchronous Serial Port (SSP) with SPI™ (Master mode) and I^{2}C™ (Master/Slave)
- Universal Synchronous Asynchronous Receiver Transmitter (USART/SCI) with 9-bit address detection
- Parallel Slave Port (PSP) 8-bits wide, with external $\overline{\text{RD}}$, $\overline{\text{WR}}$ and $\overline{\text{CS}}$ controls (40/44-pin only)
- Brown-out detection circuitry for Brown-out Reset (BOR)

Conclusions

In this thesis we have presented the design of integrated magnetic sensor interface circuits and photovoltaic energy harvesting solutions.

Initially, we realized an automated measurement setup to improve the reliability of the result obtained with different approaches in the characterization of Fluxgate magnetic sensors. The performance of the system has been improved by more then 50%. Then a new Fluxgate magnetic sensor interface circuit has been designed. Special care has been taken in order to reduce the total power consumption, as the final portable application is a current measurement system with digital output.

The energy harvesting solutions that has been proposed are suitable for discrete and continuous time working systems. The first is a sort of solar battery with a power management system, and the second is a photovoltaic voltage regulator with an autonomous temperature sensor. All the obtained results have been published in national and international conferences. The details of the publications can be found at http://sms.unipv.it/%7emferri.

Bibliography

[1] R. Boll and K. Overshott, *Magnetic Sensors, Volume 5, Sensors: A Comprehensive Survey*. Wiley-VCH, 12 1989.

[2] P. Ripka and P. Navatril, “Fluxgate sensors for magnetopneumometry,” in *Proceedings of Sensors and Actuators A: Physical*, vol. 60, May 1997, pp. 76–79.

[3] W. Hernandez, “Fluxgate magnetometer for magnetic fields in the range 1-100 Î¼t,” *Electronics Letters*, vol. 31, no. 24, pp. 2110–2111, Nov 1995.

[4] P. M. Drljaca, P. Kejik, F. Vincent, D. Piguet, and R. S. Popovic, “Low-power 2D fully integrated CMOS fluxgate magnetometer,” *IEEE Sensors Journal*, vol. 5, pp. 909–915, Oct. 2005.

[5] S. Choi, S. Kawahito, Y. Matsumoto, M. Ispida, and Y. Tadokoro, “An integrated micro fluxgate magnetic sensor,” *Sensors and Actuators A: Physical*, vol. 55, pp. 121–126, July 1996.

[6] L. Chiesi, P. Kejik, B. Janossy, and R. Popovic, “CMOS planar 2D micro-fluxgate sensor,” *Sensors and Actuators A: Physical*, vol. 82, pp. 174–180, May 2000.

[7] A. Baschirotto, E. Dallago, M. Ferri, P. Malcovati, A. Rossini, and G. Venchi, “A cmos 2d micro-fluxgate earth magnetic field detecting system with rs232 digital output,” in *IEEE Sensors*, 2007, pp. 240 – 243.

[8] A. Baschirotto, E. Dallago, P. Malcovati, M. Marchesi, and G. Venchi, “Development and comparative analysis of fluxgate magnetic sensor structures in pcb technology,” *Magnetics, IEEE Transactions on*, vol. 42, no. 6, pp. 1670–1680, June 2006.

[9] J.-S. Hwang, H.-S. Park, D.-S. Shim, K.-W. Na, W.-Y. Choi, and S.-O. Choi, “Electronic compass using two-axis micro fluxgate sensing element,” *TRANSDUCERS, Solid-State Sensors, Actuators and Microsystems, 12th International Conference on, 2003*, vol. 2, pp. 1618–1621 vol.2, June 2003.

[10] A. Baschirotto, E. Dallago, P. Malcovati, M. Marchesi, and G. Venchi, “From a pcb fluxgate to an integrated micro fluxgate magnetic sensor,” *Instrumentation and Measurement Technology Conference, 2005. IMTC 2005. Proceedings of the IEEE*, vol. 3, pp. 1756–1760, May 2005.

[11] A. Baschirotto, A. Cabrini, E. Dallago, P. Malcovati, M. Marchesi, and G. Venchi, “Development and analysis of a pcb vector 2-d magnetic field sensor system for electronic compasses,” *Sensors Journal, IEEE*, vol. 6, no. 2, pp. 365–371, April 2006.

[12] A. Baschirotto, E. Dallago, V. Ferragina, M. Ferri, M. Grassi, P. Malcovati, M. Marchesi, E. Melissano, M. Morelli, A. Rossini, S. Ruzza, P. Siciliano, and G. Venchi, “A CMOS 2D micro-fluxgate earth magnetic field sensor with digital output,” in *IEEE International Solid-State Circuits Conference Digest of Technical Papers*, Feb. 2007, pp. 390–391.

[13] V. Ferragina, M. Ferri, M. Grassi, A. Rossini, P. Malcovati, and A. Baschirotto, “A 12.4 enob incremental a/d converter for high-linearity sensors read-out applications,” *Circuits and Systems, 2007. ISCAS 2007. IEEE International Symposium on*, pp. 3582–3585, May 2007.

[14] A. Baschirotto, F. Borghetti, E. Dallago, P. Malcovati, M. Marchesi, and G. Venchi, “A cmos front-end circuit for integrated fluxgate magnetic sensors,” in *Circuits and Systems, 2006. ISCAS 2006. Proceedings. 2006 IEEE International Symposium on*, 0-0 2006, pp. 4 pp.–4406.

[15] A. Baschirotto, F. Borghetti, E. Dallago, P. Malcovati, M. Marchesi, E. Melissano, P. Siciliano, and G. Venchi, “Fluxgate magnetic sensor and front-end circuitry in an integrated microsystem,” *Sensors and Actuators A: Physical*, vol. 132, no. 1, pp. 90 – 97, 2006, the 19th European Conference on Solid-State Transducers. [Online]. Available: http://www.sciencedirect.com/science/article/B6THG-4K4WMR5-2/2/2fdffebb442ba7bf0d7f0b535013ea15

[16] E. Dallago, M. Ferri, P. Malcovati, A. Rossini, G. Venchi, and A. Baschirotto, “A cmos 2d micro-fluxgate earth magnetic field detecting system with rs232 digital output,” *Sensors, 2007 IEEE*, pp. 240–243, Oct. 2007.

[17] A. Baschirotto, E. Dallago, V. Ferragina, M. Ferri, M. Grassi, P. Malcovati, M. Marchesi, E. Melissano, M. Morelli, A. Rossini, S. Ruzza, P. Siciliano, and G. Venchi, “A cmos 2d micro-fluxgate earth magnetic field sensor with digital output,” *Solid-State Circuits Conference, 2007. ISSCC 2007. Digest of Technical Papers. IEEE International*, pp. 390–610, Feb. 2007.

[18] M. Marwick and A. Andreou, “Photo-battery fabricated in silicon on sapphire cmos,” *Electronics Letters*, vol. 44, no. 12, pp. 766–767, 5 2008.

[19] D. Dondi, D. Brunelli, L. Benini, P. Pavan, A. Bertacchini, and L. Larcher, “Photovoltaic cell modeling for solar energy powered sensor networks,” *Advances in Sensors and Interface, 2007. IWASI 2007. 2nd International Workshop on*, pp. 1–6, June 2007.

[20] N. Guilar, A. Chen, T. Kleeburg, and R. Amirtharajah, “Integrated solar energy harvesting and storage,” *Low Power Electronics and Design, 2006. ISLPED’06. Proceedings of the 2006 International Symposium on*, pp. 20–24, Oct. 2006.

[21] N. J. Guilar, E. G. Fong, T. Kleeburg, D. R. Yankelevich, and R. Amirtharajah, “Energy harvesting photodiodes with integrated 2d diffractive storage capacitance,” in *ISLPED ’08: Proceeding of the thirteenth international symposium on Low power electronics and design*. New York, NY, USA: ACM, 2008, pp. 63–68.

[22] A. Hande, T. Polk, W. Walker, and D. Bhatia, “Indoor solar energy harvesting for sensor network router nodes,” *Microprocessors and Microsystems*, vol. 31, no. 6, pp. 420–432, September 2007. [Online]. Available: http://dx.doi.org/10.1016/j.micpro.2007.02.006

[23] A. Barnett, C. Honsberg, D. Kirkpatrick, S. Kurtz, D. Moore, D. Salzman, R. Schwartz, J. Gray, S. Bowden, K. Goossen, M. Haney, D. Aiken, M. Wanlass, and K. Emery, “50*Photovoltaic Energy Conversion, Conference Record of the 2006 IEEE 4th World Conference on*, vol. 2, pp. 2560–2564, May 2006.

[24] E. Ralph, “High efficiency solar cell arrays system trade-offs,” *Photovoltaic Energy Conversion, 1994., Conference Record of the Twenty Fourth. IEEE*

Photovoltaic Specialists Conference - 1994, 1994 IEEE First World Conference on, vol. 2, pp. 1998–2001 vol.2, Dec 1994.

[25] J. McGee, “Photoelectric cells-a review of progress,” *Component Parts, IRE Transactions on*, vol. 5, no. 1, pp. 2–23, Mar 1958.

[26] N. Guilar, A. Chen, T. Kleeburg, and R. Amirtharajah, “Integrated solar energy harvesting and storage,” in *ACM/IEEE ISLPED*, 2006, pp. 20–24.

[27] A. Kansal and M. Srivastava, “An environmental energy harvesting framework for sensor networks,” in *Intl. Symp. Low Power Elec. and Design (ISLPED) ’03*, 2003, pp. 481–486.

[28] A. Arms, C. Townsed, D. Churchill, J. Galbreath, and S. Mundell, “Power management for energy harvesting wireless sensor,” in *SPIE International Symposium on Smart Structures and Smart Materials*, 2005.

[29] B. Otis, Y. Chee, and J. Rabey, “A 400 µw-rx, 1.6mw-tx super-regenerative transceiver for wireless sensor networks,” in *IEEE International Solid-State Circuits Conference (ISSCC 2005)*, 2005, pp. 396–7.

[30] M. Rahimi, H. Shah, G. Sukhatme, J. Heideman, and D. Estrin, “Studying the feasibility of energy scavenging in mobile sensor network,” in *IEEE International Conference on Robotics and Automation Proceedings*, 2003, pp. 19–24.

[31] V. Raghunathan, A. Kansal, J. Hsu, J. Friedman, and M. Srivastava, “Design considerations for solar energy harvesting wireless embedded systems,” in *International Symposium on Informatic Processing in Sensor Networks*, 2005, pp. 457–462.

[32] A. Kansal, J. Hsu, M. Srivastava, and V. Raqhunathan, “Harvesting aware power management for sensor networks,” in *ACM/IEEE Design Automation Conference*, 2006, pp. 651–656.

[33] W. Walker, T. Polk, A. Hande, and D. Bhatia, “Remote blood pressure monitoring using a wireless sensor network,” in *Sixth IEEE Annual Emerging Information Technology Conference Proceedings*, Dallas, Texas, 2006.

[34] P. Woias, Y. Manoli, T. Nann, and V. Stetten, “Energy harvesting for autonomous microsystems,” in *MST News*, vol. 4, no. 05, 2005, pp. 42–45.

[35] J. Dickson, “On-chip high-voltage generation in nmos integrated circuits using an improved voltage multiplier technique,” in *IEEE J. Solid-State Circuits Conference*, vol. 11, no. 6, 1976, pp. 347–348.

[36] P. Malcovati, F. Maloberti, M. Pruzzi, and C. Fiocchi, “Curvature compensated bicmos bandgap with 1 v supply voltage,” in *Solid-State Circuits Conference, 2000. ESSCIRC ’00. Proceedings of the 26th European*, Sept. 2000, pp. 7–10.

[37] C.-W. Lin and Y.-J. Liu, “A power efficient and fast transient response low drop-out regulator in standard cmos process,” in *VLSI Design, Automation and Test, 2006 International Symposium on*, April 2006, pp. 1–4.